

Photon Echo and Single Molecule Fluorescence
Measurements of Organic Dyes in Thin Polymer Films

Robin Smith

Carl Grossman, advisor

March 28, 2003

Abstract

The extraordinarily short optical dephasing time of organic dye molecules in polymer hosts is known to be under 20 fs between 100 and 200 K. Short dephasing times suggest enormously broadened homogeneous linewidths on the order of 10 nm. Direct observation of single dye molecule fluorescence spectra shows a similarly broadened line, giving comparable dephasing times for room temperature measurements. While this single molecule linewidth agrees with that of the bulk sample, it is inaccurate to attribute this broadening to homogeneous mechanisms. Repeated single molecule fluorescence measurements permit determination of the homogeneous nature of this linewidth, as distinct from the inhomogeneous nature of dispersion in bulk samples. Spectral diffusion in single molecule spectra is evidenced by multiple peaks, visible despite broad spectra lines at room temperature. In the particular experiment discussed in this thesis, fluorescence from single organic dye molecules in thin polymethyl methacrylate films was studied with scanning confocal microscopy. Photon antibunching exhibited by the photon-pair correlation function $g^{(2)}(\tau)$ at $\tau = 0$ confirms that single molecule emission spectra were obtained.

Contents

1	Introduction	4
1.1	Single Molecule Spectroscopy and Microscopy	4
1.2	Historical Development	5
1.2.1	Spectroscopy of Organic Molecules in Solids	5
1.2.2	Fluorescence Techniques	6
1.2.3	Single Molecule Detection	7
1.3	Applications	8
1.4	Photon Echo Measurements of Optical Dephasing	9
2	Theory	10
2.1	Spectroscopy Definitions	10
2.2	Electronic Excitation	11
2.3	Fluorescence Lifetimes	15
2.4	Single-Molecule Sensitivity	16
2.5	Correlation Effects	17
2.5.1	Photon Antibunching	17
2.5.2	Photodynamics	18
2.6	Classical Dipole Radiation	19
2.6.1	Electric Dipole Radiation in the Radiation Zone	19
2.6.2	Power Radiated by Oscillating Electric Dipole	21
2.7	Quantum Dephasing Theory	24
2.7.1	Density Matrix Formalism	24
2.7.2	Perturbation Expansion	26
2.7.3	Scattered Intensity	28
2.7.4	Spectral Profile	30
3	Bulk Fluorescence and Absorption Measurements	33
3.1	Absorption Spectra	33
3.2	Fluorescence Spectra	34
4	Fluorescence Experiment	38
4.1	Sample Fabrication	38
4.2	Dye Selection	38
4.3	Experimental Setup	39
4.4	Data Acquisition Protocol	41

5	Single Molecule Fluorescence Results	43
5.1	Correlation Plots	43
5.2	Time Intensity Plots	46
5.3	Single Molecule Emission Spectra	54
6	Photon Echo Experiment	57
6.1	Sample Fabrication	58
6.2	Experimental Setup	60
6.3	Experiment Difficulties	62
7	Photon Echo Results	64
8	Discussion	67
8.1	Single Molecule Emission Histograms	67
8.2	Line Broadening Mechanisms	69
8.3	Photon Echo Temperature Dependence	71
9	Conclusion	73
10	Appendix A: Spectral Analysis Code	75
11	Appendix B: Single Molecule Emission Histograms	78
	References	85
	Acknowledgements	91

1 Introduction

Spectroscopic data is central to many famous breakthroughs in our knowledge. Specifically, absorption and emission spectroscopy have played an essential role in the advancement of physics. Blackbody radiation, hydrogen emission lines, and photoelectric stopping voltage (vs frequency) have shaped modern physics. Modern spectroscopy techniques, most of which include laser sources, continue to redefine our understanding of nature [21].

A multitude of new spectroscopic techniques have emerged since the invention of the laser [9, 11]. Many of these techniques address issues of isolating from the macroscopic ensemble properties of individual molecules. For example, two closely related techniques that address issues considered in this thesis include Doppler free spectroscopy and hole-burning spectroscopy. The former can isolate the absorbance of gaseous atoms that are at rest in the laboratory frame.

1.1 Single Molecule Spectroscopy and Microscopy

Details and dynamics of individual molecular events often remain hidden from view when techniques designed to measure ensembles of molecules are employed. These techniques, such as bulk absorption and emission measurements, entail statistical and often static measurements. They yield only averages, losing information about molecular heterogeneity and dynamic local environments [39]. Specific techniques usually limit sample conditions to low temperatures or gaseous media. Even under these specific conditions, comparisons between spectroscopic techniques and temporal measurements such as dephasing lifetime have been tenuous [62]. Specifically, hole burning and dephasing measurements in Nile Blue dye have given no clear connections between these measurements [80, 27, 74, 55].

In the past ten years, new techniques for isolating light emission from individual molecules have emerged. These methods combine lasers, microscopy, nanometer-scale scanning techniques, coincidence-counting statistics, fast and sensitive detection, and dilute samples to provide single-molecule resolution [44]. Application of optical spectroscopy methods to molecules that have been isolated by dilution provides a non-invasive technique sensitive to environmental and molecular conformational changes in electronic structure. Techniques such as nanometer resolution imaging and single photon-emitter detection developed for single-molecule experiments are requisite for further advances in quantum computing and nanotechnology [39].

Photon echo experiments show huge variations in dephasing time values, depending on both temperature and incident light frequency. Room temperature measurements of both homogeneous linewidth (using hole burning spectroscopy) and dephasing time (using photon echos) have been impossible or very difficult. Similarly, room temperature SMS has been difficult until recently. Theoretical models exist at low temperatures only, but the connection between dephasing time and homogeneous linewidth is expected to be analogous at higher temperatures [2, 21].

1.2 Historical Development

1.2.1 Spectroscopy of Organic Molecules in Solids

It was thought that fine resolution of electronic spectra of complex organic compounds in solution is difficult to achieve due to ill-resolved vibrational structure. As a result, both absorption and emission spectra contain broad bands, the smoothness of which makes these spectra of little use for analysis. Thus a search for techniques and conditions for obtaining more fine-structured spectra has been underway. Unfortunately, low-temperature measurements have revealed that most solutions of complex organic molecules in organic solvents possess broad-band spectra even at liquid helium temperatures [62, 4].

It was found that inhomogeneous broadening of organic solutions at low temperatures conceals existent fine structure, as the spectra actually consist of the sum of many zero-phonon lines. Fluorescence line narrowing is a method, discovered in 1972, which uses selective laser excitation to reveal zero phonon line structure in emission spectra. Spectral diffusion was found to exist even at helium temperatures, because molecular lines drift over many time scales instead of being fixed in the inhomogeneous spectrum [62].

As it became evident that site selective or energy selective spectroscopic techniques including fluorescence line narrowing cannot remove all inhomogeneity and, even at very high resolution, provide average information about molecular ensembles [62]. Single molecule spectroscopy gives access to distributions of molecular parameters in solids by permitting measurement of local information and eliminating population averages. For example, correlation properties of light emitted by single molecules yields new insight into spectral diffusion and intramolecular dynamics impossible to be determined with bulk measurements [62].

Many fascinating results have been obtained via SMS. Determination of single-molecule homogeneous line shape, study of temperature dependence of single-molecule line width, direct observation of spectral diffusion, observation of photon bunching and antibunching, and study of individual two level systems [62]. While it has been shown that true single-photon emission is limited by photobleaching as well as Brownian motion of molecules into and out of the excitation volume, fluorescence of remarkably photostable systems has been reported [72].

1.2.2 Fluorescence Techniques

It has been known for several hundred years that some organic molecules emit visible radiation upon being exposed to radiation from the sun. Likely the first observation of luminescence of the extract *Lignum Nephriticum* in water was performed by Monardes in 1565 [4, page 2]. Almost a century later, F. Liceti published *Litheosporus*, the first monograph on phosphorescence. It was not until the middle of the nineteenth century that some advances in understanding the luminescence process were made. In 1845, Herschel pointed out differences between luminescence and ordinary scattered light deduced from studying the effect of sunlight on a solution containing sulfate of quinine. Also studying this compound, Stokes was able to find that the emitted light was composed of longer wavelengths than the absorbed light. Now known as the Stokes Shift, this phenomenon was discovered in 1852 [4].

Nicholas and Merritt first observed the existence of mirror symmetry between absorption and fluorescence curves for solutions of eosin and resorufin in 1907. The early literature contains some discussion as to the type of radiation involved in the process of fluorescence. While it was generally assumed that electric-dipole radiation is responsible for fluorescence, few experiments have been performed to demonstrate this conclusively. Wide-angle interference techniques developed by Selenyi in 1911 and used to study the angular distribution of fluorescence from fluorescein demonstrated that this fluorescence is indeed electric-dipole radiation. It is interesting to note that fluorescein was first synthesized by Baeyer in 1871 [4].

First measurements of luminescence decay time were made by Wood in 1905: the luminescence from a phosphor placed on the rim of a wheel and mechanically excited as the wheel rapidly rotated was followed along the wheel as it was displaced from the point of excitation. In 1923, Gottling measured 21 ns as the decay time of rhodamine by using double-refraction. Other techniques used for measuring fluorescence decay times include those of Phillips and Swank, who used pulsed X-rays and, later, a pulsed beam of 75-keV electrons to excite phosphors [4].

1.2.3 Single Molecule Detection

Non-optical methods were used to first perform single-molecule measurements, even though an experimental scheme for the performance of nanometer resolution spectroscopy was proposed by E.A. Syngé in 1928 [39]. It is only recently that optical methods have become sensitive enough to detect, image, and manipulate individual fluorophores.

The initial demonstration of single-molecule spectroscopy was performed on pentacene molecules in a *p*-terphenyl host crystal at liquid helium temperatures using a complicated doubly-modulated absorption technique [39, page 621B]. Results were published in 1989 by Moerner and Kador. Orrit and Bernard's 1990 detection of single molecules in the same system using fluorescence excitation showed that this simpler yet very sensitive method dramatically improved the signal-to-noise ratio [62, page 10257].

The narrow zero-phonon absorption line (ZPL) of the rigid pentacene molecule corresponds to the electronic transition between the ground and first excited states. Because the energy of each molecule's ZPL varies depending upon the local fields, precise molecular selectivity by frequency tuning is possible. However, broadening of the ZPL above 10K necessitates cryogenic temperatures for this spectroscopy. Nevertheless, precise tests of molecular quantum electrodynamics and microscopic theories of molecule-environment coupling are permitted by single-molecule spectroscopic studies at cryogenic temperatures [39, pages 621T, 1, 2]. Although cryogenic temperature absorption spectroscopy was initially used, fluorescence emission spectroscopy is now favored because it is a vastly simpler experimental method [39, pages 621B, 27, 31].

Confocal microscopy allows simultaneous excitation and detection from a very small, selected region of space. This, combined with dilute, thin-film samples makes room temperature measurements are possible, and a larger signal-to-noise ratio is achieved because the fluorescence emission is Stokes-shifted from the excitation. The first room temperature single-molecule images were obtained using near-field scanning optical microscopy (NSOM).

Early experimental techniques were not confocal. They were not imaging light to match the point in space where the incident light hit the sample. Instead, they used a parabolic mirror. In the image plane of the microscope field of view, a pinhole is placed at the same two-dimensional position on the screen corresponding to the place where the laser hits the sample. Therefore, irradiation and detection of the same 200-micron region is performed [21].

Single molecules in amorphous host polymer is what we study. Early experiments isolated molecules in a fixed crystalline solid, such as p-terphenyl. Below the zero-phonon line temperature of the crystal, no phonon were active. Problems with this technique are extensive. First, it is difficult to get the dye incorporated into the crystal. Specifically, the dye is put into solution with the dissolved crystal. When the solvent is evaporated and the crystal grows, it is rare for the dye molecules to be incorporated into the crystal. Today, we are able to study any dye molecule that will dissolve in solution with a polymer host such as polymethyl methacrylate (PMMA) [21]. Additionally, these molecules in amorphous polymers can be studied at room temperature.

The local environment of a particular molecule randomly shifts the homogeneous resonance line within its inhomogeneous absorption band. The single-molecule homogeneous lines are Lorentzian in profile. For a large number of molecules, each contributing a narrow Lorentzian, a smooth Gaussian inhomogeneous profile is recovered [62, 10263, figure 8]. Because statistical fluctuations in absorption intensity for a given frequency scale inversely to the square root of the number of molecules, these fluctuations appear when the number of molecules decreases to reveal a statistical fine structure, as first observed by Moerner and Carter in 1987 [62, page 10264].

Spectral resolution of individual molecules in the sample requires selection of a sufficiently small volume of sample. However, because the diffraction spot of the exciting light limits the excited volume, care must be taken to ensure low concentration of impurities in the sample. As the most difficult single molecule detection condition to achieve is the requisite sensitivity, only the fluorescence excitation technique has thus far proven successful in resolving single molecule lines. This method, when used against a dark background, permits dramatic improvement of signal to noise ratio with respect to direct absorption [62, page 10264].

1.3 Applications

Of course, the generation of triggered single-photon states is not only of fundamental interest in quantum optics. It can be applied to quantum cryptography, because perfect security could be achieved by coding each information bit on a single photon. Initial experiments aimed at reducing the probability of emission of more than one fluorescent photon per excited-state preparation required cryogenic temperatures. Recent work with systems exhibiting higher photostability, within the limits set by photobleaching, have revealed antibunching. Such systems include semiconductor quantum dots and nitrogen-vacancy centers in diamond [72].

1.4 Photon Echo Measurements of Optical Dephasing

The simplest ultrafast optical spectroscopic technique is pump-probe spectroscopy [51]. This technique subjects a system to two short light pulses separated by time delay τ . The first (pump) pulse has frequency ω_1 , and the second (probe) pulse of frequency ω_2 is measured as a function of both frequencies and time delay. The pump pulse prepares the system in a nonequilibrium state that propagates for time τ before the probe pulse measures this state. This technique is ideal for sensitive and accurate measurement of chemical dynamics such as photoisomerization and photodissociation that occur on femtosecond time scales.

Other coherent nonlinear optical techniques include coherent Raman spectroscopy, four wave mixing, transition gratings, hole-burning, and photon echos.

Both hole-burning and photon echo resonant spectroscopies are capable of eliminating inhomogeneous broadening so useful dynamical information can be extracted from structureless, broad lineshapes. Such lineshapes are typical for spectra in liquids, glasses, and the polymers considered here. Inhomogeneous broadening often arises from many small contributions of various molecules in the sample. Hole-burning is the same technique as pump-probe spectroscopy but more useful for systems of large inhomogeneous broadening.

In two-pulse photon echo measurements, the system interacts with two external pulses with wavevectors \vec{k}_1 and \vec{k}_2 . The signal of the scattered field appears in the direction $\vec{k}_s = 2\vec{k}_2 - \vec{k}_1$ and is peaked at time $t = \tau$ [51].

2 Theory

This theory chapter starts with a macroscopic descriptive overview of fluorescence phenomenology before proceeding to a microscopic description of dipole radiation and dephasing theory. Specifically, fluorescence lifetime, signal to noise ratios, and finally single molecule-sensitivity are discussed. Correlation effects observed experimentally including photon antibunching and other photodynamics are mentioned. Classical dipole radiation provides a starting framework for connecting observable physical processes to quantum dephasing theory, the results of which provide methods of spectrum analysis.

2.1 Spectroscopy Definitions

Most radiation emitted by fluorescent organic dyes molecules is in the visible, since they absorb visible radiation. Because the molecules we study give rise to particular absorption band systems, they are called chromophores as in absorption spectroscopy [4]. The phenomenon in which a molecule is excited by electromagnetic radiation to a state in which the molecule itself emits radiation is referred to as photoluminescence. A similar process called scintillation occurs when a pulse of radiation is emitted from a molecule as a result of excitation by ionizing particles such as α - or β -particles.

Since spectroscopic techniques underlie the experimental methods used in this work, we define several relevant terms. Transmittance T is the ratio of I , the radiant energy transmitted by a sample at a particular wavelength, to I_0 , the energy incident on the sample. Then absorbance A is given by $A = \log_{10}(I_0/I)$. From the absorbance, we can calculate ϵ , the molar extinction coefficient, as follows $\epsilon = Ad/m$, where m is the molecular concentration in moles per liter, and d is the sample cell thickness. Therefore, the extinction coefficient can be considered as the absorbance per unit path length per unit molar concentration [4].

2.2 Electronic Excitation

Jablonski Diagrams

It is well-known that when a molecule absorbs electromagnetic radiation, its energy increases by the energy E of the photon absorbed, as given by Einstein's relationship $E = h\nu$. Aromatic organic molecules typically have π -electronic transitions between the highest occupied molecular orbital and the lowest unoccupied orbital or some linear combination of transitions between orbitals due to configuration interactions [21]. Using the three level system of the Jablonski diagram in Figure 1, we describe the absorption and emission processes of such a molecule when it acquires appropriate excitation energy. The singlet states (of net spin angular momentum zero) are labeled with S 's, and those states with one net unit of spin angular momentum are the triplet levels, as labeled by T 's [4, page 5].

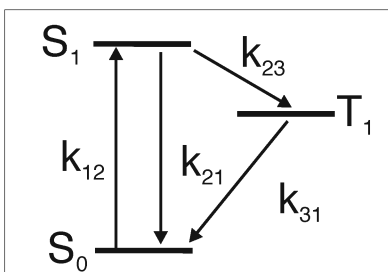


Figure 1: Three-level model of molecular response.

Each electronic level shown is comprised of many rotational and vibrational levels. Electronic and vibrational state energy differences are 1-2 eV and about 0.1 eV, respectively, for liquids at room temperature. Since rotational transition energies are typically a factor of ten smaller, on the order of 0.01 eV, they are too small to be observed in the systems considered here [4, page 5].

Since the energy difference 0.1 eV corresponds to temperature 1160 K, we can expect that π -electrons which can participate in transitions resulting in fluorescence are to be found in the state S_0 , the ground state zero vibrational level, at room temperature. If a photon of appropriate energy is absorbed by the molecule, one of these electrons is promoted to one of several vibrational levels of the first excited state S_1 .

Fluorescence Emission

Typically in condensed media, an electron in a high vibrational level undergoes vibrational relaxation; it loses its excess vibrational energy through collision with nearby molecules within about 10^{-12} sec. However, if the molecule can remain in the S_1 lowest excited state for at least 10^{-9} sec without the presence of competing processes, then the molecule will likely emit fluorescence radiation.

In fact, fluorescence radiation is defined as radiation emitted in transition between the lowest two singlet states, S_1 and S_0 . More specifically, fluorescence transitions are those which take place from the lowest (zero) vibrational level of the first excited state to one of the ground state vibrational levels. Then excess ground state vibrational energy is lost through collisions with neighboring molecules [4].

Interestingly, then, absorption and fluorescence phenomena reveal different information about molecular energy level structure. An absorption spectrum displays vibrational spacing in the first excited state to which molecules are excited when a photon is absorbed, while a fluorescence spectrum depicts ground state vibrational spacing. It is from a comparison of their similarly structured intensity patterns that the mirror symmetry between absorption and fluorescence spectra is revealed [4].

Stokes Shift

It was Stokes who first pointed out that molecules generally fluoresce at wavelengths longer than the wavelength of excitation. The Stokes shift ν_{sl} difference in frequency between the incident and emitted photons, and the corresponding Stokes loss $\hbar\nu_{sl}$ is the loss in energy equal to the energy difference between excitation and emission photons. This energy is usually lost to heat (i.e. through collisions with neighboring molecules) as the molecule shifts from higher to lower energy vibrational level in the first excited state before making the radiative transition to the ground state [4].

Such a pre-radiative transition is required since radiative transitions generally take place from the zero vibrational level of the first excited state S_1 . Therefore, some of the excitation energy available for fluorescence is lost in the vibrational energy transfer. The proportion of energy lost before radiative deexcitation depends on several physical factors of the particular molecular system,

including the shape of the ground state potential, the frequency of the radiative transition, and the change in the molecular configuration the molecule undergoes during the electronic transition. Specifically, the greater difference in the equilibrium configurations of the molecule in the states before and after the radiative deexcitation, the wider the separation between the peaks of the absorption and fluorescence emission spectra, and the greater the Stokes loss [4].

It is interesting to note that molecules with a large Stokes shift exhibit little self-absorption of their fluorescence radiation because a greater fraction of the excitation energy goes into vibrational rather than radiative energy. With little self-absorption, the fluorescence spectrum exhibits little dependence on the frequency of exciting radiation. The analysis we use in this experiment is most applicable to molecules with little Stokes shift, as similar structure is manifested in the absorption and fluorescence spectra of such molecules [4].

Other Transitions and Emission

In transitions from the ground state S_0 to the upper electronic state S_2 , the molecule rapidly dissipates the excess energy it has by virtue of not being in the lowest electronically excited state. This energy is dissipated as heat, and the molecule drops to the S_1 state in about 10^{-12} sec without emitting electromagnetic radiation. This rapid, radiationless transition between energy states of the same multiplicity (singlet to singlet, or triplet to triplet conversion) is known as internal conversion [4].

Besides fluorescence, intersystem crossing is a possible pathway for molecular deexcitation from the first excited state. A transition from S_1 to T_1 , the metastable triplet level, occurs. The triplet level is called metastable because a molecule may remain in this state for as long as several seconds, a relatively long time period.

The proceeding reversion from the triplet to the ground state S_0 may occur with or without luminescence. If radiation is emitted in this transition, it is called phosphorescence. If excess energy is converted to heat for the transition to occur, the process is again termed intersystem crossing and designated as β -phosphorescence.

Deexcitation from T_1 to S_0 via S_1 is termed α -phosphorescence and leads to radiation emission of the same spectral distribution as that of fluorescence, but with a distinctively different temporal distribution. Delayed fluorescence is another process with similar spectral but different temporal

distribution from fluorescence and α -phosphorescence. Because delayed fluorescence arises due to the interaction of two molecules in their respective triplet states, it requires a high density of molecules in their triplet states [4].

2.3 Fluorescence Lifetimes

If N_0 molecules are excited from their ground to first excited energy level, they will randomly emit this excitation energy. If dN/dt , the number of molecules losing their excitation energy per unit time (to which the fluorescence radiation intensity is proportional), is proportional to the number of remaining excited molecules N , then we can write $dN/dt = -yN$ and

$$N = N_0 e^{-yt} \quad (1)$$

given that y is a proportionality constant. Note that since the molecules are losing energy, the transition rate is proportional to the negative of the number of remaining molecules.

If we define τ as the specific time at which $y\tau = 1$, then at this time $N = N_0/e$ and $dN/dt = -(1/e)(yN_0)$. It is then evident that τ , the fluorescence decay time, is the interval of time during which the intensity of fluorescence radiation has fallen to $1/e$ of its original, maximal value.

If emission of electromagnetic radiation is the only process by which molecules can lose excitation energy, then the natural lifetime τ_0 of the radiation process can be determined. That is, if p_e is the probability per second for a molecule to emit its excitation energy by radiation, then $\tau_0 = 1/p_e$.

For molecules that can lose excitation energy by processes other than emission of radiation, including internal conversion and energy transfer, then the probability p of excitation energy loss by any of these processes is the sum of the probabilities of energy loss by each process individually. Therefore, $p = p_e + p_i + p_t$, given that p_i is the probability per second for molecular excitation energy loss by internal conversion and intersystem crossing, and p_t is the probability per second for energy transfer to another molecule. The reciprocal of this probability is the decay time τ .

The natural fluorescence lifetime τ_0 and decay time τ are related by Q , the fluorescence quantum yield, via the following relation

$$\tau_0 = \tau/Q. \quad (2)$$

The fluorescence quantum yield is the ratio of photons emitted to photons absorbed. Note that if radiation is the only available decay process, then the quantum yield is unity (each absorbed photon results in a photon emission event) and the natural fluorescence lifetime is equal to the decay time of the process which, in this case, is exclusively fluorescence emission (8) [4].

Decay times for fluorescence emission are characteristic of the specific decay process more than the particular molecule in which the emission occurs. Therefore it relevant to note the drastic differences

between the decay times characteristic of decay from singlet and triplet states. The decay time for emission from an excited electronic singlet state is very short, on the order of nanoseconds, while the decay time of an excited triplet state is on the millisecond or longer time scale. Recalling that the triplet state is a metastable level, this long lifetime is not surprising (9) [4].

2.4 Single-Molecule Sensitivity

An objective lens focuses excitation light of power P transmitted at frequency ν to excite a diffraction-limited ellipsoidal volume of a sample with cross sectional area A . For low concentration or small excitation volume V , the probability of finding two or molecules in the excited volume is negligible. Then it is possible to separate the signal of a single molecule from that of other molecules. Assuming this condition is satisfied, single-molecules in the sample are optically excited by photon absorption leading to fluorescence emission and detection. This process is characterized by two parameters including an absorption cross section σ and quantum yield Q , the average number of photons emitted for each photon absorbed. The emission signal is collected by a second optical element and directed toward a detector, overall efficiency of detection being characterized by the parameter E [39].

Optimization of signal and noise is crucial for observation of single molecules. We find an expression for the signal-to-background ratio (SBR) by first considering the following expression for signal rate s

$$s = EQ\sigma P/Ah\nu \quad (3)$$

in counts per second (Hz). For a detector dark count rate d and a background rate b per unit excitation volume and unit-excitation power, the signal-to-background ratio is

$$SBR = \frac{EQ\sigma}{bVAh\nu} \quad (4)$$

Larger excitation power (without saturation) or longer integration time will improve the signal-to-noise ratio (SNR) without affecting (SBR). These considerations are important, since the life span of single molecules is typically incredibly short. In an oxygen-rich environment, single molecules generally emit on the order of 10^6 photons before photobleaching (irreversible degradation) occurs. Therefore, it is advantageous to adjust excitation and detection parameters to maximize the duration of a single-molecule observation. Background sources as well as excitation volume and intensity are minimized as much as possible [39].

2.5 Correlation Effects

Correlation properties of light emitted by single molecules gives new insight about intramolecular dynamics and spectral diffusion, which would be impossible to obtain in experiments with ensembles of molecules. In the single molecule fluorescence studies discussed here, the correlation function is derived from a distribution of time intervals between pairs of fluorescent photons emitted [34, 65, 72].

The correlation is the distribution $g^{(2)}(\tau)$ of photon pairs separated by time delay τ , where

$$g^{(2)}(\tau) = \frac{\langle I(t)I(t+\tau) \rangle}{\langle I(t) \rangle^2} \quad (5)$$

for $\langle I(t) \rangle^2$ being the long-time average intensity. This normalized form of the correlation function is called the degree of second-order temporal coherence. The equivalence between the intensity autocorrelation and time interval distribution function can be shown in the limit of sparse photon count rate compared to detector response rate [3].

For the experiments reported in this thesis, the correlation of detected photons at two points was measured by a Hanbury-Brown-Twiss interferometer; when a 50/50 beamsplitter directs photons to be measured by either of two photodetectors, the correlation is proportional to the transition rate for joint photon absorption at both points of detector entry. Several examples of the specific information that can be gleaned from fluorescence fluctuations include photon antibunching, bunching due to intersystem crossing, and bunching due to spectral jumps.

2.5.1 Photon Antibunching

Photon antibunching is a signature of quantum mechanics here used as an indication of single molecule fluorescence contributions. If the fluorescence intensity $I(t)$ was a continuous classical function of time, our definition of $g^{(2)}$ would specify that $g^{(2)}(0) \geq g^{(2)}(\infty)$. For a single molecule excited by a coherent laser field, the actual quantum evolution of the molecule's state is relevant. Specifically, quantum state evolution introduces discontinuous jumps upon measurement that can lead to antibunching, that is, correlation functions for which the $g^{(2)}$ value at $t = 0$ is less than its value after long times.

In the case of a single emitter, the probability of a second photon being detected is zero, so $g^{(2)}(\tau = 0) = 0$. Before a second photon can be emitted, the molecule must be excited again.

Therefore, we expect the correlation function measured for a single molecule to exhibit a dip to zero around zero time delay [72]. Of course, experimental limitations such as detector noise and background signal prevent true zero intensity measurements, but theory predicts $g^{(2)}(\tau = 0) = 0$.

Indeed, photon antibunching was demonstrated experimentally thirty years ago first on single atoms in beams and later on single ions in traps. Orrit and Bernard were the first to measure the correlation of the fluorescence of single pentacene molecules in *p*-terphenyl [61]. They used this correlation measurement to prove that the fluorescence signal of a single molecule was recorded. Experiments by Basché et al. have exhibited photon antibunching on single pentacene molecule in a *p*-terphenyl crystal [3].

2.5.2 Photodynamics

Relaxation of a molecule into and out of the triplet state is called intersystem crossing. The triplet state plays an integral role in photodynamics of molecules by specifying an upper limit for the number of photons the molecule may absorb before crossing into the triplet 'dark' state in which fluorescence does not occur. Therefore, dark intervals without fluorescence are indicative of the average triplet state lifetime. The duration of the bright (fluorescent) intervals depends on the excitation intensity, which governs the average occupation of the excited singlet state.

Rates of intersystem crossing vary significantly between molecules, most likely due to influence of neighboring molecules or the environment. Sensitivity of intramolecular intersystem crossing varies between species, but it seems that this mechanism amplifies distortions responsible for inhomogeneous broadening.

Spectral jumps occur when a single molecule coupled to a specific two-level system jumps from one potential to another. Spectral diffusion occurs because the single molecule's resonance switches frequencies. Because the two-level system to which the molecule is coupled is linked to its environment, spectral diffusion is indicative of the strength of coupling between molecule and environment.

2.6 Classical Dipole Radiation

The aim of this section on classical dephasing theory is to provide a basic physical model for the spectral features of linewidth and to link the spectral features to temporal features.

The Lorentz model treats the atomic electron as an oscillator to provide a description of atoms' response to perturbations [40]. This model is based on Lorentz's hypothesis that an electron in an atom responds to light as if it were bound to the nucleus by a spring and therefore oscillating about the nucleus. This model asserts that the electron in the atom has an equilibrium position in the absence of external forces. The electron experiences the Lorentz force when influenced by an electromagnetic field and is therefore displaced from its equilibrium position. The elastic restoring force is given by Hooke's Law $F = -kx$ with the spring constant k dependent on the electron's natural oscillation frequency ω_0 and mass m by $\omega_0^2 = \frac{k}{m}$. Note that we discuss here the steady-state solution for the forced harmonic oscillator and add damping later.

2.6.1 Electric Dipole Radiation in the Radiation Zone

To find the far fields (fields in the radiation zone) due to an atom, we model the atom in the following manner: $+q$ is the nuclear charge centered at the origin, and $-q$ is the electron charge oscillating along the x -axis [20]. The electron motion in time is described by the following equation

$$\vec{r}_e = r_0(\omega)e^{i\omega t}\hat{i}, \quad (6)$$

where r_e is the distance along the x -axis from the origin to the position of the electron. The frequency response of a system is given by the term $r_0(\omega)$, which may contain information on resonances, width, and exponential decay. Then for \vec{r} being the distance from the origin to the field point and \vec{r}' being the distance from the electron to the field point, the charge density is

$$\rho(\vec{r}', t_r) = q\delta(\vec{r}' - \vec{r}_e)\delta(y)\delta(z) \quad (7)$$

with the retarded time given by

$$t_r = t - \frac{|\vec{r} - \vec{r}'|}{c} \quad (8)$$

to first order. We then have the current density

$$\vec{J} = \frac{dr_e}{dt}\hat{i} = qi\omega r_0 e^{i\omega t_r}\delta(y)\delta(z)\hat{i}. \quad (9)$$

Two of Maxwell's equations, Faraday's law

$$\nabla \times \vec{E} = -\frac{1}{c} \frac{\partial \vec{B}}{\partial t} \quad (10)$$

and $\nabla \cdot \vec{B} = 0$, which leads to $\vec{B} = \nabla \times \vec{A}$, reveal that the fields in the radiation zone depend upon the vector potential \vec{A} where

$$\begin{aligned} \vec{A} &= \int \frac{\vec{J}(\vec{r}', t_r)}{|\vec{r} - \vec{r}'|} dv' \\ &= \hat{q}i\omega r_0 \left((x - x_e)^2 + y^2 + z^2 \right)^{-1/2} \exp \left[i\omega \left(t - \frac{1}{c} \sqrt{(x - x_e)^2 + y^2 + z^2} \right) \right]. \end{aligned} \quad (11)$$

Note that $x_e \ll r = \sqrt{x^2 + y^2 + z^2}$ since $x_e = r_e = x_0 e^{i\omega t_r}$ is on the order of the atom size. Expanding $(x - x_e)^2$ as $x^2 - 2xx_e + x_e^2$, the square root terms in Equation 11 then become

$$\sqrt{(x - x_e)^2 + y^2 + z^2} = \sqrt{r^2 \left(1 - \frac{2xx_e}{r^2} + \frac{x_e^2}{r^2} \right)}. \quad (12)$$

Since the last term $\frac{x_e^2}{r^2}$ is very small, we drop it and are left with $r(1 - \frac{2xx_e}{r^2})^{1/2}$. The binomial expansion then gives

$$\sqrt{(x - x_e)^2 + y^2 + z^2} \approx r \left(1 - \frac{xx_e}{r^2} \right). \quad (13)$$

so the vector potential becomes

$$\vec{A} = \hat{q}i\omega r_0 \frac{1}{r} \left(1 + \frac{xx_e}{r^2} \right) \exp(i\omega t) \exp \left[-\frac{i\omega r}{c} \left(1 - \frac{xx_e}{r^2} \right) \right]. \quad (14)$$

Considering just terms to first order of r in the denominator, the vector potential becomes

$$\vec{A} = \hat{q}i\omega r_0 \frac{e^{-i\omega r/c}}{r} e^{i\omega t} + O \left(\frac{1}{r^2} + \frac{1}{r^3} + \dots \right). \quad (15)$$

Then for dipole moment $\vec{p} = \hat{q}r_0$, the vector potential is approximately

$$\vec{A} \approx i\omega \vec{p} \frac{e^{-i\omega r/c}}{r} e^{i\omega t}. \quad (16)$$

Since we know $\vec{B} = \nabla \times \vec{A}$, then the far field \vec{B} is given by

$$\vec{B} = \omega^2 \frac{e^{-i\omega r/c}}{r} e^{i\omega t} \hat{r} \times \vec{p}. \quad (17)$$

Then to find the electric field \vec{E} in the radiation zone, we insert $\vec{B} = \nabla \times \vec{A}$ into Faraday's Law to obtain

$$\nabla \times \vec{E} = -\frac{1}{c} \frac{\partial \vec{B}}{\partial t} = -\frac{1}{c} \frac{\partial}{\partial t} (\nabla \times \vec{A}). \quad (18)$$

Then

$$\vec{E} = -\frac{1}{c} \frac{\partial \vec{A}}{\partial t} + K \quad (19)$$

where $K = \text{const.}$ Moving the derivative term to the other side of the equation gives

$$\vec{E} + \frac{1}{c} \frac{\partial \vec{A}}{\partial t} = K. \quad (20)$$

Taking the curl of each side of the equation and recalling the vector identity $\nabla \times (\nabla \phi) = 0$, we have

$$\nabla \times \left[\vec{E} + \frac{1}{c} \frac{\partial \vec{A}}{\partial t} \right] = 0. \quad (21)$$

Identifying

$$\vec{E} + \frac{1}{c} \frac{\partial \vec{A}}{\partial t} = -\nabla \phi \quad (22)$$

then

$$\vec{E} = -\nabla \phi - \frac{1}{c} \frac{\partial \vec{A}}{\partial t}. \quad (23)$$

To calculate the scalar potential ϕ , we consider the integral form

$$\phi(r, t) = \int \frac{\vec{\rho}(\vec{r}', t_r)}{|\vec{r} - \vec{r}'|} dv'. \quad (24)$$

Integration yields

$$\phi(r, t) = \left[-\frac{q}{|\vec{r} - \vec{r}'|} + \frac{q}{|\vec{r}'|} \right] e^{i\omega t_r}, \quad (25)$$

which simplifies to

$$\phi(r, t) = -\frac{qx_e e^{i\omega t_r}}{r^3} \quad (26)$$

by analogy to Equations 11 and 13.

Compared to

$$\frac{\partial \vec{A}}{\partial t} = -\omega^2 \vec{p} e^{i\omega t} \frac{e^{-i\omega r/c}}{r}, \quad (27)$$

the $\nabla \phi$ contribution will be negligible in the radiation zone.

2.6.2 Power Radiated by Oscillating Electric Dipole

Into Equation 23 we plug the results of Equations 26 and 27 to obtain

$$\vec{E} = \frac{\omega^2}{c} e^{i\omega t} \frac{e^{-i\omega r/c}}{r} \hat{r} \times \vec{p} \times \hat{r}, \quad (28)$$

which reduces to

$$\vec{E} = \frac{1}{c}(\hat{r} \times \vec{B}). \quad (29)$$

Then plugging in for \vec{B} from Equation 17 yields

$$\vec{E} = \frac{\omega^2}{c} e^{i\omega t} \frac{e^{-i\omega r/c}}{r} (\vec{p} - \hat{r}(\hat{r} \cdot \vec{p})). \quad (30)$$

Notice the dipole fields are in phase, transverse, and mutually perpendicular.

Switching from coordinate-free to the more conventional spherical coordinate representation of the dipole field permits observation of the radiated power distribution. We have

$$\vec{E} = p\omega^2 \frac{\sin \theta}{r} \cos[\omega(t - r/c)] \hat{\theta} \quad (31)$$

for $|\vec{p}| = p = r_0 q$ and

$$\vec{B} = \frac{p\omega^2}{c} \frac{\sin \theta}{r} \cos[\omega(t - r/c)] \hat{\phi}. \quad (32)$$

First calculating the Poynting vector \vec{S} , we obtain

$$\vec{S} \equiv \vec{E} \times \vec{B} = \frac{1}{c} \left[p\omega^2 \frac{\sin \theta}{r} \cos[\omega(t - r/c)] \right]^2 \hat{r}. \quad (33)$$

Time-averaging over a complete cycle to obtain the average intensity $\langle \vec{S} \rangle$ gives

$$\langle \vec{S} \rangle = \frac{p^2 \omega^4}{2c} \frac{\sin^2 \theta}{r^2} \hat{r}. \quad (34)$$

Notice that since $\sin(\theta = 0, \pi) = 0$, there exists no radiation along the axis of the dipole. The intensity profile reveals maximal intensity in the equatorial plane ($\theta = \pi/2$) and an overall torus-shaped intensity profile [20, 40, 33].

Integration of the intensity $\langle \vec{S} \rangle$ over a sphere of radius r gives the total power radiated $\langle P \rangle$, as follows

$$\langle P \rangle = \int \langle \vec{S} \rangle \cdot d\vec{a} = \frac{p^2 \omega^4}{2c} \int \frac{\sin^2 \theta}{r^2} r^2 \sin \theta d\theta d\phi. \quad (35)$$

This integrates to

$$\langle P \rangle = \frac{8\pi p^2 \omega^4}{3c \cdot 2} = \frac{4\pi}{3} \frac{p^2 \omega^4}{c}. \quad (36)$$

Notice the sharp frequency dependence of the power radiated. Therefore, energy absorbed and reradiated by an oscillating dipole increases in strength for higher frequencies ω . As expected by

energy conservation, the total power radiated is independent of the radius r of the sphere over which the intensity was integrated.

These results for the fields and power radiated by an oscillating electric dipole are useful for considering the interaction of a monochromatic electromagnetic field with an atom. In the Lorentz model, this incident electromagnetic field forces atomic electron oscillation at the field frequency. An induced dipole moment in the atom then serves as a new electromagnetic field source; it is these new radiation fields we just calculated [20].

2.7 Quantum Dephasing Theory

The interaction of a two-level system with a light field can be described using a density matrix formalism [48, 16]. Specifically, we consider two nearly resonant light beams with the same frequency ω . A state initially in a superposition of the upper and lower levels, given by $|\psi, t = 0\rangle = c_1|1\rangle + c_2|2\rangle$ where subscript 1 represents the lower and 2 the upper level, evolves into $|\psi(t)\rangle = c_1|1\rangle e^{-i\omega_1 t} + c_2|2\rangle e^{-i\omega_2 t}$ at time t later.

For the Hamiltonian $H_T = H_A + H_I$, H_A is the atomic term and H_I represents the interaction. We have $H_A|1\rangle = E_1|1\rangle$ and $H_A|2\rangle = E_2|2\rangle$. Denoting the time derivative of $c_1(t)$ as \dot{c}_1 , we next use the time dependent Schroedinger equation $H_T|\psi\rangle = i\hbar \frac{d\psi}{dt}$. For the left side we obtain

$$H_T|\psi(t)\rangle = c_1 E_1|1\rangle e^{-i\omega_1 t} + c_2 E_2|2\rangle e^{-i\omega_2 t} + c_1 H_I|1\rangle e^{-i\omega_1 t} + c_2 H_I|2\rangle e^{-i\omega_2 t} \quad (37)$$

and for the right side

$$i\hbar \frac{d\psi}{dt} = i\hbar [(\dot{c}_1 - i\omega_1 c_1)|1\rangle e^{-i\omega_1 t} + (\dot{c}_2 - i\omega_2 c_2)|2\rangle e^{-i\omega_2 t}]. \quad (38)$$

Since $\hbar\omega_1 = E_1$ and $\hbar\omega_2 = E_2$, we cancel two terms from each side to obtain

$$c_1 H_I|1\rangle e^{-i\omega_1 t} + c_2 H_I|2\rangle e^{-i\omega_2 t} = i\hbar \dot{c}_1|1\rangle e^{-i\omega_1 t} + i\hbar \dot{c}_2|2\rangle e^{-i\omega_2 t}. \quad (39)$$

2.7.1 Density Matrix Formalism

Using density matrix formalism, we consider the following density matrix elements: $\rho_{11} = |c_1|^2$, $\rho_{22} = |c_2|^2$, and $\rho_{12} = c_1 c_2^*$. So then $\dot{\rho}_{ij} = c_i \dot{c}_j^* + \dot{c}_i c_j^*$. Toward this end, we next calculate $i\hbar \dot{c}_1$ by multiplying on the left by $\langle 1|$ and multiplying through by $e^{i\omega_1 t}$ to obtain [34]

$$i\hbar \dot{c}_1 = c_1 \langle 1|H_I|1\rangle + c_2 e^{-i(\omega_2 - \omega_1)t} \langle 1|H_I|2\rangle. \quad (40)$$

Similarly for calculating $i\hbar \dot{c}_2$, we obtain

$$i\hbar \dot{c}_2 = c_2 \langle 2|H_I|2\rangle + c_1 e^{-i(\omega_1 - \omega_2)t} \langle 2|H_I|1\rangle. \quad (41)$$

and let $\omega_1 - \omega_2 = \omega_0$.

We now use density matrix formalism to solve these two coupled differential equations, and the density matrix terms will eventually yield physically meaningful quantities. According to the semi-classical dipole interaction approximation, the Hamiltonian has only off-diagonal terms. That is,

the terms H_{11} and H_{22} go to zero. So we have $\langle 1|H_I|1\rangle = 0$ and $\langle 2|H_I|2\rangle = 0$, and we define $\langle 1|H_I|2\rangle = \langle 2|H_I|1\rangle \equiv V$ [34].

Then $i\hbar\dot{c}_1 = c_2Ve^{i\omega_0t}$ and $i\hbar\dot{c}_2 = c_1Ve^{-i\omega_0t}$. Calculating $\dot{\rho}_{11}$ yields

$$i\hbar\dot{\rho}_{11} = c_1(c_2e^{-i\omega_0t}V)^* + c_1^*(c_2e^{-i\omega_0t}V). \quad (42)$$

If we identify $c_1c_2^*$ as ρ_{12} and $c_1^*c_2$ as ρ_{21} then

$$\dot{\rho}_{11} = -\dot{\rho}_{22} = \frac{i}{\hbar}(V^*\rho_{12}e^{i\omega_0t} - V\rho_{21}e^{-i\omega_0t}). \quad (43)$$

Performing the following subtraction and using a phenomenological argument to add the last term, we obtain the following expression which matches Equation 1 in reference [77]

$$\dot{\rho}_{22} - \dot{\rho}_{11} = \frac{2i}{\hbar}(V\rho_{21}e^{-i\omega_0t} - V^*\rho_{12}e^{i\omega_0t}) - \frac{1}{T_1}(\rho_{22} - \rho_{11}). \quad (44)$$

Notice this last term $\rho_{22} - \rho_{11}$ represents the change in population between ground and excited states, thus reflecting the finite lifetime of excited states. We set $\rho_{22} - \rho_{11} \equiv \rho_D$ and note that T_1 represents the longitudinal relaxation time [48].

Similarly, we again use our expressions for \dot{c}_1 and \dot{c}_2 from just above Equation 42 to calculate $\dot{\rho}_{12}$. We know $\dot{\rho}_{12} = c_1\dot{c}_2^* + \dot{c}_1c_2^*$. Then

$$\dot{\rho}_{12} = \dot{\rho}_{21}^* = \frac{i}{\hbar}e^{i\omega_0t}(c_2Vc_2^* - V^*c_1c_1^*), \quad (45)$$

and we also use the dipole interaction potential V for the semiclassical electric dipole transition to be

$$V = \frac{1}{2}\mu E(\vec{r}, t) (e^{i\omega t} + e^{-i\omega t}). \quad (46)$$

where μ is the electric dipole for the transition and $E(\vec{r}, t)$ is the electric field amplitude [48, 34].

Using Equation 44 for $\dot{\rho}_{22} - \dot{\rho}_{11}$, letting ω represent the laser frequency (which nearly matches ω_0 , the transition frequency between the lower and upper levels), and noting $\rho_{11} = c_1c_1^*$ and $\rho_{22} = c_2c_2^*$, we obtain

$$\dot{\rho}_D = \dot{\rho}_{22} - \dot{\rho}_{11} = \frac{2i}{\hbar}\mu(E\rho_{21}e^{i(\omega-\omega_0)t} - E^*\rho_{12}e^{-i(\omega-\omega_0)t}) - \frac{1}{T_1}\rho_D. \quad (47)$$

Letting $\hat{\rho}_{21} = \rho_{21}e^{i(\omega-\omega_0)t}$, then $\hat{\rho}_{12} = \rho_{12}e^{-i(\omega-\omega_0)t}$ and Equation 47 becomes

$$\dot{\rho}_D = \frac{2i}{\hbar}\mu(E\hat{\rho}_{21} - E^*\hat{\rho}_{12}) - \frac{\rho_D}{T_1}. \quad (48)$$

We also have $\dot{\rho}_{12} = -\frac{i}{\hbar}\mu E\rho_D e^{i(\omega+\omega_0)t}$ from Equation 45. Then noting $\dot{\hat{\rho}}_{12} = \dot{\rho}_{12}i(\omega + \omega_0)t e^{i(\omega+\omega_0)t}$ and phenomenologically adding the final term, we obtain

$$\dot{\hat{\rho}}_{12} = \dot{\rho}_{21}^* = -\frac{i}{\hbar}\mu E\rho_D + i(\omega_0 - \omega)\hat{\rho}_{12} - \frac{\hat{\rho}_{12}}{T_2}. \quad (49)$$

Equations 48 and 49 are called the Optical Bloch Equations and make use of two conditions: the resonance assumption that $\omega \sim \omega_0$, and the rotating wave approximation that terms oscillating at frequencies $\omega + \omega_0$ can be ignored.

2.7.2 Perturbation Expansion

In optical dephasing experiments, light is scattered off an oscillating dipole to see if it is still oscillating. Since we need the third order susceptibility, perturbation expansion to third order is necessary to get terms that go as the cube of the field; this is the lowest order in the field that permits direct measurement of T_2 . This scheme also describes radiation due to the dipole moment oscillation, as described classically above. The polarization is calculated in terms of the states of the atoms. Then T_2 gives the spectral width and the polarization, classically assumed to be a constant parameter, is seen to decay as a function of time [80].

Calculating intensity as a function of time delay τ , we are able to extract T_2 if f , the correlation function is known. Note that it is here that Kobayashi starts deriving his peak shift method [27].

The following two manifestations of the dephasing time exist. These include the dephasing time, a direct measure of dephasing processes as $\rho_{(12)}$ decays with time and the width associated with a particular line [21].

Treating the interaction Hamiltonian H_I as a small perturbation, we use perturbation expansion in μE and successive approximation to calculate ρ_D and $\hat{\rho}_{12}$ to third order [77]. To begin, we expand $\rho_D = \rho_D^{(0)} + \rho_D^{(1)} + \dots + \rho_D^{(n)} + \dots$ and $\hat{\rho}_{12} = \hat{\rho}_{12}^{(0)} + \hat{\rho}_{12}^{(1)} + \dots + \hat{\rho}_{12}^{(n)} + \dots$, substitute these expansions for ρ_D and $\hat{\rho}_{12}$ and their derivatives in Equations 48 and 49, and equate terms of the same order on both sides of each equation.

The zeroth order approximation to Equation 48 is

$$\dot{\rho}_D^{(0)} = -\frac{\rho_D^{(0)}}{T_1}. \quad (50)$$

So then $\rho_D^{(0)} = \rho_0 e^{-t/T_1}$, where we have chosen the initial condition $\rho_D^{(0)}(t=0) = \rho_0$.

Similarly, the zeroth order approximation to Equation 49 yields

$$\dot{\hat{\rho}}_{12}^{(0)} = -\frac{\hat{\rho}_{12}^{(0)}}{\tilde{T}_2}, \quad (51)$$

and we choose $\hat{\rho}_{12}^{(0)} = 0$ for an initial condition. It follows that $\dot{\rho}_{21}^{(0)} = 0$ since $\dot{\hat{\rho}}_{12} = \dot{\hat{\rho}}_{21}^*$.

Continuing to first order, we have

$$\dot{\rho}_D^{(1)} = \frac{2i}{\hbar} \mu (E \hat{\rho}_{21} - E^* \hat{\rho}_{12}) - \frac{\rho_D^{(1)}}{T_1}, \quad (52)$$

which simplifies to

$$\dot{\rho}_D^{(1)} = -\frac{\rho_D^{(1)}}{T_1} \quad (53)$$

for the first order approximation to Equation 48.

From Equation 49,

$$\dot{\hat{\rho}}_{12}^{(1)} = -\frac{i}{\hbar} \mu E \rho_D^{(0)} - \frac{\hat{\rho}_{12}^{(1)}}{\tilde{T}_2}. \quad (54)$$

Plugging in the integrated form $\rho_0 e^{-t/T_1}$ of Equation 50 for $\rho_D^{(0)}$ yields

$$\dot{\hat{\rho}}_{12}^{(1)} + \frac{\hat{\rho}_{12}^{(1)}}{\tilde{T}_2} = -\frac{i}{\hbar} \mu E \rho_0 e^{-t/T_1}. \quad (55)$$

Solving this differential equation, we eventually obtain

$$\hat{\rho}_{12}^{(1)}(t) = \int_0^t -\frac{i}{\hbar} \mu E \rho_0 e^{-t_1/T_1} e^{t_1/\tilde{T}_2} e^{-t/\tilde{T}_2} dt_1. \quad (56)$$

Now for second order, we look back to Equation 48, from which we obtain the following second order approximation

$$\dot{\rho}_D^{(2)} = \frac{2i}{\hbar} \mu (E \hat{\rho}_{21}^{(1)}(t) - E^* \hat{\rho}_{12}^{(1)}(t)) - \frac{\rho_D^{(2)}}{T_1}. \quad (57)$$

Rewriting this as

$$\dot{\rho}_D^{(2)} + \frac{\rho_D^{(2)}}{T_1} = \frac{2i}{\hbar} \mu (E \hat{\rho}_{12}^{*(1)}(t) - E^* \hat{\rho}_{12}^{(1)}(t)), \quad (58)$$

we use the same trick to evaluate this differential equation to obtain

$$\rho_D^{(2)}(t) = \int_0^t \dot{\rho}_D^{(2)} e^{(t_2-t)/T_1} dt_2. \quad (59)$$

For the third order approximation, the following differential equation

$$\dot{\hat{\rho}}_{12}^{(3)} = -\frac{i}{\hbar}\mu E \rho_D^{(2)} - \frac{\hat{\rho}_{12}^{(3)}}{\tilde{T}_2} \quad (60)$$

gives

$$\hat{\rho}_{12}^{(3)}(t) = \int_0^t \dot{\hat{\rho}}_{12}^{(3)} e^{(t_3-t)/\tilde{T}_2} dt_3. \quad (61)$$

Replacing $\dot{\hat{\rho}}_{12}^{(3)}$ in Equation 61 with $-\frac{i}{\hbar}\mu E \rho_D^{(2)}$ from Equation 60 gives

$$\hat{\rho}_{12}^{(3)}(t) = \int_0^t -\frac{i}{\hbar}\mu E(t_3) \rho_D^{(2)} e^{(t_3-t)/\tilde{T}_2} dt_3. \quad (62)$$

Then subbing the integral expression for $\rho_D^{(2)}(t)$ from Equation 59 into Equation 62 yields

$$\hat{\rho}_{12}^{(3)}(t) = \int_{t_3=0}^t -\frac{i}{\hbar}\mu E(t_3) \int_{t_2=0}^{t_3} \dot{\rho}_D^{(2)} e^{(t_2-t_3)/T_1} dt_2 e^{(t_3-t)/\tilde{T}_2} dt_3. \quad (63)$$

Continuing this procedure of substitution, we replace $\frac{2i}{\hbar}\mu(E\rho_{21}^{(1)}(t) - E^*\hat{\rho}_{12}^{(1)}(t))$ from Equation 57 for $\dot{\rho}_D^{(2)}$ in Equation 63 to obtain

$$\hat{\rho}_{12}^{(3)}(t) = \int_{t_3=0}^t -\frac{i}{\hbar}\mu E(t_3) \int_{t_2=0}^{t_3} \frac{2i}{\hbar}\mu(E(t_2)\hat{\rho}_{12}^{*(1)}(t_2) - E(t_2)^*\hat{\rho}_{12}^{(1)}(t_2)) e^{(t_2-t_3)/T_1} dt_2 e^{(t_3-t)/\tilde{T}_2} dt_3. \quad (64)$$

For a final substitution, we replace $\hat{\rho}_{12}^{*(1)}(t_2)$ and $\hat{\rho}_{12}^{(1)}(t_2)$ in Equation 64 with the integral of Equation 56, which gives

$$\begin{aligned} \hat{\rho}_{12}^{(3)}(t) = & \int_{t_3=0}^t -\frac{i}{\hbar}\mu E(t_3) \int_{t_2=0}^{t_3} \frac{2i}{\hbar}\mu \left(E(t_2) \int_{t_1=0}^{t_2} -\frac{i}{\hbar}\mu E(t_1) \rho_0 e^{-t_1/T_1} e^{(t_1-t_2)/\tilde{T}_2} dt_1 \right. \\ & \left. - E^*(t_2) \int_{t_1=0}^{t_2} \frac{i}{\hbar}\mu E^*(t_1) \rho_0 e^{-t_1/T_1} e^{(t_1-t_2)/\tilde{T}_2} dt_1 \right) e^{(t_2-t_3)/T_1} dt_2 e^{(t_3-t)/\tilde{T}_2} dt_3 \end{aligned} \quad (65)$$

and simplifies to

$$\hat{\rho}_{12}^{(3)}(t) = -\frac{4i}{\hbar^3}\mu^3 \int_{t_3=0}^t \int_{t_2=0}^{t_3} \int_{t_1=0}^{t_2} E(t_3) \left(E(t_2)E(t_1) - E^*(t_2)E^*(t_1) \right) \rho_0 e^{(t_2-t_3-t_1)/T_1} e^{(t_3-t_2+t_1-t)/T_2}, \quad (66)$$

which agrees with Equation A7 in [48].

2.7.3 Scattered Intensity

The scattered intensity $I(\tau)$ is then given by

$$I(\tau) = \int d(\Delta\omega) g(\Delta\omega) \int_{-\infty}^{\infty} dt \int_{-\infty}^t dt_3 \int_{-\infty}^{t_3} dt_2 \int_{-\infty}^{t_2} dt_1 e^{(t_3-t_2)/T_1} e^{-(t-t_3+t_2-t_1)/T_2} \tilde{E}(t_3) \tilde{E}(t_2)$$

$$\begin{aligned} & \tilde{E}^*(t_1 + \tau) e^{i\Delta\omega(t-t_3+t_2+t_1)} \int d(\Delta\omega') g(\Delta\omega') \int_{-\infty}^t dt_6 \int_{-\infty}^{t_6} dt_5 \int_{-\infty}^{t_5} dt_4 \\ & \tilde{E}^*(t_6) \tilde{E}^*(t_5) \tilde{E}(t_4 + \tau) e^{(t_3-t_2)/T_1} e^{-(t-t_3+t_2-t_1)/T_2} e^{-i\Delta\omega'(t_4-(t_6+t_5-t))} \end{aligned} \quad (67)$$

according to [22].

In [27], Kobayashi then assumes $g(\Delta\omega) \sim 1$, which gives $\int d(\Delta\omega) e^{i(\Delta\omega)(t_1+t-t_3-t_2)} = \delta(t_1+t-t_3-t_2)$, since $\frac{1}{\sqrt{2\pi}} \int_{-\infty}^{\infty} e^{i\omega t} d\omega = \delta(t)$. The scattered intensity then becomes

$$I(\tau) = \int_{-\infty}^{\infty} dt \int_{-\infty}^t dt_3 \int_{-\infty}^{t_3} dt_2 \int_{-\infty}^{t_2} dt_1 \delta(t_1 + t - t_3 - t_2) \cdots, \quad (68)$$

reduces to

$$\begin{aligned} I(\tau) &= \int_{-\infty}^{\infty} dt \int_{-\infty}^t dt_3 \int_{-\infty}^{t_3} dt_2 \tilde{E}(t_3) \tilde{E}(t_2) \tilde{E}^*(t_3 + t_2 - t + \tau) e^{-(2t-2t_3)/T_2} \\ & \int_{-\infty}^t dt_6 \int_{-\infty}^{t_6} dt_5 \tilde{E}^*(t_6) \tilde{E}^*(t_5) \tilde{E}(t_6 + t_5 - t + \tau) e^{-(2t-2t_6)/T_2}, \end{aligned} \quad (69)$$

and, with substitutions

$$f(t_3 - t + \tau) = \int_{-\infty}^{t_3} dt_2 \tilde{E}(t_2) \tilde{E}^*(t_3 + t_2 - t + \tau) \text{ and } f^*(t_6 - t + \tau) = \int_{-\infty}^{t_6} dt_5 \tilde{E}^*(t_5) \tilde{E}(t_6 + t_5 - t + \tau),$$

leads to

$$I(\tau) = \int_{-\infty}^{\infty} dt \int_{-\infty}^t dt_3 \tilde{E}(t_3) f(t_3 - t + \tau) e^{-(2t-2t_3)/T_2} \int_{-\infty}^t dt_6 \tilde{E}^*(t_6) f^*(t_6 - t + \tau) e^{-2(t-t_6)/T_2}. \quad (70)$$

Making more substitutions, specifically, setting $t' = t_3 - t$ and $t'' = t_6 - t$ gives

$$I(\tau) = \int_{-\infty}^{\infty} dt \int_{-\infty}^0 dt' \tilde{E}(t' + t) f(t' + \tau) e^{2t'/T_2} \int_{-\infty}^0 dt'' \tilde{E}^*(t'' + t) f^*(t'' + \tau) e^{2t''/T_2} \quad (71)$$

which simplifies to

$$I(\tau) = \int_{-\infty}^0 dt' \int_{-\infty}^0 dt'' f(t' + \tau) f^*(t'' + \tau) e^{2(t'+t'')/T_2} \int_{-\infty}^{\infty} E(t + t') \tilde{E}^*(t + t'') dt. \quad (72)$$

Recognizing $E(t + t') \tilde{E}^*(t + t'')$ as $f(t' - t'')$ and replacing t' with $-t'$ and t'' with $-t''$ yields

$$I(\tau) = \int_0^{\infty} dt' \int_0^{\infty} dt'' f(t' - \tau) f^*(t'' - \tau) f(t'' - t') e^{-2(t'+t'')/T_2}. \quad (73)$$

This final result agrees with [27].

2.7.4 Spectral Profile

Having obtained the Optical Bloch equations for a two-level system interacting with an electromagnetic field in the presence of damping in Equations 48 and 49, we now consider more specifically the nature of the damping by identifying two damping time constants T_1 and T_2 . Labeled with reference to their physical positions in the density matrix, the constants are related to the longitudinal $\Gamma_1 = 1/T_1$ and transverse $\Gamma_2 = 1/T_2$ decay rates. The first quantifies the decay of ρ_{22} , while the second tracks the decay of ρ_{21} .

We start with the following specific form for the Optical Bloch Equations

$$\dot{\hat{\rho}}_{22} = -\frac{i\nu}{2}(\hat{\rho}_{12} - \hat{\rho}_{21}) - \frac{\hat{\rho}_{22}}{T_1} \quad (74)$$

and

$$\dot{\hat{\rho}}_{12} = \dot{\hat{\rho}}_{21}^* = \frac{i\nu}{2}(\hat{\rho}_{11} - \hat{\rho}_{22}) + i(\omega_0 - \omega)\hat{\rho}_{12} - \frac{\hat{\rho}_{12}}{T_2}, \quad (75)$$

where $\nu/2 = \mu E/\hbar$ is the field intensity representing the coupling strength of the interaction energy between the external field and electric dipole of the system, introduced here for notational simplification.

In the weak field limit (that is, as the field intensity approaches zero), we will see that the radiative lineshape depends only on the transverse decay time T_2 . Under steady state conditions, Equations 74 and 75 reduce to

$$-\frac{i\nu}{2}(\hat{\rho}_{12} - \hat{\rho}_{21}) = \frac{\hat{\rho}_{22}}{T_1} \quad (76)$$

and

$$\frac{i\nu}{2}(1 - 2\hat{\rho}_{22}) = \hat{\rho}_{12} \left(\frac{1}{T_2} - i(\omega_0 - \omega) \right), \quad (77)$$

where $\hat{\rho}_{11} - \hat{\rho}_{22} = 1 - 2\hat{\rho}_{22}$ since $\hat{\rho}_{11} + \hat{\rho}_{22} = 1$. Further solving Equation 77 for $\hat{\rho}_{12}$ gives

$$\hat{\rho}_{12} = \frac{i\nu}{2} \frac{(1 - 2\hat{\rho}_{22})}{\frac{1}{T_2} - i(\omega_0 - \omega)}. \quad (78)$$

Recalling $\hat{\rho}_{12} = \hat{\rho}_{21}^*$, we can substitute appropriate forms of Equation 78 into Equation 76 to obtain

$$\frac{\hat{\rho}_{22}}{T_1} = -\left(\frac{i\nu}{2}\right)^2 (1 - 2\hat{\rho}_{22}) \left[\frac{1}{\frac{1}{T_2} - i(\omega_0 - \omega)} + \frac{1}{\frac{1}{T_2} + i(\omega_0 - \omega)} \right], \quad (79)$$

which is simplified to

$$\frac{\hat{\rho}_{22}}{T_1} = \left(\frac{\nu}{2}\right)^2 (1 - 2\hat{\rho}_{22}) \left[\frac{2/T_2}{\left(\frac{1}{T_2}\right)^2 + (\omega_0 - \omega)^2} \right] \quad (80)$$

by rationalizing the denominator and simplifying. We now multiply through by T_1 and distribute $(1 - 2\hat{\rho}_{22})$ to get

$$\hat{\rho}_{22} = \frac{\nu^2 T_1}{2T_2} \frac{1}{\left(\frac{1}{T_2}\right)^2 + (\omega_0 - \omega)^2} - \frac{\nu^2 T_1}{T_2} \hat{\rho}_{22} \frac{1}{\left(\frac{1}{T_2}\right)^2 + (\omega_0 - \omega)^2}. \quad (81)$$

Now grouping the $\hat{\rho}_{22}$ terms together and factoring out $\hat{\rho}_{22}$ gives

$$\hat{\rho}_{22} = \frac{\nu^2 T_1}{2T_2} \frac{1}{\left(\frac{1}{T_2}\right)^2 + (\omega_0 - \omega)^2} \left(1 + \frac{\nu^2 T_1}{T_2} \frac{1}{\left(\frac{1}{T_2}\right)^2 + (\omega_0 - \omega)^2} \right)^{-1}, \quad (82)$$

and multiplying out the denominators yields

$$\hat{\rho}_{22} = \frac{\nu^2 T_1}{2T_2} \left(\left(\frac{1}{T_2}\right)^2 + (\omega_0 - \omega)^2 + \frac{\nu^2 T_1}{T_2} \right)^{-1}. \quad (83)$$

Finally considering $\hat{\rho}_{12}$ again, we plug this Equation 83 result for $\hat{\rho}_{22}$ into Equation 78 to obtain

$$\hat{\rho}_{12} = \frac{i\nu}{2} \frac{1}{\frac{1}{T_2} - i(\omega_0 - \omega)} \left(1 - 2 \frac{\nu^2 T_1}{2T_2} \left(\left(\frac{1}{T_2}\right)^2 + (\omega_0 - \omega)^2 + \frac{\nu^2 T_1}{T_2} \right)^{-1} \right). \quad (84)$$

Rationalizing the second multiplied term and putting the third over a common denominator gives

$$\hat{\rho}_{12} = \frac{i\nu}{2} \frac{\frac{1}{T_2} + i(\omega_0 - \omega)}{\left(\frac{1}{T_2}\right)^2 + (\omega_0 - \omega)^2} \left(\left(\left(\frac{1}{T_2}\right)^2 + (\omega_0 - \omega)^2 + \frac{\nu^2 T_1}{T_2} - \frac{\nu^2 T_1}{T_2} \right) \left(\left(\frac{1}{T_2}\right)^2 + (\omega_0 - \omega)^2 + \frac{\nu^2 T_1}{T_2} \right)^{-1} \right) \quad (85)$$

which fortunately simplifies to

$$\hat{\rho}_{12} = \frac{\nu}{2} \left(\frac{i}{T_2} - (\omega_0 - \omega) \right) \left(\left(\frac{1}{T_2}\right)^2 + (\omega_0 - \omega)^2 + \frac{\nu^2 T_1}{T_2} \right)^{-1}. \quad (86)$$

Now as ν approaches zero, this result reduces to

$$\hat{\rho}_{12} \sim \frac{\nu}{2} \left(\frac{i}{T_2} - (\omega_0 - \omega) \right) \left(\left(\frac{1}{T_2}\right)^2 + (\omega_0 - \omega)^2 \right)^{-1}. \quad (87)$$

We can see that $\hat{\rho}_{12}$ is independent of T_1 as we hoped.

Now to calculate the dipole moment expectation value $\langle d \rangle$, we recall $\rho_{12} = \hat{\rho}_{12} e^{i\omega t}$ and observe that $\langle d \rangle$ has the following form

$$\langle d \rangle = -e \left(\rho_{12} e^{i\omega t} + \rho_{21} e^{-i\omega t} \right), \quad (88)$$

where the contributions from the $\hat{\rho}_{11}$ and $\hat{\rho}_{22}$ terms are zero because no electric dipole transition between same states is possible for symmetrical systems. Plugging our results from Equation 87 into Equation 88 give

$$\langle d \rangle = e \frac{\nu}{2} \left[\frac{((\omega_0 - \omega) - i/T_2)}{(1/T_2)^2 + (\omega_0 - \omega)^2} e^{i\omega t} + \frac{((\omega_0 - \omega) + i/T_2)}{(1/T_2)^2 + (\omega_0 - \omega)^2} e^{-i\omega t} \right]. \quad (89)$$

Now to find the Fourier amplitude of the radiation intensity, we first rewrite the dipole moment expectation value in terms of the real magnitude of our complex result multiplied by a complex phase factor $e^{i\varphi}$. In this case, $\varphi = \arctan \left[(T_2(\omega_0 - \omega))^{-1} \right]$ and

$$|d| = e \frac{\nu}{2} \frac{e^{i(\omega t - \varphi)} e^{-i(\omega t - \varphi)}}{\sqrt{(1/T_2)^2 + (\omega_0 - \omega)^2}}, \quad (90)$$

which simplifies to

$$|d| = e\nu \frac{\cos(\omega t - \varphi)}{\sqrt{(1/T_2)^2 + (\omega_0 - \omega)^2}}. \quad (91)$$

Finally, the detected intensity for the radiative lineshape is

$$|I| = |d|^2 = e^2 \frac{\nu^2}{2} \frac{1}{(1/T_2)^2 + (\omega_0 - \omega)^2}. \quad (92)$$

As we expected, in the weak field limit the radiative lineshape has no longitudinal decay rate dependence; it depends only on the transverse decay rate Γ_2 .

Note that we have related the transverse decay time T_2 , a molecular property of a molecular measurable in the time domain, to the natural or homogeneous linewidth. This relation is especially useful, given that the natural linewidth is often difficult to measure directly due to inhomogeneity effects and line broadening mechanisms such as Doppler broadening in real samples [34].

3 Bulk Fluorescence and Absorption Measurements

Bulk absorption and emission spectra for several of organic dyes in methanol solution and in thin films with PMMA were acquired or obtained from catalogued sources. These spectra were useful for determining whether the absorption and emission wavelengths of particular dyes were suited to our experimental conditions.

3.1 Absorption Spectra

Absorption spectra were taken on a Jasco V-560 UV/VIS Spectrophotometer. A thin circular slide on which a thin film of disperse red in PMMA dissolved in chlorobenzene had been spin-coated was placed in a triangular lens holder on a stand just after the incident beam hole, in front of the cuvette-holding apparatus.

Figures 2 and 3 display absorption spectra of Disperse Red 1 in methanol solution and in a thin film with PMMA dissolved in chlorobenzene, respectively [66, pages 78 and 107]. While the peak absorption for each is approximately 500 nm in wavelength, the absorption band is considerably wider for the dye in polymer film.

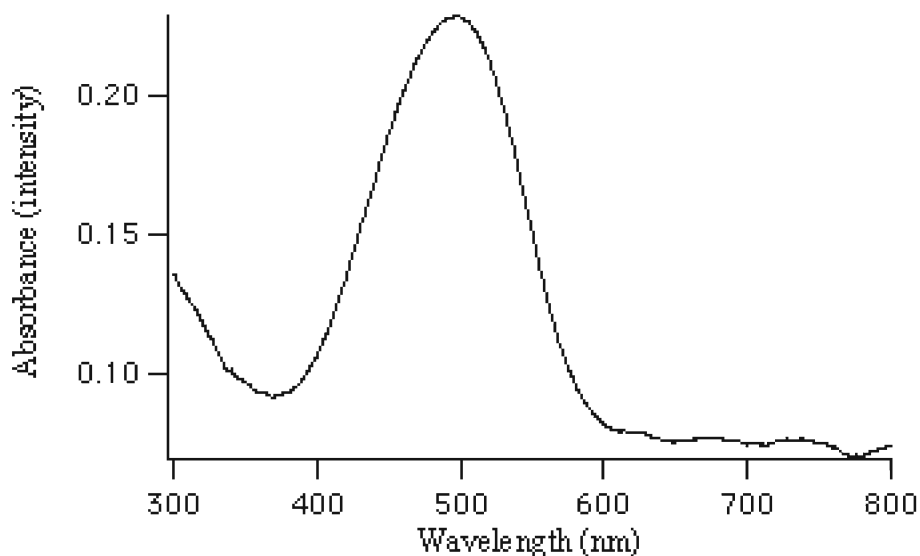


Figure 2: Absorption spectrum for Disperse Red 1 in methanol solution.

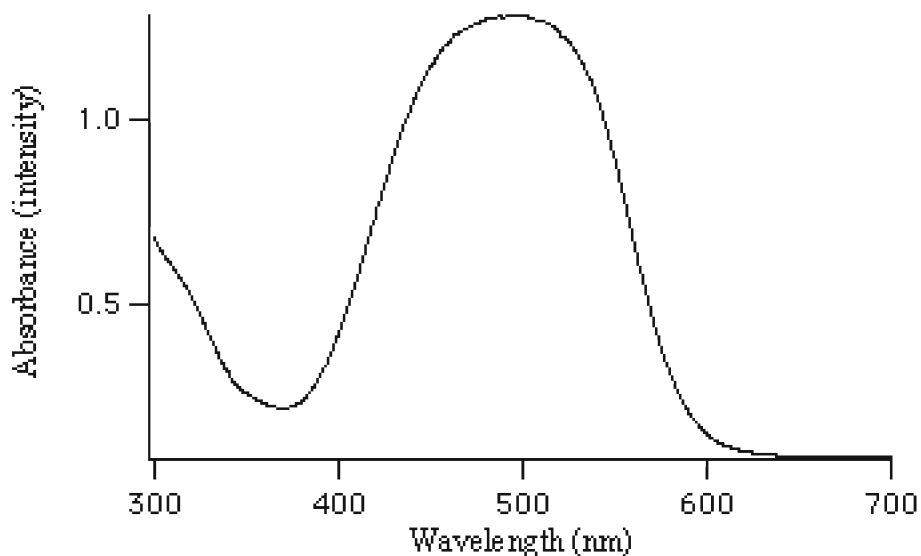


Figure 3: Absorption Spectrum for Drop Film of Disperse Red 1 in PMMA dissolved in Chlorobenzene. Note the incredibly wide absorption band.

Figure 4 shows bulk absorption and emission spectra for Bodipy. Figure 5 shows bulk absorption and emission spectra for SulfuroRhodamine 640. Figure 6 shows bulk absorption and emission spectra for Nile Red.

3.2 Fluorescence Spectra

A very dilute solution of disperse red in methanol was placed in a 1-cm cuvette for right-angle fluorimeter detection. Peak fluorescence emission at 550 nm was recorded, which is very close to the absorption peak at 500 nm. Because the fluorescence is shifted little from the absorption, it is termed 'blue fluorescence.' Fluorescence spectra were recorded for both 514 and 532 nm excitation wavelengths since these are the laser excitation wavelengths we expected to use.

We devised a method for taking fluorescence emission spectra of spin-coated disperse red in PMMA films. This was necessary because the fluorescence properties of dye in polymer differ from those of the dye in methanol solvent, due to differences in interaction between the dye and PMMA and methanol. Specifically, the local polymer matrix or solvent environment makes different emission (de-excitation) transitions accessible for energy emission.

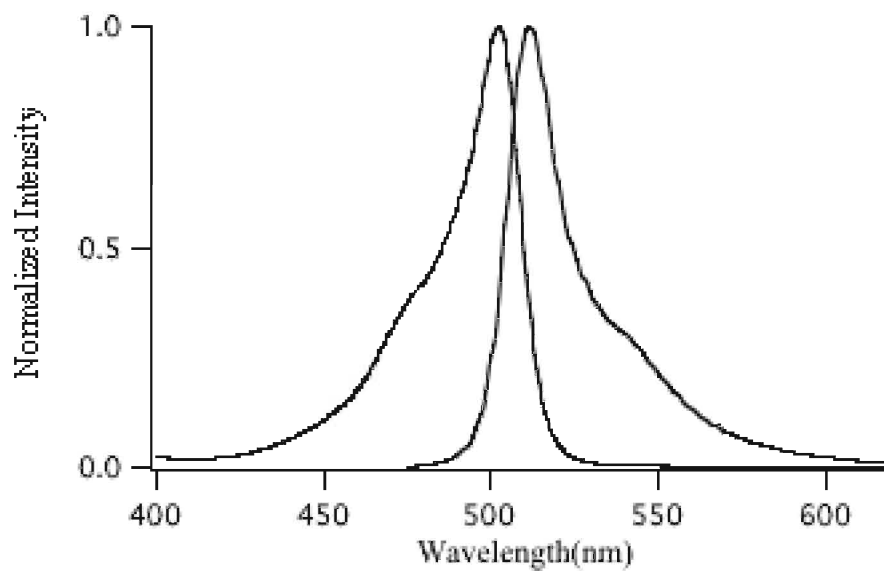


Figure 4: Absorption and emission spectra for Bodipy.

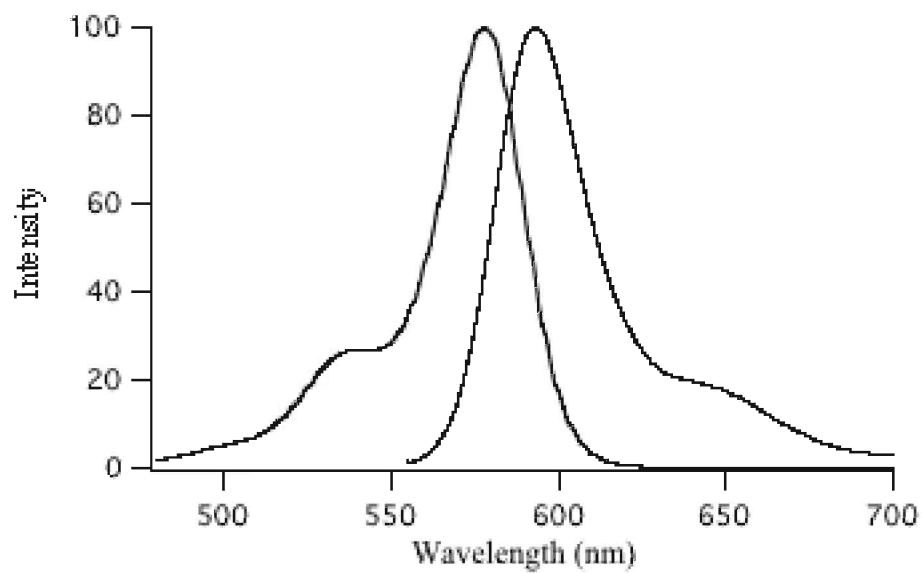


Figure 5: Absorption and emission spectra for SulfuroRhodamine 640.

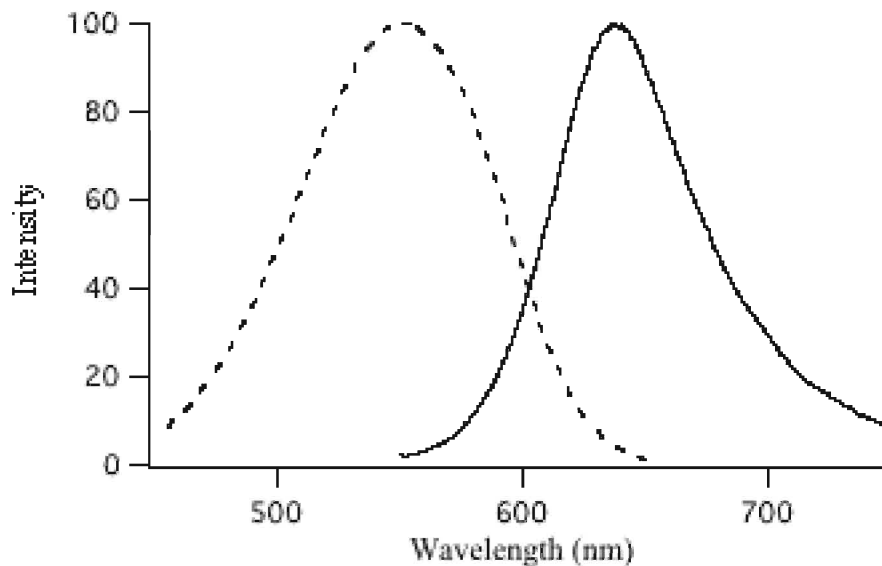


Figure 6: Absorption and emission spectra for Nile Red.

As shown in Figure 7, excitation wavelength has little effect on the peak fluorescence emission of Disperse Red 1 in methanol solution. For excitation at 500 nm (solid), 514 nm (dotted), and 532 nm (dashed), the central emission wavelength is 560 nm [66, 51]. Note that the emission intensity is normalized to one after background subtraction for ease of comparison between spectra.

The dotted profile in Figure 8 shows the fluorescence emission spectrum for a drop film of Disperse Red 1 in PMMA and chlorobenzene with 500 nm excitation [66, 106]. Again, the emission intensity is normalized to one after background subtraction for ease of comparison between spectra. Unlike the same dye in methanol solution (the solid line from Figure 7 reproduced here again as a solid profile), this spectrum has central emission wavelength of 550 nm.

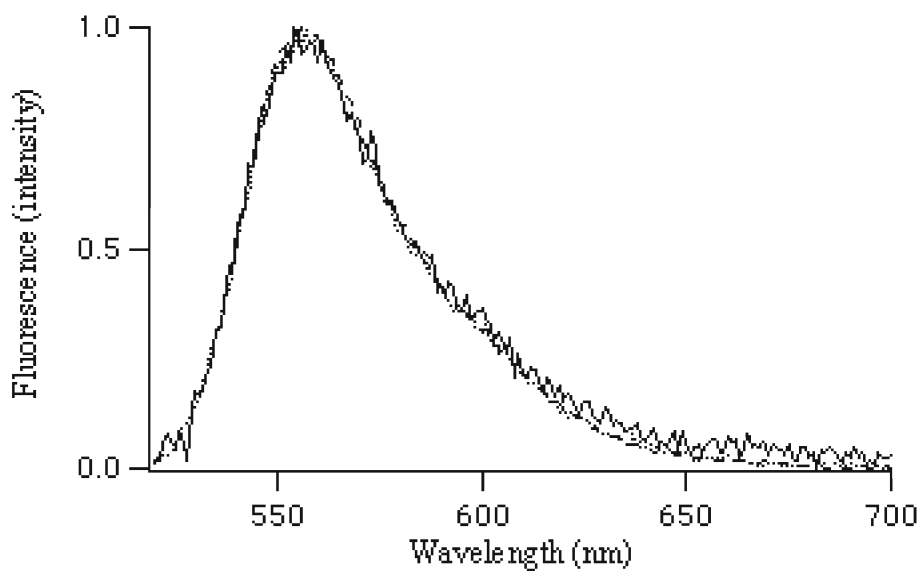


Figure 7: Fluorescence emission spectra for Disperse Red 1 in methanol solution.

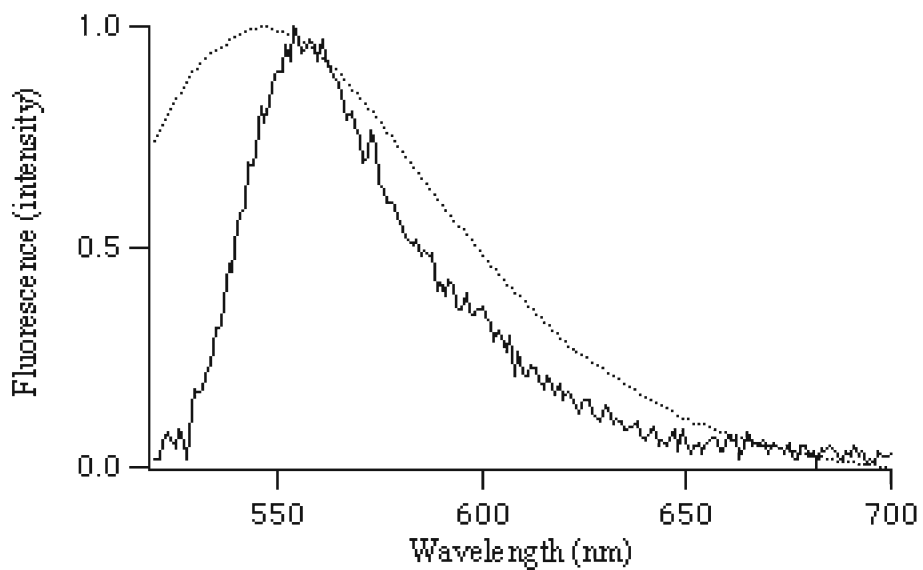


Figure 8: Fluorescence emission spectrum for a drop film of Disperse Red 1 in PMMA and chlorobenzene for 500 nm excitation (dotted), and emission for DR1 in methanol solution for 500 nm excitation (solid).

4 Fluorescence Experiment

Single molecule fluorescence and spectroscopy was detected with a scanning confocal microscope. A Hanbury-Brown-Twiss detection setup was used for measurement of the second order autocorrelation function to ensure that only one emitter was being detected [72]. Both autocorrelation and photon count rate were recorded as functions of time. Sample purity and concentration were critical to the success of these experiments, so sample preparation is described before a description of the fluorescence experimental apparatus is given.

4.1 Sample Fabrication

Dye molecules were embedded in a highly transparent polymethyl methacrylate (PMMA) polymer film of approximate 10-nm thickness. A solution of dye and PMMA in chlorobenzene (specifically, $\ll 1$ mg of dye per 100 ml and 1.2% by weight concentration of PMMA) were spin-coated onto a cover-glass plate. As a host polymer, PMMA has the advantage of permitting study of a wide variety of dyes. It also permits fabrication flexibility, because a variety of film thicknesses may be achieved. As measured by the confocal optical microscope described next, sample fluorescence density is that of about one emitter per square micron [72]. All dyes samples were prepared in a class 10 clean room facility, the envelope seal of which provided a totally leak-free environment. Blank films of PMMA without dye were also prepared for background fluorescence measurement.

4.2 Dye Selection

When we first arrived at LPQM, we expected to perform single molecule fluorescence measurements on Nile Blue in PMMA to complement the photon echo measurements we had begun on the same dye-polymer system. Since we had experimented with Disperse Red-1 (DR-1) and DR-11 in the photon echo experiment as well, we suggested performing single molecule fluorescence measurements of these dyes as well [66, page 114].

In agreement with previous work at LPQM, it was concluded that DR-1 does not provide sufficient fluorescence for detection as a single molecule. However, it was suggested that Nile Red and DCM were known to fluoresce and had spectra similar to that of DR-1. Spectral features to consider include the peak absorption wavelength and Stokes shift. For example, the short wavelength of

peak absorption of 480 nm for DCM was a concern. Since the dephasing experiment excites around 575 nm, with possible excitation down to only 550 nm with a change of laser dye, it is not possible to excite at much shorter wavelengths since the YAG itself gives a frequency doubled output of about 530 nm. Exciting far to the red of the DCM absorption would result in very low signal to noise in the photon echo experiment. This would be troublesome, regardless of whatever large single molecule fluorescence DCM might exhibit. Fluorescence also must fully extend beyond 565 nm to get past the dichroic mirror, as discussed in the next section. Nile Red, for example, has peak fluorescence near this peak cutoff, making spectral analysis difficult.

Since we brought DR-11, we decided to give it a try, even though its close relative DR-1 did not fluoresce. Other suggested dyes included Cyanine and Pyranine as well as Rhodamine-101, and Rhodamine-640, Bodipy, and Styryl-7 [66].

4.3 Experimental Setup

The 514-nm line of a cw argon-ion laser was used to excite molecules in the sample, as in Figure 9. The laser beam was spatially filtered through a single-mode fiber before being linearly polarized and sent to the inverted scanning confocal microscope. After reflecting off a dichroic mirror, the excitation beam entered an oil-immersion microscope objective of magnification $60\times$. The diffraction limited spot (FWHM lateral resolution of 320 nm [65]) looks effectively like a pinpoint at the center of the field of view when seen through the ocular. The beam passed through the sample glass substrate and was finally focused onto the sample, which had been positioned in the focal plane by the computer-controlled xyz piezoelectric translation stage. The same objective collected the fluorescence, which next passed through the dichroic mirror to be separated from any reflected or scattered incident light, and was finally focused into a pinhole of diameter $30\text{-}\mu\text{m}$ in the image plane [72].

Essential for confocal microscopy, a pinhole is used to select the portion of light corresponding only to the region of the sample hit by the laser spot. While the microscope objective collects light from a field of view much larger than the laser spot, a focusing lens projects this whole image onto a plane (the image plane) where a pinhole transmits only light from the excited region of the sample in which we are interested. Alignment of this pinhole is critical and very sensitive.

The dichroic mirror, pinhole, and notch filter work to reduce noise in the detected signal; to each fluorescence photon detected, there corresponds on the order of ten-thousand excitation photons

from the laser. Integral for coupling the laser to the dye-polymer system, the dichroic mirror also functions critically in permitting single molecule detection by preventing all but about a thousand excitation photons from traveling in the direction of the fluorescence emission. The pinhole further reduces noise, and critical adjustment of the notch filter ensures acquisition of good single molecule images.

A 514-nm holographic notch filter removed residual backreflected excitation light before the fluorescence was directed into the detection equipment: a Hanbury-Brown-Twiss setup comprised of two single-photon-counting avalanche photodiodes (APD's) to which fluorescence was equally directed by a 50-50 nonpolarizing beam splitter. Optical cross talk between detectors was suppressed by glass short-pass filters placed in front of each [72]. This optical cross talk occurs when the APD's absorb visible photons and re-emit infrared radiation as a ghost signal. Since each APD detects a single photon at a time, this signal is converted to a signal current by exciting electrons across a conduction gap. Occurring several times for signal amplification, eventually millions of electrons are flowing. Since each electron excitation results in the emission of an infrared photon, a huge burst of infrared radiation called a ghost signal is emitted by the APD for each visible photon detected. The ghost signal is correlated at zero time delay, adding to the noise associated with difficulty identifying the signature zero correlation intensity for single molecules [21]. The short-pass filters remove infrared radiation emitted by the APD's, thus decreasing the correlation at zero time delay.

The time interval between the detection of two consecutive photons is converted to voltage by way of the start-stop protocol of a time-amplitude converter (TAC) on a 100-ns scale. These voltages are recorded by a multichannel analyzer and accumulated into a distribution of time intervals to build $c(\tau)$, the time-interval histogram of raw coincidence counts. The second-order autocorrelation function $g^{(2)}(\tau)$ is well-approximated directly from the coincidence counts $c(\tau)$, given low detection efficiency and counting rate for short interphoton times considered here [72].

Not shown in the apparatus diagram of Figure 9 is the cooled CCD grating spectrometer used to measure the fluorescence emission spectra of single molecules. Cooled to -70 degrees Celsius to permit more sensitive measurement, the spectrometer was run through a computer interface which permitted adjustment of integration time, offered the option of taking multiple integrated spectra in series, and connected the spectrometer to the incident laser beam so that a single button could be pushed to stop spectrum acquisition and stop the laser light from hitting the sample. This flexibility was appreciated when new dyes of unknown photostability were studied; quick adjustments to integration time could be made before bleaching too many precious single molecules. Red and green beams from He-Ne and diode-pumped YAG lasers, respectively, of wavelengths 632.8 and 532

nm were aligned along the direction of the argon-ion green line for spectrometer calibration [66].

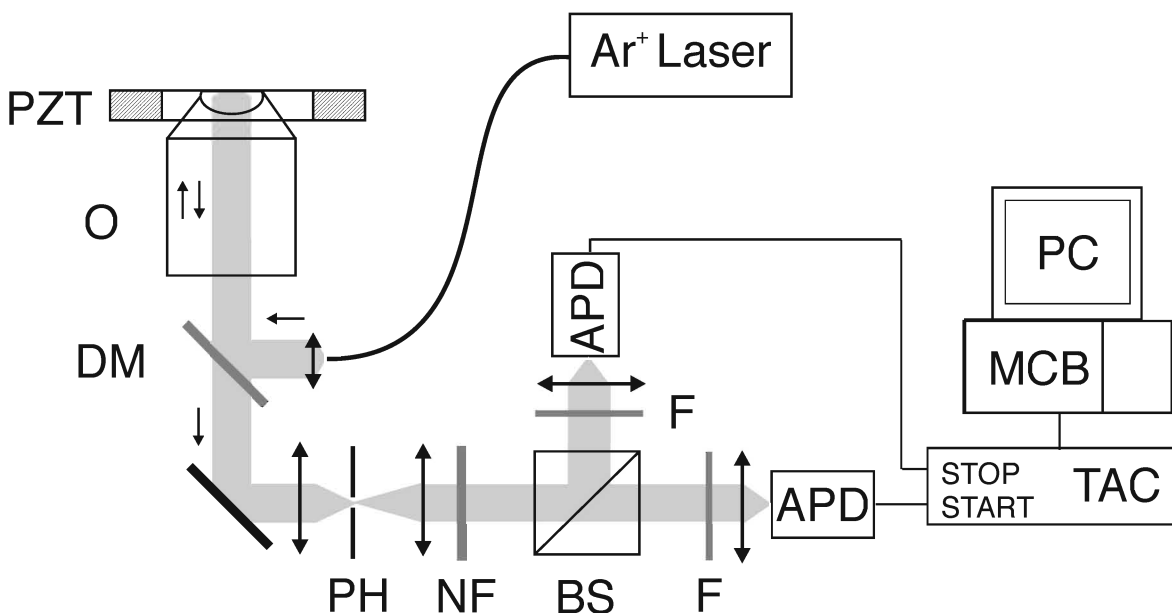


Figure 9: Hanbury-Brown-Twiss-type setup for second-order autocorrelation function measurement with scanning confocal microscope.

4.4 Data Acquisition Protocol

For each experimental run, three types of data were acquired. Single-molecule fluorescence, antibunching plots of the single-molecule correlation function, and time intensity plots monitoring photostability were obtained, as described below.

For each run taken, the spectrum recorded by the spectrometer was displayed on a PC using the Andor MCD software. This package also permitted electronic control and monitoring of the spectrometer temperature, which was set to -70°C for data acquisition. The integration time over which the spectrum was recorded could also be adjusted. For long-lived molecules with low fluorescence intensity, a series of four, ten-second scans were performed. For molecules that bleached quickly, several one-second scans were taken in rapid sequence.

The Maestro software package produced a $g^{(2)}(\tau)$ plot whenever the two APD's were running.

Essentially, the coincidence count histogram $c(\tau)$ is normalized to give the photon-pair correlation function $g_{(2)}(\tau)$. Specifically, since two fluorescence photons cannot be detected in an arbitrarily short time interval due to the finite radiative lifetime of the molecular dipole, there should be zero correlation between the photon intensities detected by the two APD's at zero time delay $\tau = 0$. This plot is therefore useful for verification of single molecule detection. The profile of the plot can also give information about the rate constants for transitions between ground, first excited singlet, and first excited triplet states, as shown in Figure 1 and discussed in References [72, 62].

A LabView program that recorded and displayed the intensity of the light detected by each APD as a function of time. Monitoring the dynamic time intensity plot allowed us to check whether the single molecules found were still fluorescing during data acquisition. When the intensity level suddenly dropped to zero, it was clear that the fluorescence had abruptly stopped. This was evidence that the fluorescence detected was in fact that of a single molecule, and the abrupt stopping of the fluorescence emission indicated that the molecule had been bleached.

Excitation at the 514-nm line of the Argon-ion laser with just over 2 μW of power (intensity of $2\text{kW}/\text{cm}^2$ at the sample) was used for most of the experiments described here. Besides the intensity and wavelength of the excitation light, the time intensity plot depends upon the photostability, an intrinsic property of the dye molecule under examination. In part for this reason, single molecule fluorescence studies of so many different dyes were performed.

5 Single Molecule Fluorescence Results

Single molecule fluorescence measurements were performed on thin film samples of the following dyes dissolved in chlorobenzene and spincoated into thin films with PMMA: Nile Red, Disperse Red, Cyanine, Bodipy, Styryl-7, Rhodamine-101, and Rhodamine-640. The final two dyes turned out to be two different samples of the same chemical structure. We present here correlation and time intensity plots as well as single-molecule emission spectra.

5.1 Correlation Plots

Raw correlation function data was recorded in the form of photon correlation count as a function of detection channel. The channel-number-to-time-delay conversion corresponds to the TAC settings and Stop Channel delay: 512 channels was a full scale of 100 ns with $\tau = 0$ around channel 225. The result is the nanosecond time delay scale seen on correlation function plots displayed here in Figures 10 through 16 [67]. Note that the correlation plots are not normalized; they display raw coincidence count $c(\tau)$ data. For the low photon count rates of these experiments, the raw coincidence count is approximately the correlation function, so $c(\tau) \sim G^{(2)}(\tau)$ [72].

The correlation function plot for cyanine in Figure 10 provides convincing evidence of single molecule fluorescence, since the correlation function intensity drops to background for no time delay between detection at the two APD's. While the plot seems quite noisy, we can identify this as the proper degree of shot noise; the square root of the average amplitude of the correlation function [34]. For a signal of amplitude fifteen, the shot noise is about four, so peak-to-peak noise fringes of height eight are expected [67]. For detection by photoelectric methods, the shot noise dominates the lowest order contribution to noise. There is an interesting exception in the case of single molecules, as almost all of the data presented here are of single quantum emitters. For small time delays, sub-Poissonian quantum statistics take effect [70].

Evidence of a single molecule in Disperse Red-11 trials is shown in Figure 11. Figure 12 shows the correlation function of a single Rhodamine-101 molecule. Note that although the overall intensity is much lower than for Cyanine or Disperse Red-11, the shot noise remains about equal to the square root of the signal amplitude. We have evidence of a single R-101 molecule in another trial, as shown in Figure 13. A final trial for R-101 with huge signal yields excellent evidence of single molecule detection in Figure 14.

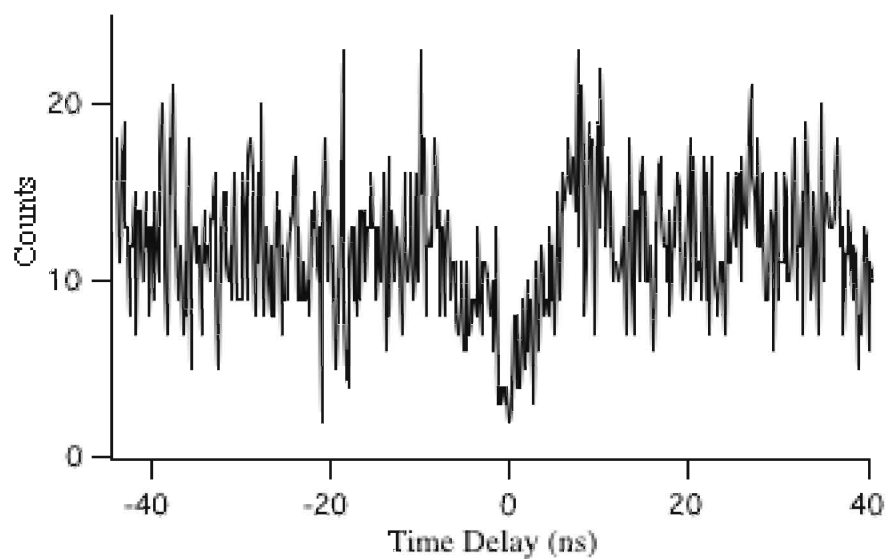


Figure 10: This second-order autocorrelation function plot for cyanine in PMMA indicates that fluorescence of a single molecule was being detected.

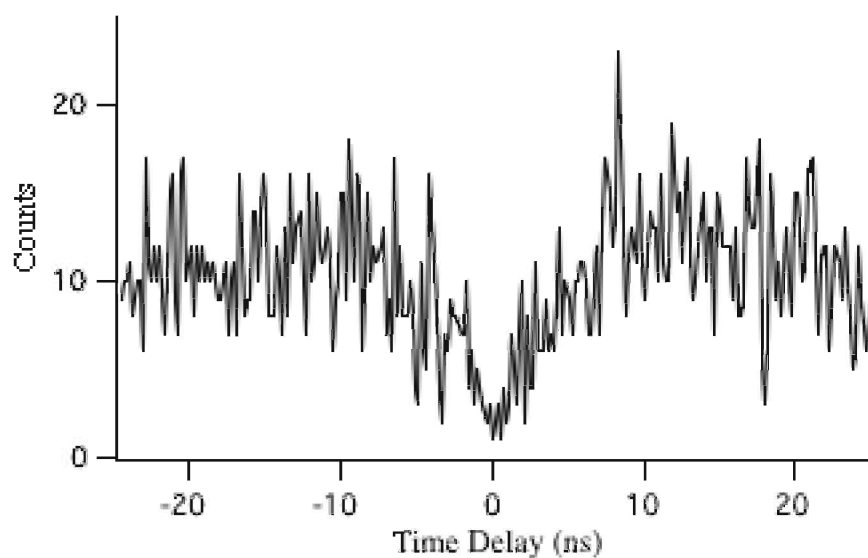


Figure 11: This second-order autocorrelation function plot for DR-11 in PMMA indicates that fluorescence of a single molecule was being detected.

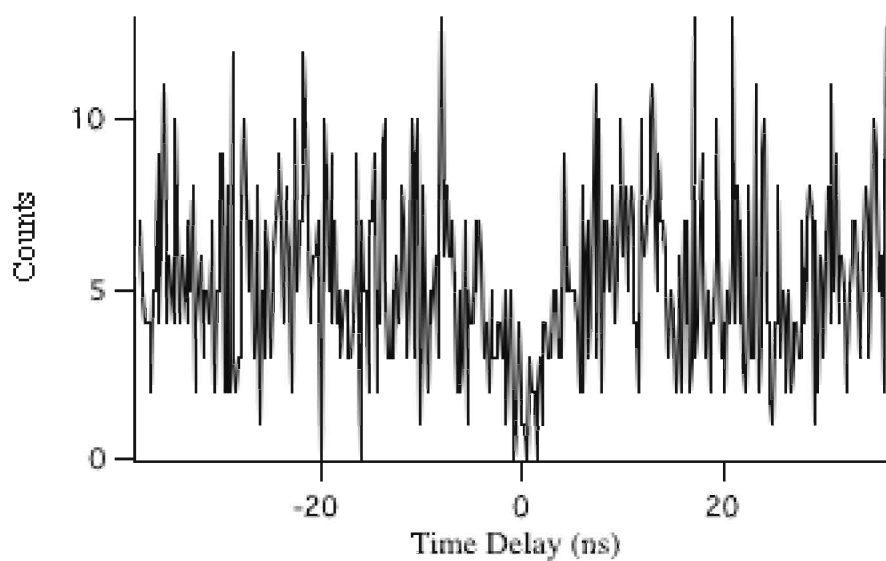


Figure 12: This second-order autocorrelation function plot for R-101 in PMMA indicates that fluorescence of a single molecule was being detected.

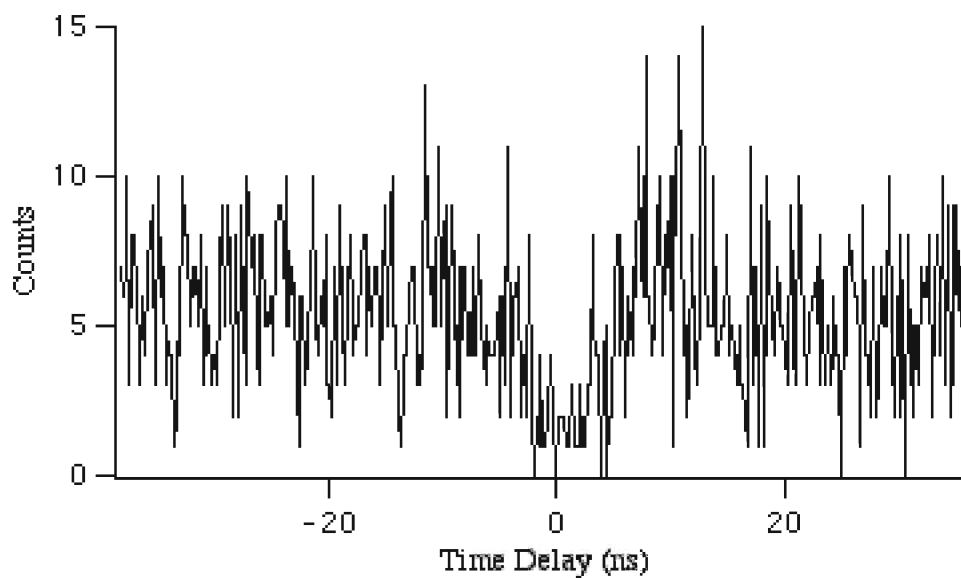


Figure 13: This second-order autocorrelation function plot for a second trial of R-101 in PMMA indicates that fluorescence of a single molecule was being detected.

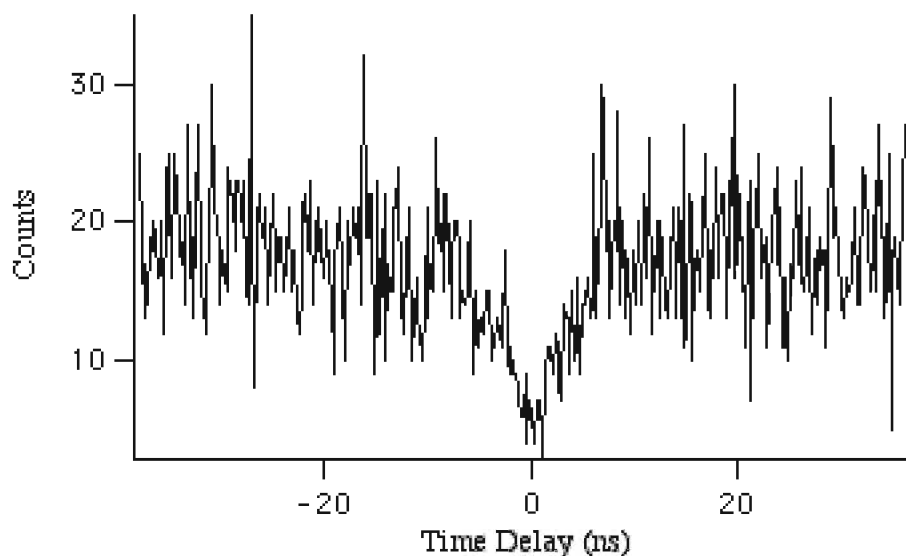


Figure 14: This second-order autocorrelation function plot for a third trial of R-101 in PMMA indicates that fluorescence of a single molecule was being detected.

Two interesting correlation function plots obtained for Styryl-7 are shown in Figures 15 and 16. These plots are of particular importance since the count level for the detected signal is so high. Figure 15 does not indicate the presence of a single molecule, since the intensity clearly dips to about ten, not background, for zero time delay. This is expected in the case of exactly two molecules, when the correlation function should drop to half its average value [72]. Figure 16 most likely indicates the detection of a single molecule since the intensity drops nearly to background for zero time delay.

5.2 Time Intensity Plots

Along with the correlation function plots, the time intensity plots are useful for suggesting whether a single molecule was observed during a trial. Raw time intensity data was recorded in the form of photon counts (per 100 ms integration cycle) as a function of time, from the start of the experiment. Both detection channels of the HBT interferometer were displayed dynamically and recorded. Therefore, a data file containing two streams of intensity values followed by a list of times (in microseconds) is obtained. Note that the time duration over which the time intensity data was recorded varies for each trial depending on the fluorescence lifetime of the molecule.

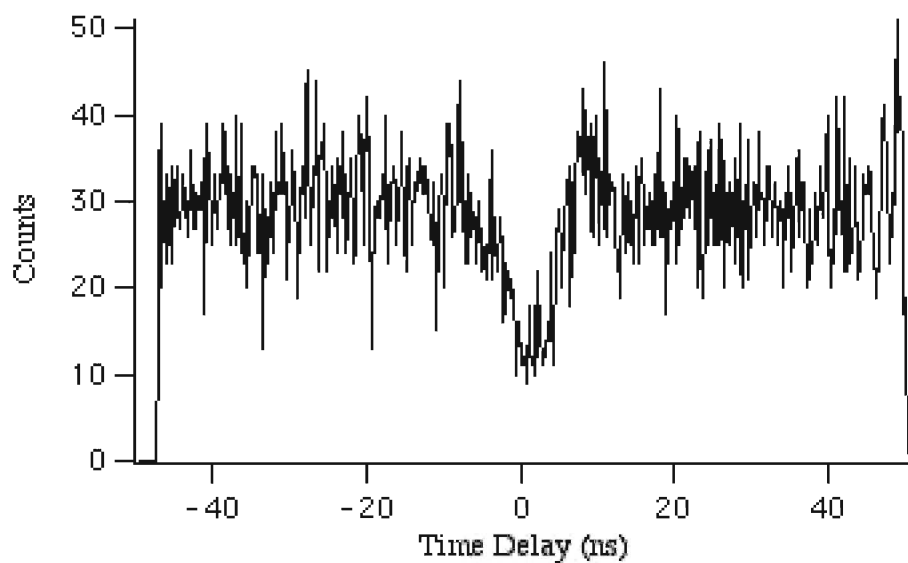


Figure 15: This second-order autocorrelation function plot for Styryl-7 in PMMA indicates that fluorescence of more than one molecule was being detected.

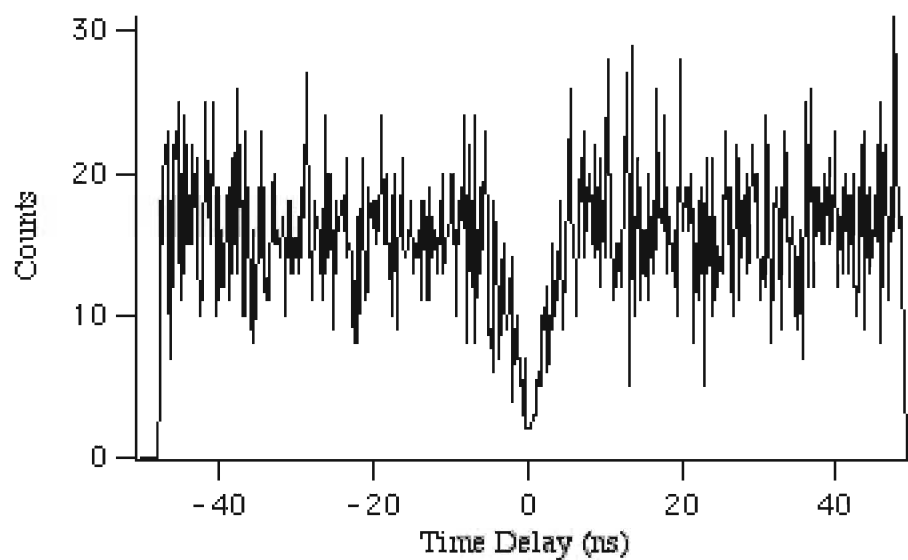


Figure 16: This second-order autocorrelation function plot for Styryl-7 in PMMA indicates that fluorescence of more than one molecule was being detected.

Bleaching occurs when the chemical structure of a molecule is altered, likely through interaction with the excitation photons and other chemical species in the environment, such as oxygen. Due to altered chemical structure, the molecule either no longer absorbs light of the excitation wavelength or, if it does still absorb light of that wavelength, it is no longer fluorescent in the wavelength range over which emission was detected. Oxygen quenching is the process by which the presence of oxygen air around the solution the fluorescence spectrum of which is being examined affects the first excited singlet state of the molecule, leading to a reduction in the molecular fluorescence yield. It is well known that the sensitivity of a molecule to oxygen quenching is closely related to the fluorescence decay time of the molecule [4].

A time intensity plot for the single Cyanine molecule for which we have a correlation function in Figure 10 is shown in Figure 17. The sudden drop in intensity from about 500 to background indicates that the fluorescence intensity of a single molecule was likely observed, since there is little chance that more than one molecule would bleach simultaneously.

Note that the detected photon count does not drop to zero even after the molecule has stopped fluorescing. There exists a nonzero background count of ten to fifteen, usually less than 10-percent the fluorescence signal count. This background exhibits contributions from random light as well as dark count random emissions from the APD's. This dark count exists due to thermal fluctuations, but it is usually on the order of 100 Hz (or photons per second). Since the fluorescence signal is usually greater than 1000 photons per second, this APD background contribution can reasonably be ignored.

Evidence of a single Disperse Red-11 molecule is shown in Figure 18. This time intensity plot agrees with the correlation plot for this trial given in Figure 11, supporting the evidence that a single molecule was detected. Notice the blinking behavior that occurs when the fluorescence stops for several seconds just after 200 s and just before 600 s.

The time intensity plot for R-101 is shown in Figure 19. The characteristic sudden drop in intensity from about 600 counts to background indicates that single molecule fluorescence was likely detected. The time intensity plot for the R-101 molecule described by the correlation plot in Figure 12 is shown in Figure 20. While the shape of this plot is similar to those already seen, with the sudden drop to zero intensity characterizing fluorescence of a single molecule, the comparatively short fluorescence lifetime should be discussed. Compared to the fluorescence intensity for other R-101 trials, this trial has single molecule fluorescence of high intensity (averaging 700 counts) and short lifetime. Comparison to results for other dyes, it seems that when the fluorescence lifetime of a molecule

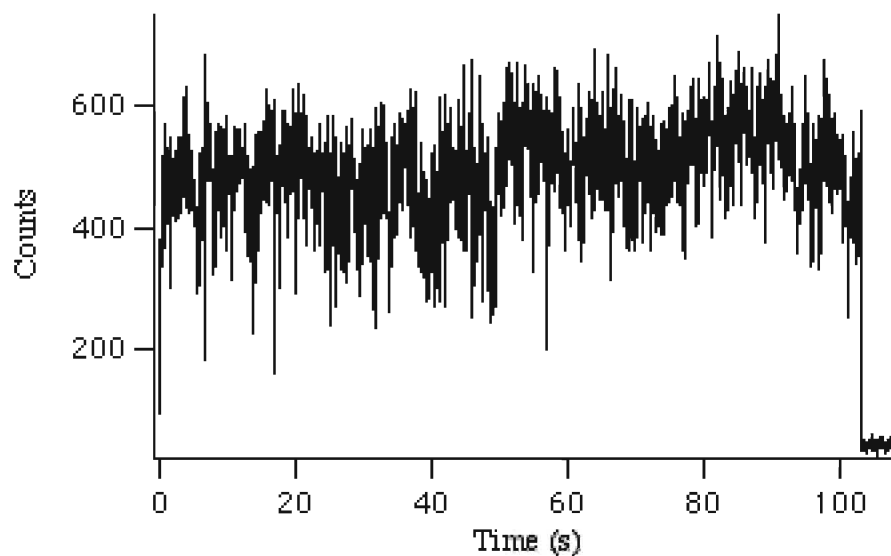


Figure 17: The sudden drop to zero intensity characteristic of single molecule fluorescence is visible in this time intensity plot for Cyanine in PMMA, agreeing with the single molecule evidence given by the correlation function for the same trial.

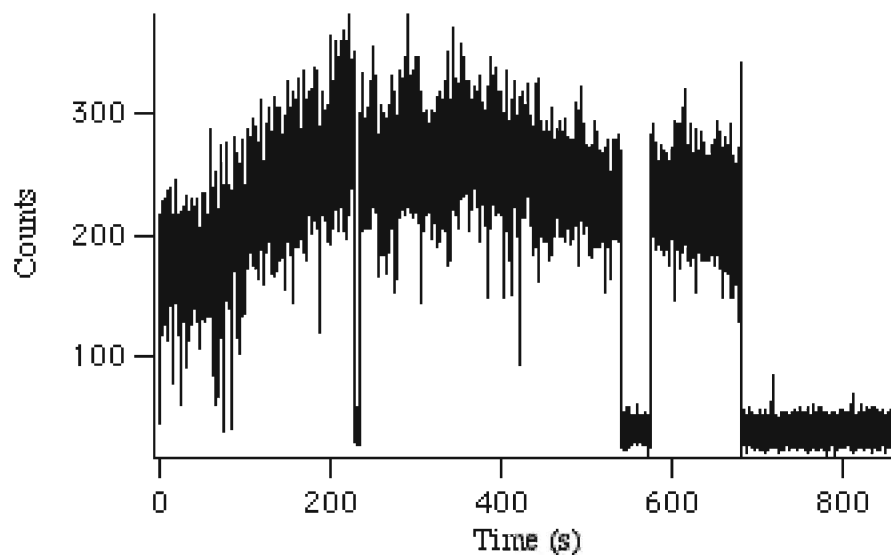


Figure 18: This time intensity plot for DR-11 in PMMA indicates that fluorescence of a single molecule was being detected.

is shorter than is typical for that species, the fluorescence intensity is larger than usual for that dye as well. Clearly, further studies of fluorescence lifetime as a function of fluorescence intensity are likely to yield interesting results. Preliminary observations suggest fluorescence lifetime to be inversely proportional to fluorescence intensity.

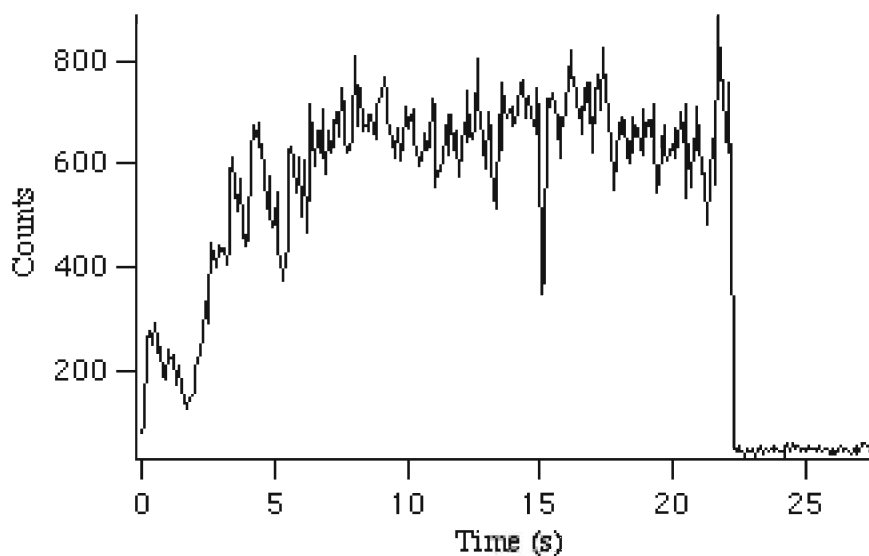


Figure 19: This time intensity plot for R-101 in PMMA indicates that fluorescence of a single molecule was likely being detected.

A time intensity plot for the R-101 molecule represented in the correlation plot of Figure 14 is shown in Figure 21. Together, these plots reveal that it is highly likely that the fluorescence of a single molecule was being collected.

The time intensity plot for Styryl-7 shown in Figure 22 agrees with the correlation plot of Figure 16 for the same trial in indicating that fluorescence from a single molecule was likely detected.

An unusual time intensity plot for R-640 is shown in Figure 23. Although R-640 and R-101 have identical molecular structures, the distinction is maintained here because samples were made from different stock containers. This plot for R-640 reveals that the fluorescence of several molecules was detected, as indicated by the stepwise decrease in the counts of fluorescence intensity detected. It is likely due to five or six molecules in the confocal region. In under three seconds, one molecule stopped fluorescing, and the fluorescence intensity decreased from 400 to about 275 counts. About 10 seconds later, a second molecule stopped fluorescing, and the pattern continues from there.

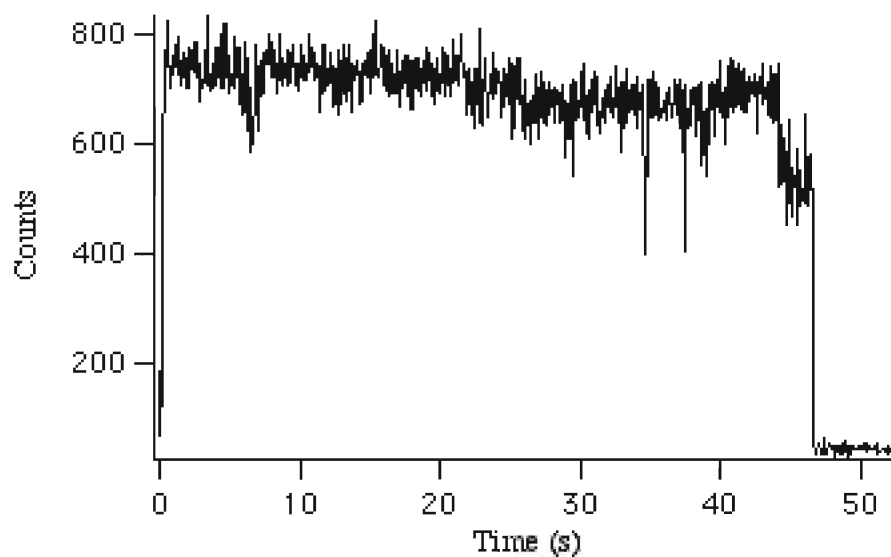


Figure 20: This second-order autocorrelation function plot for R-101 in PMMA indicates that fluorescence of a single molecule was being detected.

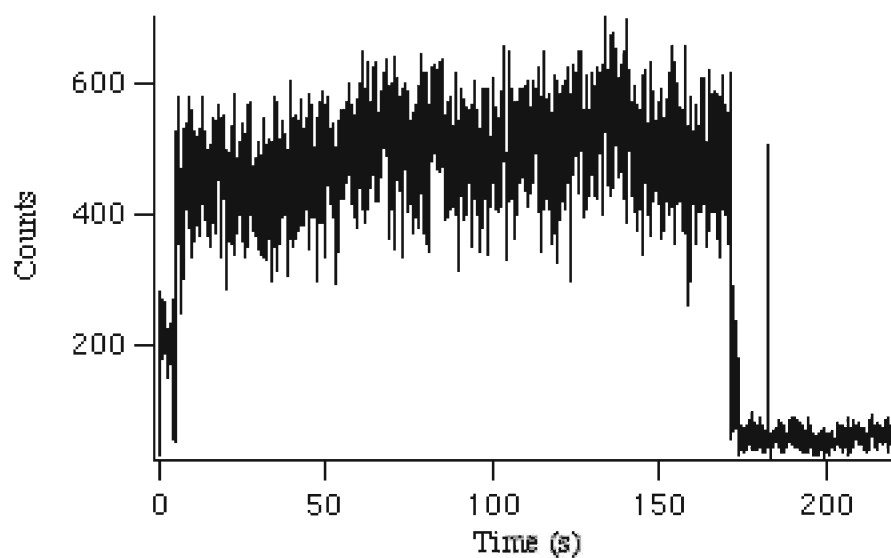


Figure 21: The sudden drop to zero intensity in this time intensity plot for R-101 in PMMA indicates that fluorescence of a single molecule was likely being detected.

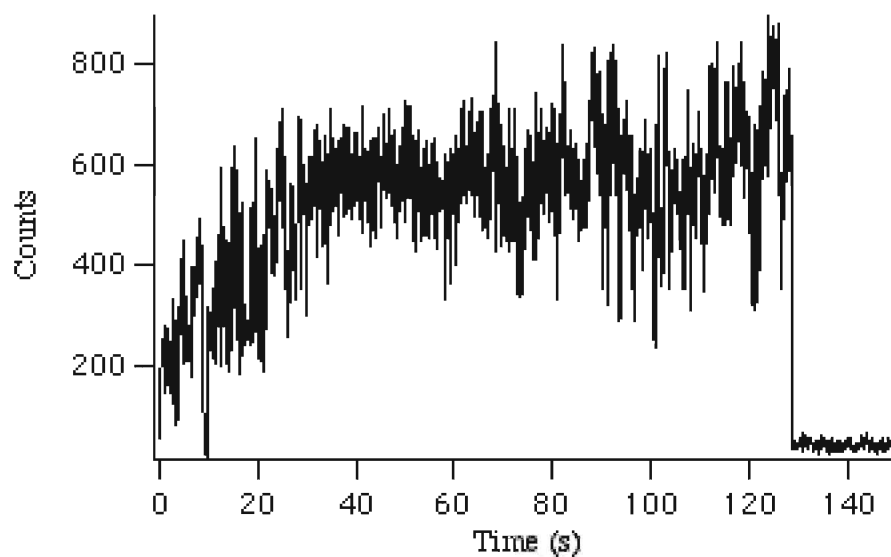


Figure 22: This time intensity plot for Styryl-7 in PMMA indicates that fluorescence of a single molecule was likely being detected.

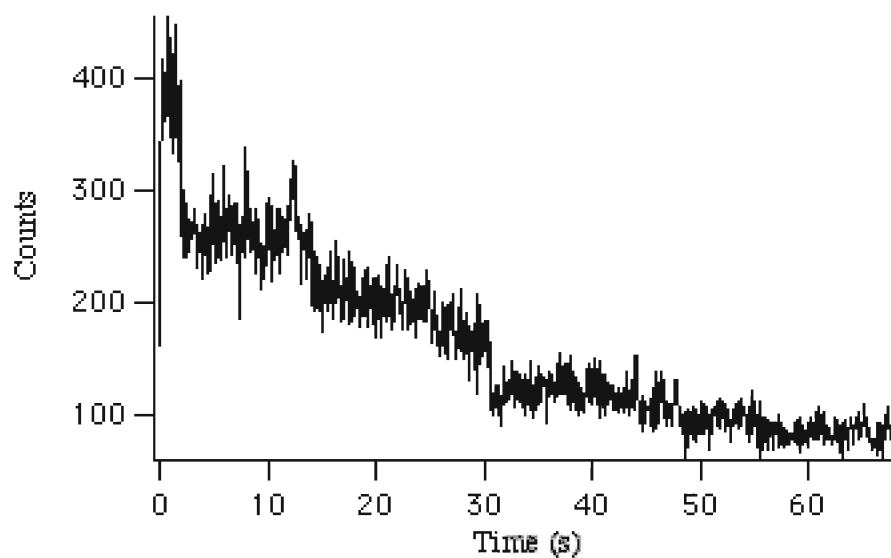


Figure 23: This time intensity plot for R-640 in PMMA indicates that fluorescence of several molecules was being detected.

Besides bleaching, blinking is another fluorescence intensity behavior observable in the time intensity plot. Occasionally, a molecule's fluorescence suddenly stops, only to return after a few seconds or less, as shown in Figure 18. This can occur when the molecule has entered the metastable triplet state T_1 of the first excited state. If the fluorescence intensity oscillates rapidly (which sometimes appears as an increased noise level), it is likely that the molecule is jumping randomly in and out of the dark triplet state. Since these intermittent nonfluorescent periods may be on the order of the detector repetition time or less, the full darkness of this state is not always measured. This explains rapid intensity fluctuations that may not drop to background during triplet excursions [70]. This is often observed just before the molecule bleaches, as seen in Figure 22.

Some time intensity plots, for example, R-640 of Figure 24, show a mixture of multiple molecules, blinking and bleaching. It is possible that this plot starts out with the fluorescence intensity of two molecules, one of which blinks at about 25 seconds, returns at 30 seconds and bleaches around 31 seconds. The remaining molecule continues to fluoresce for a second and then bleaches, too. While this type of observation is interesting, it is unfortunately difficult to verify and, ultimately, not very useful.

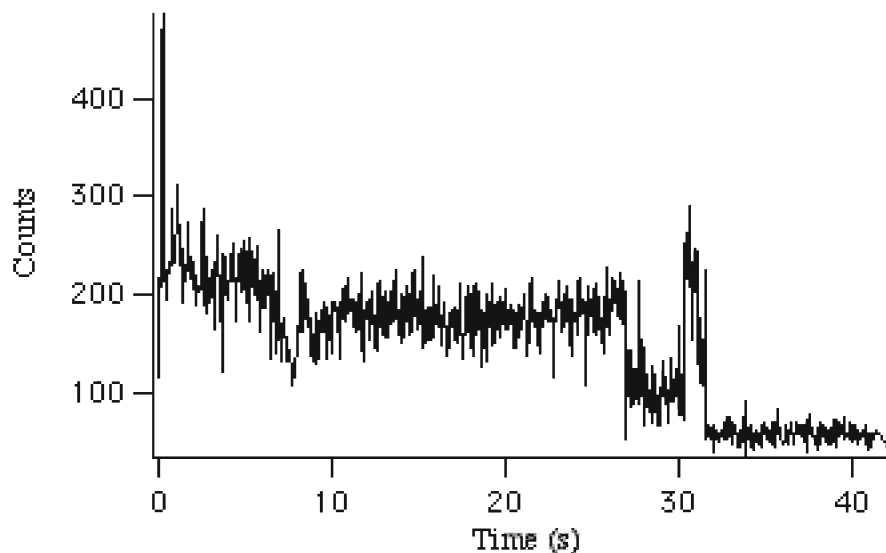


Figure 24: This time intensity plot for R-640 in PMMA indicates that fluorescence of two molecules was likely being detected. After the first molecule stopped fluorescing, the remaining molecule was blinking, on account of having gone into its triplet state.

5.3 Single Molecule Emission Spectra

Single molecule fluorescence of eight dyes was studied. These dyes included Rhodamine 640, Nile Blue, Disperse Red 11, Nile Red, Rhodamine 101, Styryl 7, and Bodipy. Photon echo measurements were performed on the first three dyes, along with Dipserse Red 1. Note that no single molecule fluorescence studies of this final dye were performed due to low photostability.

The first molecule studied emitted fluorescence for over forty seconds without photobleaching and also had a huge fluorescence yield, as seen in Figure 25. Four emission spectra were recorded, each with a ten second integration time. Peak emission wavelengths for the four spectra are 568.2, 581.0, 581.1, and 580.6 nm with dephasing times of 9.3, 8.8, 8.8 and 9.1 fs, respectively, which average to 577.7 nm and 9.0 fs over all four runs for this molecule.

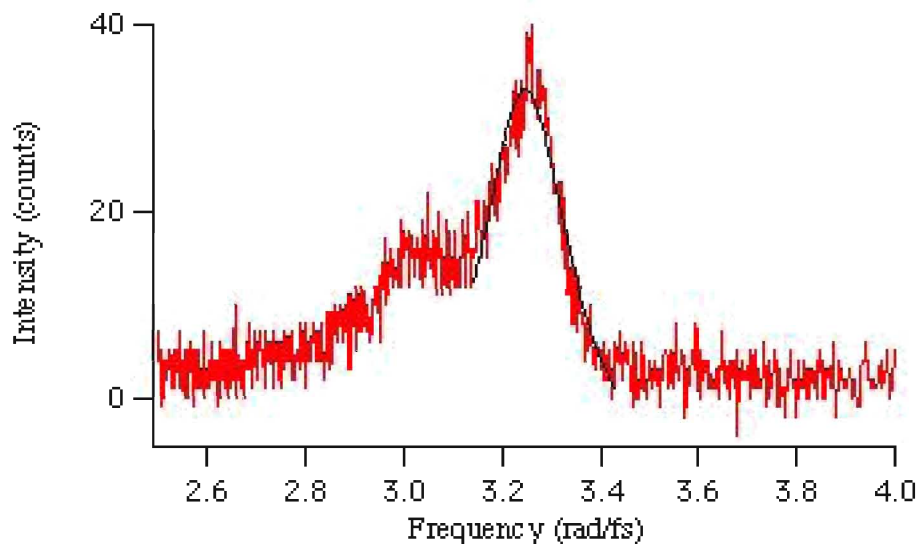


Figure 25: Emission spectrum for a long lived, single cyanine molecule with high fluorescence yield (lifetime over forty seconds before photobleaching).

The second molecule studied had average central emission wavelength 562.5 nm and dephasing time 8.0 fs. While this molecule had comparably lower fluorescence yield, as shown in Figure 26, it did fluoresce for over thirty seconds before photobleaching. Peak emission wavelengths were 563.2, 559.9, and 564.7 nm and the corresponding dephasing times were 11.1, 7.6, and 5.2 fs.

Over thirty emission spectra of Nile Red were acquired and it was observed that this dye had high fluorescence yield but relatively low photostability, as photobleaching often occurred in under ten

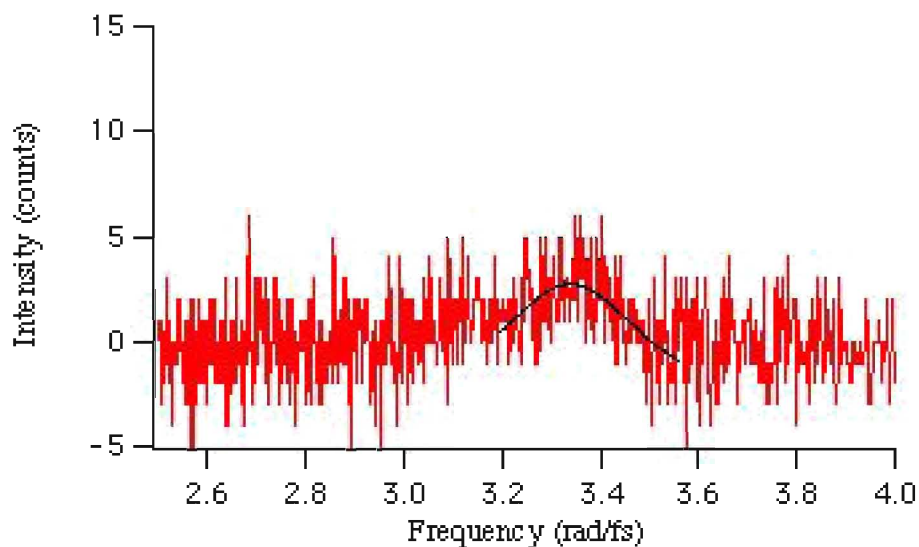


Figure 26: The single cyanine molecule for which this plot is the emission spectrum fluoresced with low fluorescence yield for about thirty seconds before photobleaching.

seconds. Little analysis was performed on the emission spectra obtained, as the spectra were cut off by the 580-nm dichroic filter, as shown in Figure 27. It is possible that accurate values for the central emission wavelength and dephasing time could be obtained using more sophisticated fitting techniques. The Lorentzian fit shown in Figure 27 most likely gives too narrow a FWHM and therefore, too long a dephasing time. Similarly, the peak emission wavelength suggested by this fit is likely shifted to longer wavelength than the true peak.

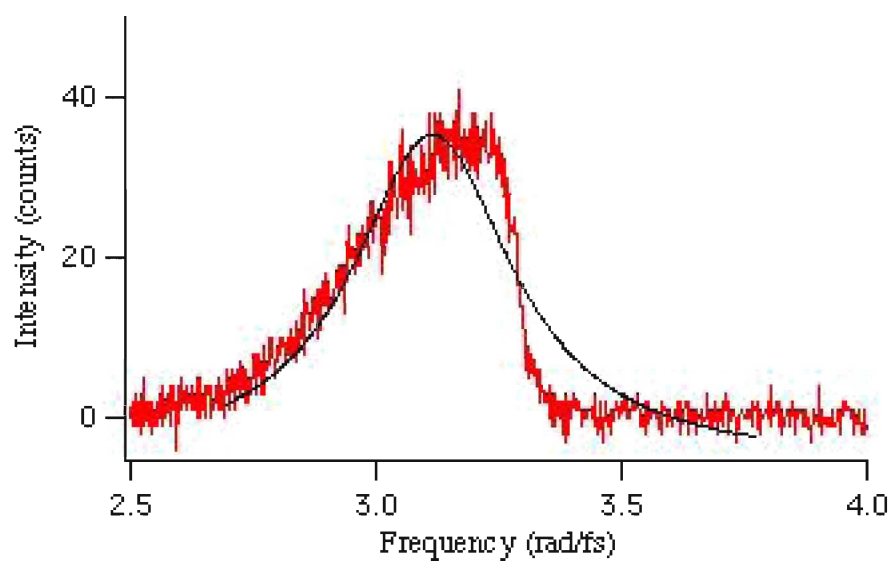


Figure 27: The single Nile Red molecule for which this plot is the emission spectrum fluoresced with high fluorescence yield. Unfortunately, its emission spectra is cut off by the 583-nm dichroic filter.

6 Photon Echo Experiment

Study of ultrafast optical dephasing in physical systems is important to increasing understanding of matter-photon dynamics. Specifically, the microscopic dynamics of materials can be probed by studying the $S_1 \rightarrow S_0$ transition relaxation processes they undergo after light excitation with temporally incoherent 10-ns nanosecond laser pulses. Since the relaxation times of condensed matter such as liquids and solids are often shorter than picoseconds, ultrashort pulses are used to obtain higher time resolution [18]. Measurements of the longitudinal relaxation time T_1 and ultrafast homogeneous transverse relaxation (dephasing) time T_2 are of particular interest.

Tang and collaborators first used the equal-pulse intensity-correlation technique to measure transverse relaxation times shorter than the excitation pulse widths. Similarly, Fujiwara and collaborators experimentally confirmed theoretical predictions that four-wave mixing including photon echoes with temporally incoherent (broad-spectrum) light can give ultrahigh time resolution (on the order of the femtosecond homogeneous transverse relaxation time of condensed matter), as determined by the excitation field correlation time, regardless of the excitation pulse width [18].

In the past twenty years, important research on absorption and ultrafast dephasing has been performed on the oxazine dyes Cresyl Violet and Nile Blue, with thorough measurements conducted over an extensive range of excitation wavelengths, time scales, and temperatures [18]. For example, it is well-known that dephasing times are generally shorter for excitation at bluer (shorter) wavelengths due to intramolecular relaxation processes [18]. The theoretical work done to explain and interpret those measurements will prove useful here.

Ultrafast laser pulses or broadband incoherent light was used in time-delayed degenerate four-wave mixing (DFWM) measurements to determine the time constants for optical dephasing. When dephasing times T_2 are long compared to the light source field correlation time τ_c , the extended tail of the DFWM signal as a function of time delay permits determination of the dephasing time [18]. For dephasing times commensurate to or shorter than the light source field correlation time, a measured shift in the peak scattered light intensity from zero time delay gives a dephasing time estimate.

Measurements have revealed and numerical simulations have confirmed a new effect in optical dephasing time measurement: rapid time-delay sinusoidal oscillation variations or interference fringes on the DFWM signal [23]. Comparison of the measured modulation depth with numerical sim-

ulations reveals that this technique is useful for estimating dephasing times shorter than 10 fs. Therefore, this technique is useful for measuring dephasing times using tunable incoherent light when the time domain is limited by the duration of laser pulses. As expected, this technique proves useful for measuring optical dephasing times of samples with broad homogeneous linewidths at high temperatures in highly interactive environments [23].

6.1 Sample Fabrication

We discuss here sample chemistry, including the specific protocol and problems dissolving polymer. Slide cleaning and fabrication of drop and spincoated films is also covered.

Although our dephasing measurements were ultimately performed on drop films of Nile Blue, Disperse Red-11 and Rhodamine-640 in PMMA, our first attempts at making solutions for films began with Nile Blue (NB) in PVOH and water. According to the general protocol, Nile Blue was first dissolved in water, and solid polymer powder was added. The solution was prepared in a 25-mL Erlenmeyer flask and covered with Parafilm to prevent evaporation during storage [68, page 120].

In an effort to fabricate thicker films, we added more polymer than Carl's old recipes had recommended. Instead of 1.2 g PVOH, we added 1.8 g PVOH to 8 mg NB dissolved in 20 mL Millipore water. The next day, we removed about 1.2 mL of solution, decided it was not thick enough, and added 0.6 g of PVOH. We then had difficulty getting the polymer to dissolve, so we removed the Parafilm, added a magnetic stir bar, and covered the flask with aluminum foil.

We then placed the flask in a water bath (later replaced with clear mineral oil) on a magnetic hot plate. A thermometer in the water bath permitted monitoring of the system temperature. We heated the solution to 80 deg C while it stirred. Since the flask was covered with foil, the water that evaporated from solution condensed in the cooler upper part of the flask that was not surrounded by the heated water bath, eventually returning to solution.

Synthetic sapphire slides are used for samples on which optical measurements are to be performed. Sapphire has chemical formula Al_2O_3 , and because the ground to first excited state transition for aluminum and oxygen is satisfied by absorption of photons in the UV, the slide's absorption will not interfere with detection of optical processes occurring in the sample adhered to the slide. That is, the slide has no absorption in the visible because the large transitions are satisfied by UV absorption, and other smaller transitions are in the IR [68, page 100].

The sapphire slides have good thermal conductivity, so we can be sure that when the vacuum chamber containing the sample on the slide is cooled down, the slide is also cooled to this temperature. Since the slide has a large surface area in contact with the sample, we can be sure that the sample itself is also cooled. This is important for accurate low temperature measurements.

A slide to be cleaned is first placed in soap and Millipore water, then acetone to remove the film. It is then transferred with tweezers to Millipore water for acetone removal before being cleaned with a mixture of sulfuric acid and hydrogen peroxide colloquially known as piranha bath. The slide is dipped in this bath for only thirty seconds, as it is a strong chemical that could remove the coating on the slide. The slide is then again rinsed in Millipore water, dipped in acetone, and then dried with lens tissue. If water spots remain on the slide, drops of methanol are placed on the slide. Then the slide is again dried with lens tissue before being placed on lens tissue in a closed plastic petri dish. Sometimes, if lens tissue seems to deposit unwanted dust on the slide, dry nitrogen gas or canned compressed air is used to blow the slide dry after methanol treatment.

While Carl Grossman had extensive experience with making and using drop films in past dephasing experiments, our first drop films were made by Daniel Sproul in Summer 2001. This method consisted of filtering solution with Cameo 0.5- μm disposable nylon filters before dropping one drop of Nile Blue in PVOH and water onto a slide. Care was taken to ensure that no drops of solution containing air bubbles were placed in the slide, as it was found that these air bubbles created inhomogeneities in film thickness [68, page 124]. After placing the slide in a petri dish with the lid cracked open to allow for more rapid solvent evaporation, the slide was left undisturbed for at least 24 hours [68, page 121]. During the dry time, the water evaporated and the sample adhered to the slide.

At first, slides were placed under an incandescent desk lamp for quick drying. Usually slides were allowed to dry overnight in a large desiccator, the top of which was not fully sealed. When high humidity became a problem, slides were dried in a closed desiccator to prevent moisture from the air from condensing on them.

A common difficulty with drop films is that too much evaporation would occur in the center of the slide, so the resulting film is thickest in a rim around the edge. Evaluation of film quality mainly consisted of checking for uniformity of film thickness. A ridged pattern seen in the film when the slide is held up to light indicates that the changes in film thickness are on the order of the wavelength of light; specifically, each stripe in the ridged pattern represents a change in film thickness equal to one wavelength (about 550 nm) of light. The optical density of films was

measured using a Jasco UV/VIS-550 spectrophotometer in the inorganic chemistry laboratory [68, page 121].

Our first spin-coated films were made by Daniel Sproul. He experimented with Nile Blue in PVOH and water, using the spin-coater Peter Collings had graciously lent us. The drop film fabrication procedure was followed, except that the blank slide was placed on the spincoater head before filtered drops of solution were added. Then the program specifying acceleration, spin time, and deceleration was run, having already been entered before the slide was present.

Daniel found that thicker films, important for increased optical density and getting a detectable signal, could be made by decreasing the acceleration rate. It was also found that coating the entire film with dye before spinning it increased uniformity of film coverage [68, page 121].

6.2 Experimental Setup

A frequency-doubled Q -switched Nd:YAG laser producing pulses of width 10 ns and peak power 2.3 kW at 532 nm pumped a static dye cell containing the organic laser dye Rhodamine-590. A back-mirror reflected some of the Rhodamine-590 fluorescence emission back through the dye cell to create amplified spontaneous emission of approximate correlation time 100 fs [18]. This emission created an incoherent beam which was then spatially filtered, collimated, and polarized before being sent into the DFWM experiment, as shown in Figure 28.

The light beam was split into two excitation beams E_1 and E_2 and sent along two arms of the DFWM interferometer. A time delay τ between the beams was controlled as follows: the path length of one beam was adjusted using a precision stepper-controlled stage to move the mirrors determining the beam's path. The 50-nm translation resolution of this stage allowed time delays with 0.33-fs increments. The relative polarization of the two beams was adjusted with a wave-plate and polarizer [23]. Directed along parallel paths, the beams were focused down to a small spot size and recombined on the sample film at an approximately five-degree angle. The echo signal can have a contribution from thermal gratings, which can be reduced if the two beams have crossed polarization.[27] In the case of thin, PMMA films there was no apparent change in the echo signal between parallel and crossed polarizations, possibly due to the thermal stability of the sapphire substrate.

The dye-polymer film on a thin sapphire slide was mounted inside the optical head of a close-loop

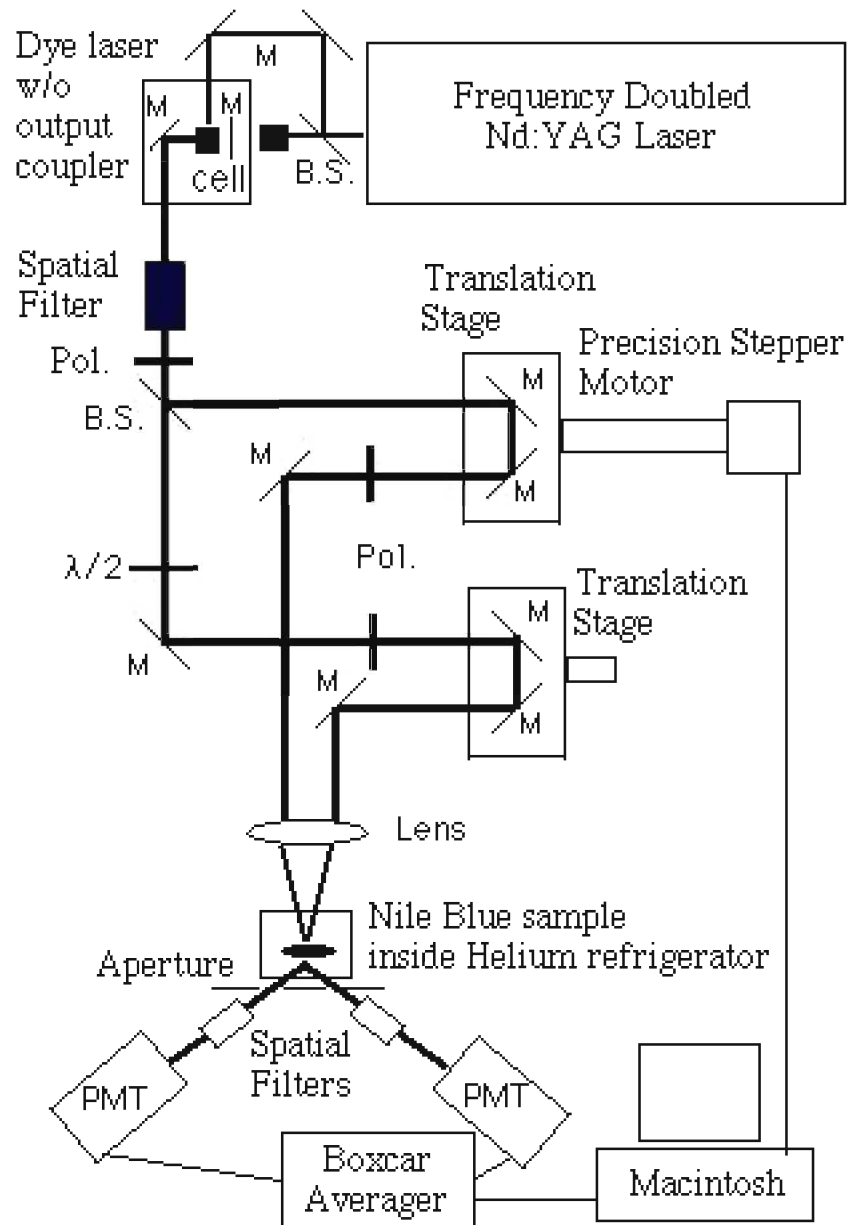


Figure 28: A schematic of the two-beam, time-delayed degenerate four wave mixing (DFWM) with incoherent light used in the photon echo experiment.

Helium refrigerator. Transmitted beams along the incident \vec{k}_1 and \vec{k}_2 directions were blocked. Noise and other stray reflections from specular scattering were removed by placing small apertures before spacial filters along the dephasing signal scattering directions $2\vec{k}_1 - \vec{k}_2$ and $2\vec{k}_2 - \vec{k}_1$, as shown in Figure 29.

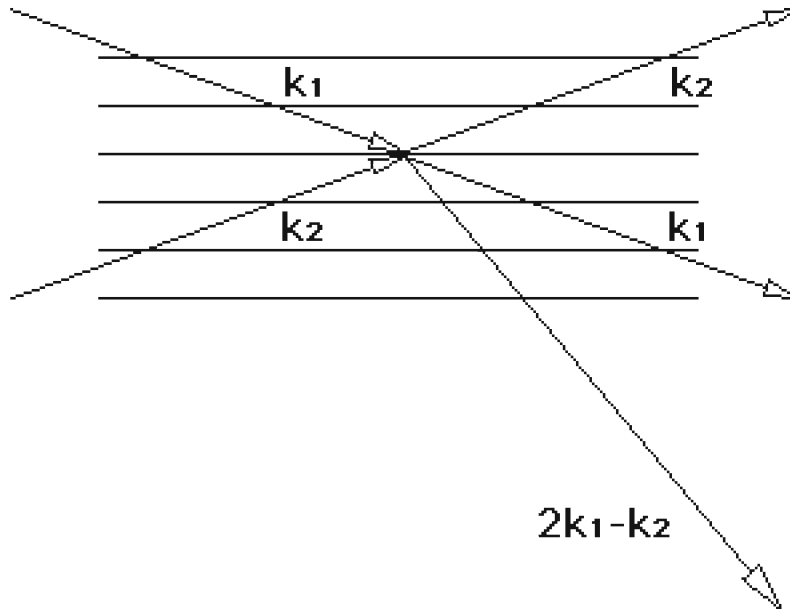


Figure 29: Beam geometry for the time-delayed DFWM experiment. Excitation beams along \vec{k}_1 and \vec{k}_2 yielded scattered signal in the $2\vec{k}_1 - \vec{k}_2$ direction from which dephasing measurements were made. The $2\vec{k}_2 - \vec{k}_1$ direction is not shown, but is symmetrically related.

The photomultiplier tubes (PMT's) and spatial filters were aligned to detect scattered signal intensity in the $2\vec{k}_1 - \vec{k}_2$ and $2\vec{k}_2 - \vec{k}_1$ directions. This was accomplished using an alignment laser collinear with the predicted signal paths. The signals were averaged with boxcar integration electronics and read by the computer where they were recorded as a function of time. Essentially, we measure the interference of light scattered by the film.

6.3 Experiment Difficulties

After the experiment was completely built and aligned precisely, we still had difficulties consistently measuring the signal. This indicated a need to continue refining our sample fabrication protocol, but there also existed hardware difficulties with the dephasing experiment itself. The stability of

the incoherent light source was called into question, and the focusing lens just before the mounted film sample created many reflections. Some strong reflections were aimed in the predicted signal directions. We eventually found that turning the sample so that it was not normal to the incident beams directed these strong reflections away from the signal paths.

In the course of resolving the problem of focusing lens reflections, we replaced this focusing lens with another with anti-reflective coating. To make sure the new lens was positioned so the beams focused on the sample and yielded an interference pattern at zero time delay between the incident beams, we replace the sample with a pinhole. We undertook a systematic procedure for adjusting the pinhole with a micrometer while varying the time delay to find a tiger stripe interference pattern of the beams indicative of the beams overlapping at the pinhole (which we hoped was close to the location of the sample film).

Once sample was back in place, we adjusted the pinholes at the entrances to the detectors only slightly; instead it was the mirrors directing the beams parallel too each other after the interferometer that were used to adjust beam height and horizontal position. Since no interference effect visually showed the beam overlap on the sample, a series of mirror and lenses was used to create a telescope for viewing the beam overlap on the sample.

7 Photon Echo Results

Photon echo experiments were performed on dye-polymer films of Nile Blue in polyvinylalcohol (PVOH) and Rhodamine-640 in polymethylmethacrylate (PMMA) at low temperatures (between 20 and 160 K). In all of these experiment, we found that the dephasing time was shorter than the coherence time of the incident beam and in most cases the dephasing time T_2 was determined from the peak shift in time between the scattered light intensity along $2\vec{k}_1 - \vec{k}_2$ and $2\vec{k}_2 - \vec{k}_1$. A typical data set is shown in Figure 30 [23].

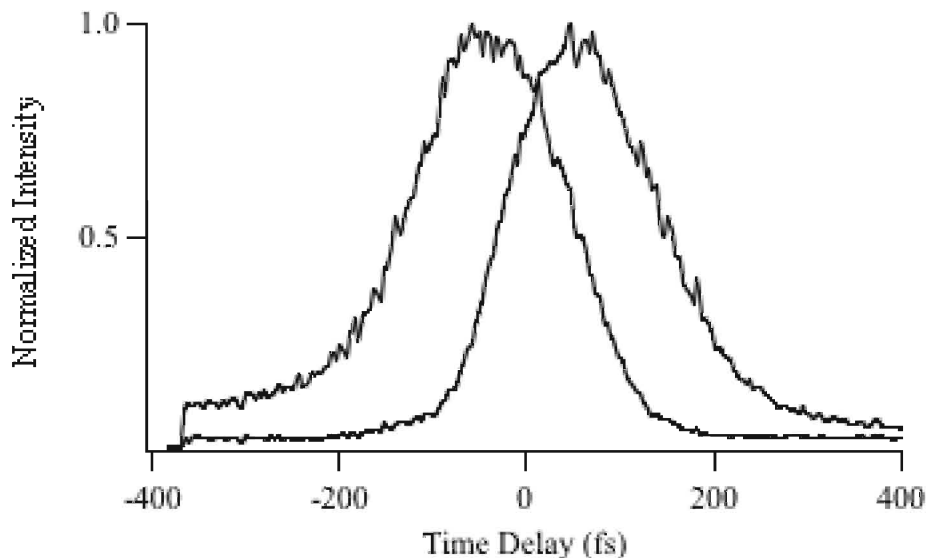


Figure 30: Scattered intensity as a function of time delay for incident incoherent light of central wavelength 575 nm. For this sample, Nile Blue in PVOH drop film at 12 K, the peak shift of 94 fs yields a dephasing time of approximately 47 fs.

For Nile Blue samples, the incoherent source had a central wavelength of 575 nm, which is on the blue side of the 620 nm central absorption peak. Measurements were made at 12K (Figure 30), 72K, 120K and room temperature (Figure 31). As sample temperature increases, peak separation decreases until none can be resolved. This finding agrees with other reported measurements [18, 23] The room temperature measurement yielded featureless DFWM signals, with a peak shift smaller than the limit of resolution for the peak scattered light intensity. Thus there was no measurable peak shift and we can conclude that these samples exhibit dominance of homogeneous broadening at high temperatures [74]. It is also suspected that a fast thermal grating effect may be minimizing the signal intensity; although this effect should have little quantitative influence on dephasing time

calculation, it may be responsible for washing out the interference fringes that would otherwise possibly be present [23, 18, 21].

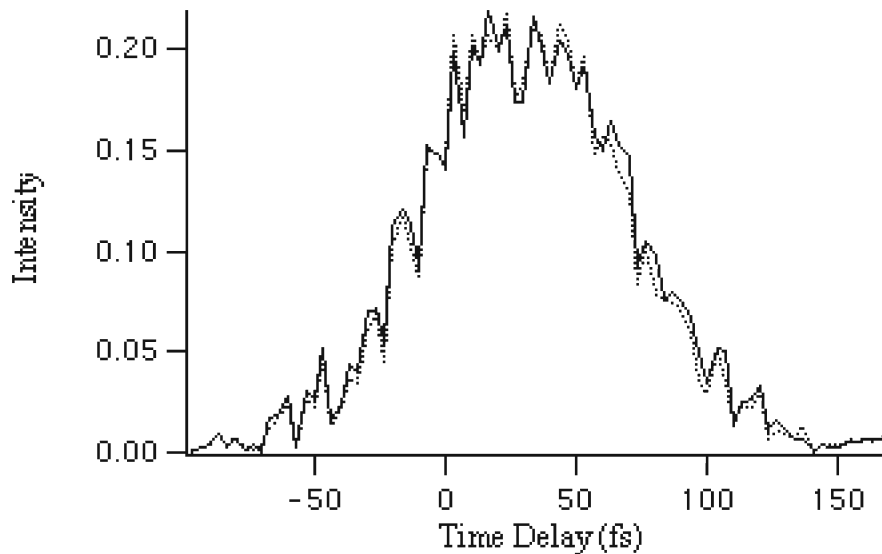


Figure 31: Dephasing Signal for Nile Blue at 310K.

Figure 32 displays the photon echo intensity for Rhodamine 640 drop film at 50K. Scattered intensity as a function of time delay for incident incoherent light of central wavelength 590 nm is shown. For this sample of Rhodamine 640 in PMMA drop film at 50 K, the peak shift of about 37 fs yields a dephasing time just under 20 fs. Similar experiments were made at temperatures of 10, 20, 30, 40, 60, 75, 80, 100, 120.8, 140.2, and 160 K.

Figure 33 shows similar data for the same Rhodamine 640 drop film sample but at 40K. In this graph the scattered light signals along $2\vec{k}_1 - \vec{k}_2$ and $2\vec{k}_2 - \vec{k}_1$ directions are displayed as solid lines. Accurate peak times are extracted from the data using Gaussian fitting functions, shown as dotted and dashed lines. For this sample of Rhodamine 640 in PMMA drop film at 40 K, the peak shift of about 46.5 fs yields a dephasing time of approximately 23 fs.

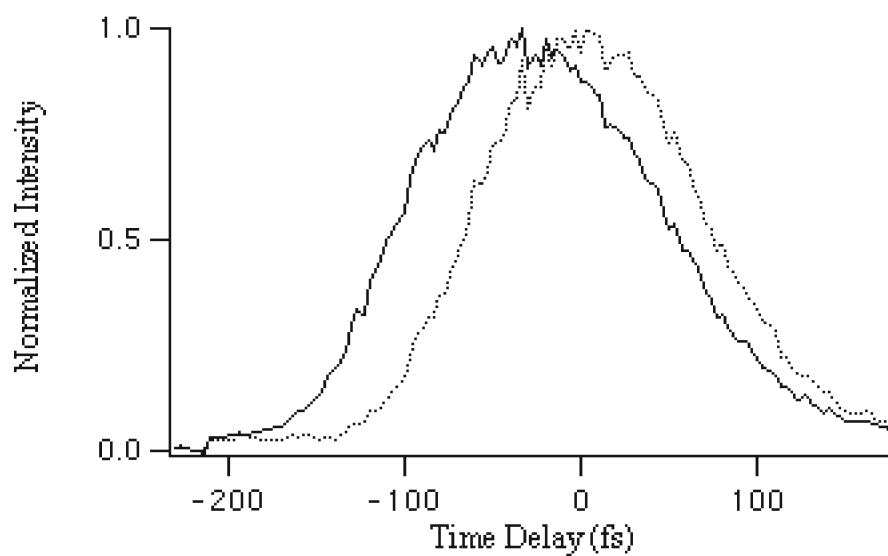


Figure 32: Dephasing Signal at 50K for Rhodamine 640.

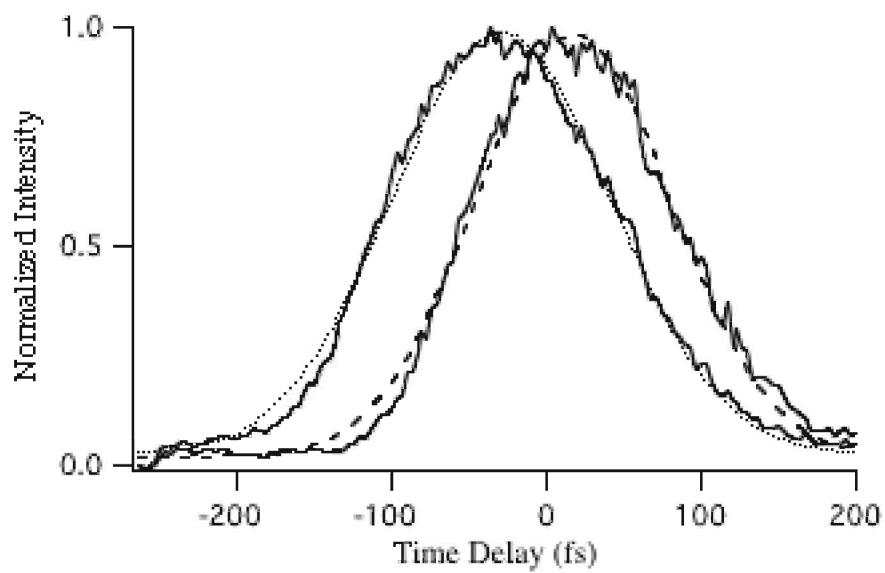


Figure 33: Dephasing Signal at 40K for Rhodamine 640.

8 Discussion

8.1 Single Molecule Emission Histograms

Emission spectra for single fluorescent dye molecules are fit to a Lorentzian lineshape function, from which the reciprocal of the FWHM gives the dephasing or transverse decay time, as calculated by applying the rotating wave approximation to the optical Bloch equations to solve for the quantum expectation value of the molecule's dipole moment.

Of interest for the study of broadening mechanisms and spectral diffusion is the peak wavelength of emission. Histograms for several molecules of each dye are here presented to show the distribution of peak emission and dephasing times for each dye studied. The distributions suggest interesting conclusions for the characterization of each dye. Nile Blue has emission peaks over a wide range of wavelengths, as shown in Figure 34. Dephasing times vary between five and twenty fs, as given in Figure 35. Note that these short dephasing times are too short to measure directly in the photon echo (timing) experiment.

Nile Blue exhibits low photostability, as fluorescence emission lasts generally under one second before photobleaching. The huge distribution in the peak emission wavelengths is likely due to the high reactivity of Nile Blue with its environment, and may be intrinsic to the molecule itself. We could perhaps obtain a better sense of these distributions if lower temperature single molecule emission spectra were taken. Note also that correlation between the dephasing time and degree of dispersion of central emission wavelengths may exist. However, these results give no significant difference between dephasing times for dyes with drastically different peak emission wavelength dispersions.

Rhodamine 640 histograms have a very different profile. This dye exhibits a narrow peak emission wavelength distribution in Figure 36. It also has good photostability and a high fluorescence yield. As for Nile Blue, short dephasing times are observed. However, as shown in Figure 37, these dephasing times average ten fs; this small increase in dephasing time over that of Nile Blue may be significant.

Since inhomogeneous effects are essentially absent from SMF studies, we focus on the effect of local environment randomly shifting the homogeneous resonance line within its inhomogeneous absorption band. These single molecule Lorentzian lines combine to give a smooth Gaussian inho-

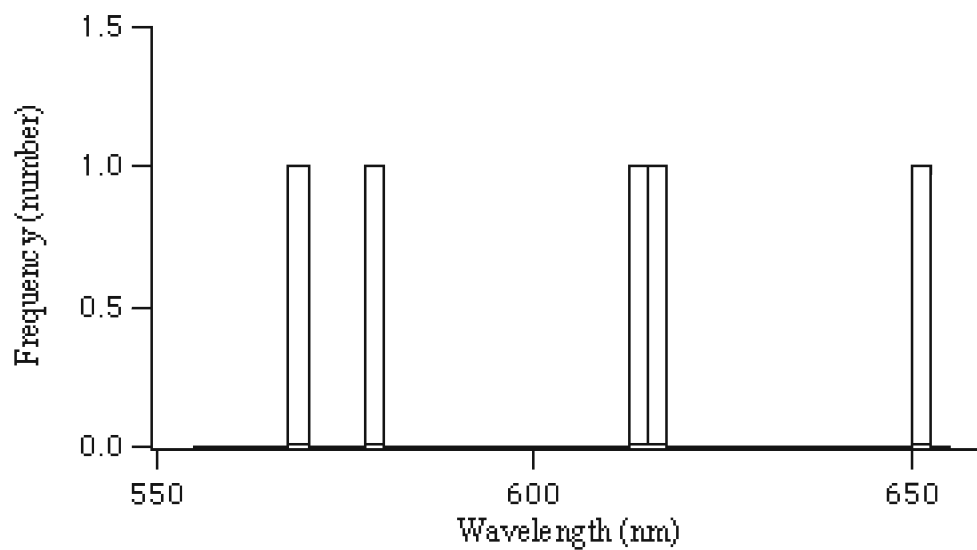


Figure 34: Histogram of Peak Emission Wavelengths for Nile Blue

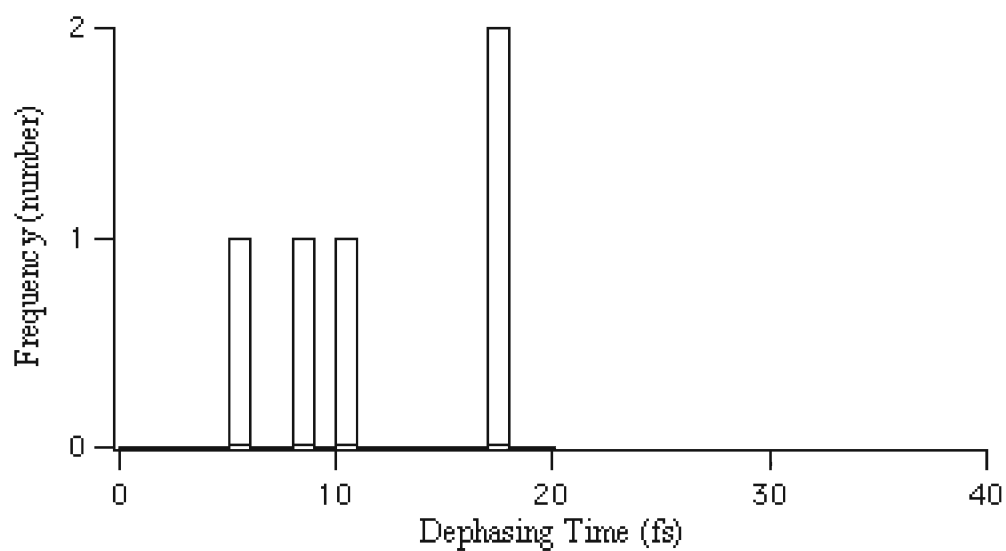


Figure 35: Histogram of Dephasing Times for Nile Blue

mogeneous profile for bulk samples, as seen in our photon echo measurements described in section 8.3.

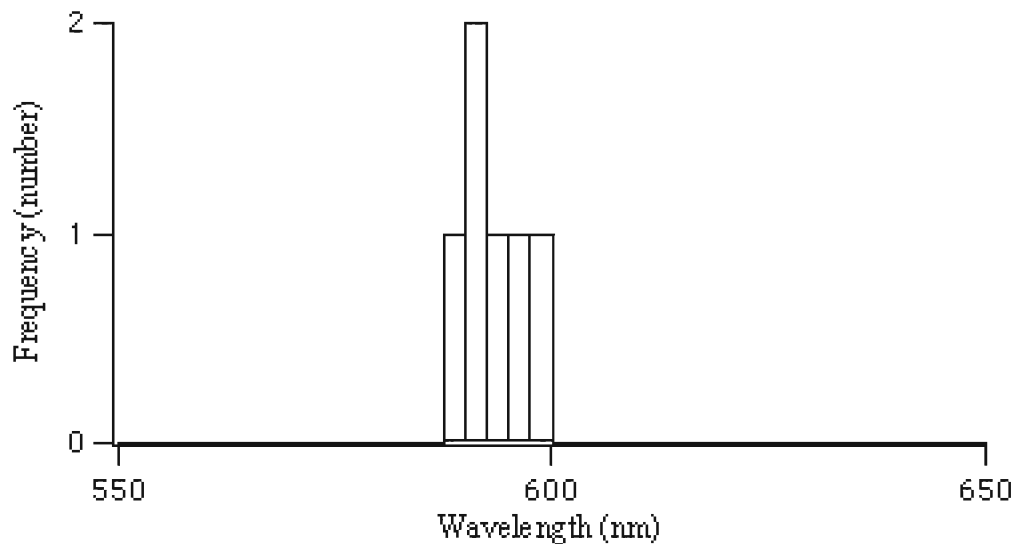


Figure 36: Histogram of Peak Emission Wavelengths for Rhodamine 640

The following figures containing peak emission wavelength and dephasing time histograms for Bodipy, Disperse Red 11, Rhodamine 101, and Styryl 7 are shown in Appendix B: Figures 40, 41, 42, 43, 44, 45, 46, and 47. These data indicate that high photostability may be correlated with tight peak emission wavelength distributions and high fluorescence yield. Further single molecule fluorescence measurements as a function of temperature may be worthy of pursuit for quantification of photostability versus emission bandwidth. Controllable environmental factors include excitation wavelength as well as the intensity profile and magnitude of the excitation light. Also, sample temperature and chemical environment, including environmental gases and the polymer matrix are known to affect fluorescence emission and could therefore be systematically studied more thoroughly.

8.2 Line Broadening Mechanisms

A typical single molecule emission spectra is has a peak emission between 560 and 630 nm, depending on the dye. This spectrum is fit to a Lorentzian using a standard Chi-squared fitting procedure; the IgorPro code written to perform these fits is shown in Appendix B. The fitting parameters give peak frequency and width, the latter of which is used to calculate the dephasing

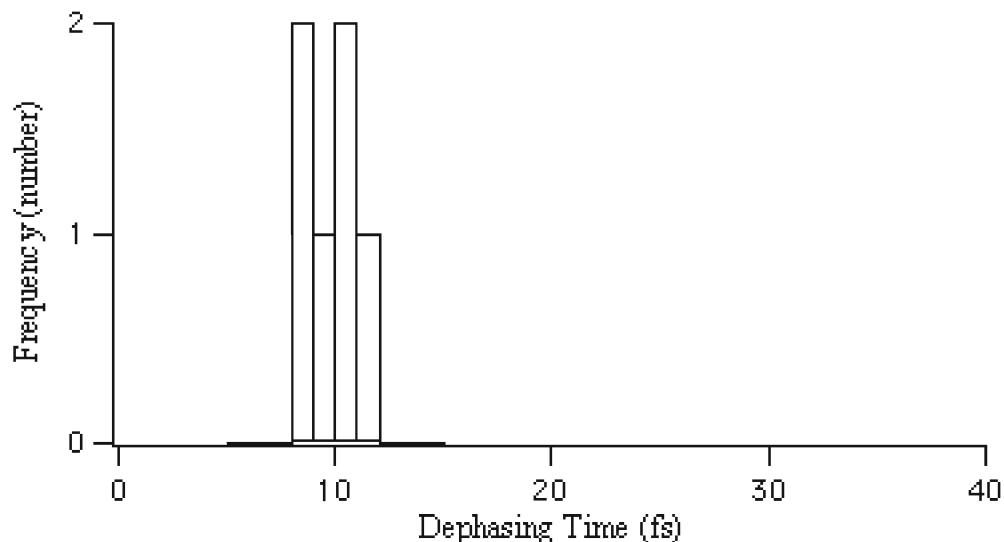


Figure 37: Histogram of Dephasing Times for Rhodamine 640

time [34]. For a single molecule, the dephasing time is the lifetime of the ground and first excited states superposition.

Depending on the integration time scale and local environment of the molecule, various types of spectral broadening may be observed, given that spectral broadening can be a microscopic homogeneous effect caused by various mechanisms. For example, phonon assisted tunneling causes changes in the lattice environment around the molecule. This is a homogeneous effect that explains the temperature-dependent line width and dephasing time [2]. It is also possible that the molecule itself moves, ending up in a different environment. This explains spectral diffusion. Lastly, temperature-induced changes in local molecular environments may occur.

From molecule to molecule, there can exist huge variation in central peak frequency, as shown in the peak wavelength histograms for Nile Blue, Bodipy, and Disperse Red-11 in Figures 34, 40, 42. These distributions are much larger than the homogeneous line width of Rhodamine-640. Evidently, the molecular environment has an important effect on the fluorescence response of a molecule; it is not just the structure of the molecule itself that determines its electronic energy levels, but also the way the molecule interacts with its polymer host. Often these mechanisms for broadening are distinguishable. For example, temperature induced environment changes affect all molecules, giving a fluorescence effect distinctly different from the effects of local environment changes and molecule movement that are likely to affect the fluorescence emission profiles of several but not all molecules

in a region of the sample.

8.3 Photon Echo Temperature Dependence

Detection of photon echo signals at a variety of temperatures permitted examination of dephasing time as a function of temperature. Specifically, the peak shift between scattering directions $2\vec{k}_1 - \vec{k}_2$ and $2\vec{k}_2 - \vec{k}_1$ determined from the detected intensity plots was calculated for Rhodamine 640 in PMMA at temperatures from 20 to 160K. This peak shift is twice the dephasing time [27]. Errors in the Gaussian fits to each intensity plot were propagated to the calculated dephasing time values, yielding the error bars seen in the Figure 38 plot of dephasing time as a function of temperature for Rhodamine 640.

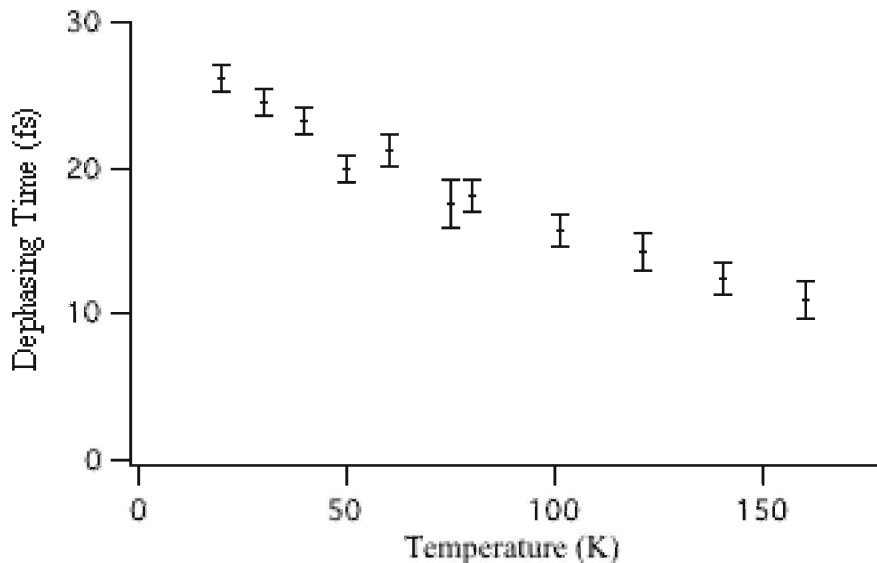


Figure 38: Dephasing time as a function of temperature for Rhodamine 640 in PMMA.

Figure 39 plot of dephasing time as a function of temperature for Nile Blue in PVOH [23]. The primary result of these studies is that the dephasing time extrapolated from the temperature dependence closely agrees with the room temperature dephasing time values derived from the single molecule emission spectra. These are very short dephasing times, indicating a wide distribution of phonon assisted variations in the local environment. This contribution, though termed homogeneous, is not exactly so given the observed distribution. Also, given that the photon echo and single molecule fluorescence experiments occur on vastly different time scales of 10 ns and 10 s re-

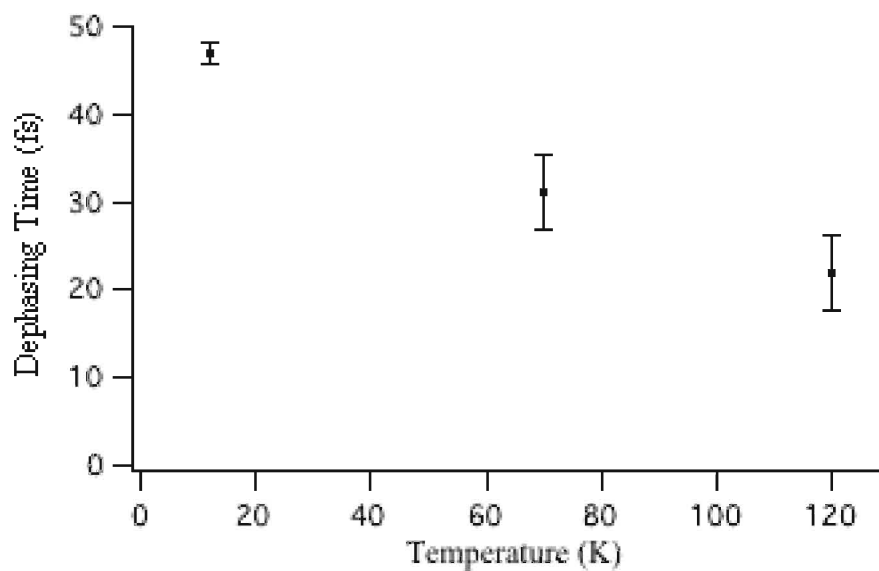


Figure 39: Dephasing time as a function of temperature for Nile Blue in PVOH.

spectively, the agreement on homogeneous linewidth most likely excludes the possibility of spectral diffusion, which is not likely to occur on a 10-ns timescale. Nevertheless, there are a few data sets that provide distinct evidence of spectral diffusion [62].

9 Conclusion

Photon echo and single molecule fluorescence experiments have been performed to study the optical properties of dye-polymer systems. We have confirmed the extraordinarily short optical dephasing times of organic dyes in polymer hosts to be under 20 fs for the oxazine dye Nile Blue and laser dye Rhodamine-640 in polymethylmethacrylate at room temperature. These experimental results were used to determine the natural linewidth of the dye-polymer systems over this temperature range. The short dephasing times suggest homogeneous linewidths on the order of 10 nm at room temperature.

The extremely broadened nature of this line is confirmed by direct observation of single dye molecule fluorescence spectra. Extrapolation of the trend of decreasing dephasing time with increasing temperature yields comparable dephasing times for room temperature measurements in the photon echo and single molecule experiments.

Mechanisms including inhomogeneous broadening and spectral diffusion were examined for comparing results of single molecule and bulk emission spectra and dephasing time measurements. The bulk sample dephasing time, giving the lifetime of the polarizability of the dye in the polymer matrix, is inversely related to the bandwidth of the inhomogeneously broadened absorption since it is known that many of the sample mechanisms are responsible for these effects in the bulk sample.

Since the effect of inhomogeneous broadening is absent from single molecule measurements, narrower linewidths are expected. Therefore, agreement between the linewidths for single molecule and bulk samples indicates presence of another broadening effect in the single molecule environment. Indeed, repeated room-temperature single molecule fluorescence measurements reveal that the homogeneous linewidth is broadened so as to agree with ultrafast dephasing experiments. Spectral diffusion was observed in some cases, as evidenced by the presence of multiple peaks despite broadened lines.

The dephasing time determined by photon echo measurements extrapolated to room temperature agrees with single molecule dephasing times acquired at room temperature within uncertainty of under a factor or two. Specifically, we see that the dephasing time for Rhodamine 640 can be extrapolated to between 10 and 20 fs at room temperature. More conclusive evidence for this extrapolation can be obtained by constructing a good model which suggests a fit for this peak shift vs dephasing time data, or acquiring new data.

New data at higher temperatures using timing photon echo techniques would require interference fringe rather than peak shift analysis, as the dephasing times at higher temperatures are too short for peak shift resolution. A good candidate for these studies is Nile Red with estimated dephasing times under 10 fs. New single molecule fluorescence data at temperatures below room temperature could be acquired, perhaps extending to a regime of temperatures low enough for direct comparison of timing and single molecule measurements.

Our second main conclusion concerns the relation between spectral width and photostability measured at the single molecule level. By comparing our lifetime (time intensity) plots with the width of the histogram of central emission peaks, we can correlate these features. Namely, high photostability and high fluorescence yield correlate with a narrow peak emission wavelength distribution. This is seen most clearly for Rhodamine 640, which exhibits these features, and Nile Blue, which exhibits low photostability, low fluorescence yield, and highly dispersed emission wavelength peaks.

Since our extrapolated low-temperature dephasing times agree with those at room temperature, we can conclude that the dephasing time is a bulk property which extends down to the single molecule level. That is, even at high temperatures, the dephasing time is due to the homogeneous line width of single molecules and therefore is not a bulk property.

Conversely, if we had found spectral diffusion to be a dominant mechanism in play, our single molecule emission spectra would have wider widths which would not agree with the dephasing times measured on the 10-ns time scales with the photon echo experiment. Spectral diffusion would have led to calculated dephasing times that are too short to be in agreement with dephasing times measured in bulk samples. The broad single molecule widths would be largely due to inhomogeneous broadening, the wide distribution of central emission wavelength peaks due to spectral diffusion, the former being caused by the latter and resulting in dephasing times too short to agree with those measured directly for bulk samples.

10 Appendix A: Spectral Analysis Code

This appendix contains IgorPro procedures for single molecule emission and photon echo scattering spectra data analysis.

The following procedure gives the Lorentzian function used to fit single molecule emission spectra as well as the procedure for specifying fit parameters and extracting peak emission wavelengths and calculating dephasing times from the results.

```
function/D lorentzianfit(v,x)
variable/D x
wave/D v
return v[0]+v[1]/(((x-v[2])^2)+(v[3]^2))
end

macro doit()
variable xs,xf
LoadWave/J/D/W/K=0 "Macintosh HD...filepath...filename.asc"
display wave1 vs wave0 //plots intensity signal as a function of wavelength
Label left "\\F'Times'\\Z12Counts"
Label bottom "\\F'Times'\\Z12Wavelength (nm)"
setaxis left -5,15
ModifyGraph nticks(left)=3
setaxis bottom 500,700
duplicate wave0 omegs //converting x-axis from wavelength to frequency units
omegs = 2*3.1416*300/wave0
display wave1 vs omegs
Label left "\\F'Times'\\Z12Intensity (counts)"
Label bottom "\\F'Times'\\Z12Frequency (rad/fs)"
setaxis left -5,15
ModifyGraph nticks(left)=3
setaxis bottom 2.5,4
duplicate/0 wave1 fitwave1 //preparing fit file
fitwave1=0
make/D/0/N=4 W_coef2, W_sigma2
edit W_coef2
appendtotable W_sigma2
make/D/N=4 /0 C2
appendtotable C2
make/D/N=4 /0 sig2
appendtotable sig2
C2={0.85184,10,3.21,.1} //inital guesses for param values {y_0, amp, x_0, width}
FindValue/V=500 /T=.5 wave0 //specifying appropriate frequencies so fit only
xs=V_value //runs from 500 to 700 nm
FindValue/V=700 /T=.5 wave0
xf=V_value
funcfit /H="0000" lorentzianfit, C2, wave1(xs,xf) /X=omegs /D= fitwave1
Duplicate/0/R=(xs,xf) omegs xfit
```

```

Duplicate/O/R=(xs,xf) fitwave1 yfit
appendtograph yfit vs xfit
ModifyGraph rgb(yfit)=(0,0,0)
endmacro

macro fit() //for re-fitting a given spectrum with new parameters
variable xs,xf //once it has been loaded and already fit once with above macro
FindValue/V=500 /T=.5 wave0
xs=V_value
FindValue/V=700 /T=.5 wave0
xf=V_value
funcfit /H="0000" lorentzianfit, C2, wave1(xs,xf) /X=omegs /D= fitwave1
RemoveFromGraph yfit
Duplicate/O/R=(xs,xf) omegs xfit
Duplicate/O/R=(xs,xf) fitwave1 yfit
appendtograph yfit vs xfit
ModifyGraph rgb(yfit)=(0,0,0)
endmacro

macro calc() //calculates peak emission wavelength and dephasing time from fit params
variable peak, T_2
peak=600*pi/(C2[2])
T_2=1/(C2[3])
print peak, T_2
endmacro
//calculate percent errors by hand from errors given by fit routine

```

The following IgorPro procedure was used for fitting the photon echo data to Gaussian functions.

```

function/D mygaussianfit(v,x)
variable/D x
wave/D v
return v[0]+v[1]*exp(-((x-v[2])/v[3])^2)
end

Macro myfit(num)
string num
variable xs,xf

string sname, rname, dname
sname = "sam" + num //specifying sample intensity
duplicate/o sample $sname
$sname = -$sname
rname = "ref" + num //reference intensity
duplicate/o reference $rname
$rname = -$rname
dname = "del" + num //time delay
duplicate/o position $dname
$dname = ($dname-140000)/3 //converting time delay from stepper motor increments to fs
display $sname, $rname vs $dname

```

```

Label left "\\F'Times'\\Z12Normalized Intensity"
Label bottom "\\F'Times'\\Z12Time Delay (fs)"

ModifyGraph rgb($sname)=(0,65535,0)
wavestats $sname
$sname=$sname/V_max //normalizing sample and reference intensities
wavestats $rname
$rname=$rname/V_max
showinfo

string fitsname, fitrname //preparing fits files
fitsname="fitsam"+num
duplicate/o $sname $fitsname
$fitsname=0
make/D/N=4 /O C1,sig1
edit C1, sig1
C1={0,1,10,200} //inital guesses for param values {y_0, amp, x_0, width}

funcfit /H="0000" mygaussianfit, C1,$sname /X=$dname /D= $fitsname
appendtograph $fitsname vs $dname
ModifyGraph rgb($fitsname)=(0,65535,0),lstyle($fitsname)=1

fitrname="fitref"+num
duplicate/o $rname $fitrname
$fitrname=0
make/D/N=4 /O C1,sig1
edit C1, sig1
C1={0,1,-10,200} //inital guesses for param values {y_0, amp, x_0, width}

funcfit /H="0000" mygaussianfit, C1,$rname /X=$dname /D= $fitrname
appendtograph $fitrname vs $dname
ModifyGraph lstyle($fitrname)=1

endmacro

```

11 Appendix B: Single Molecule Emission Histograms

The following figures containing peak emission wavelength and dephasing time histograms for Bodipy, Disperse Red 11, Rhodamine 101, and Styryl 7 are shown in this appendix: Figure 40, Figure 41, Figure 42, Figure 43, Figure 44, Figure 45, Figure 46, and Figure 47.

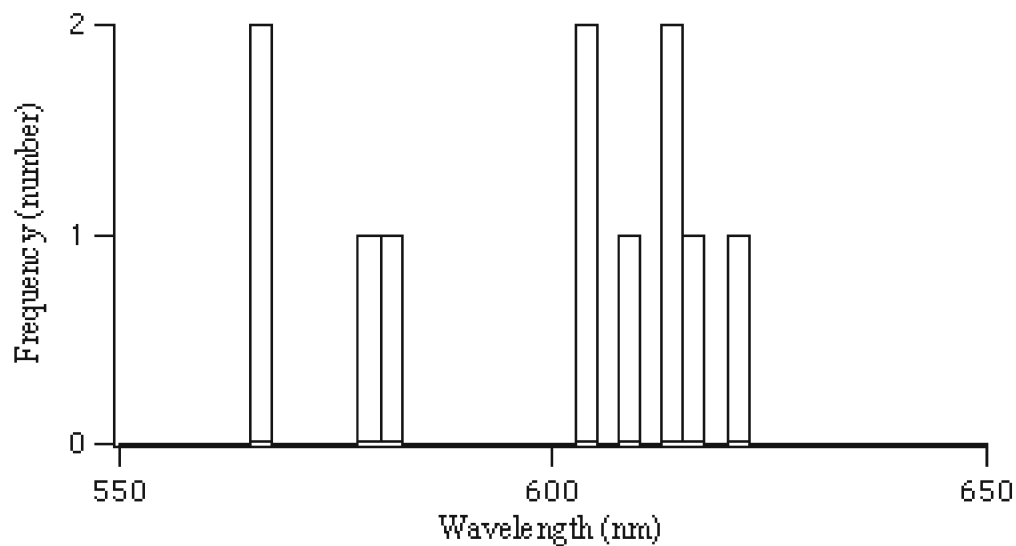


Figure 40: Histogram of Peak Emission Wavelengths for Bodipy

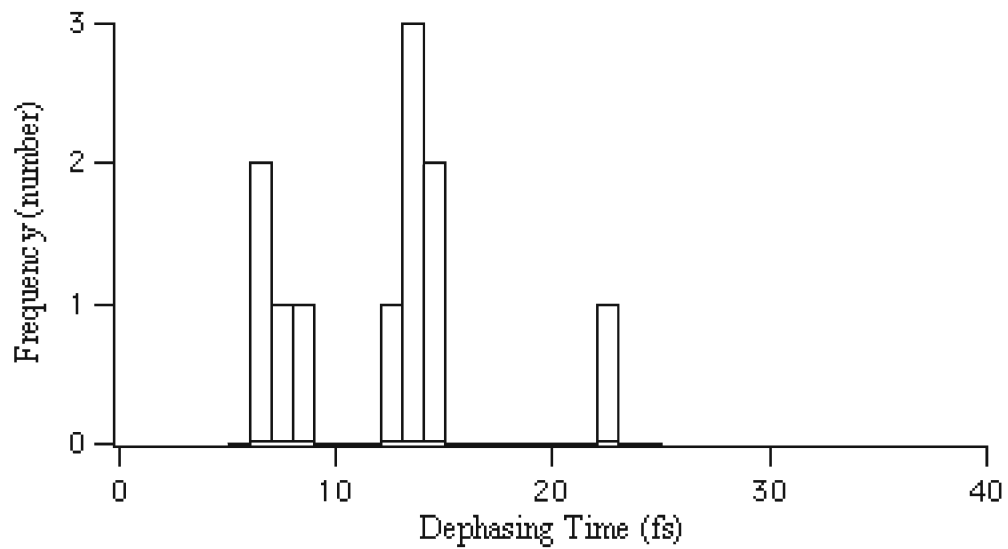


Figure 41: Histogram of Dephasing Times for Bodipy

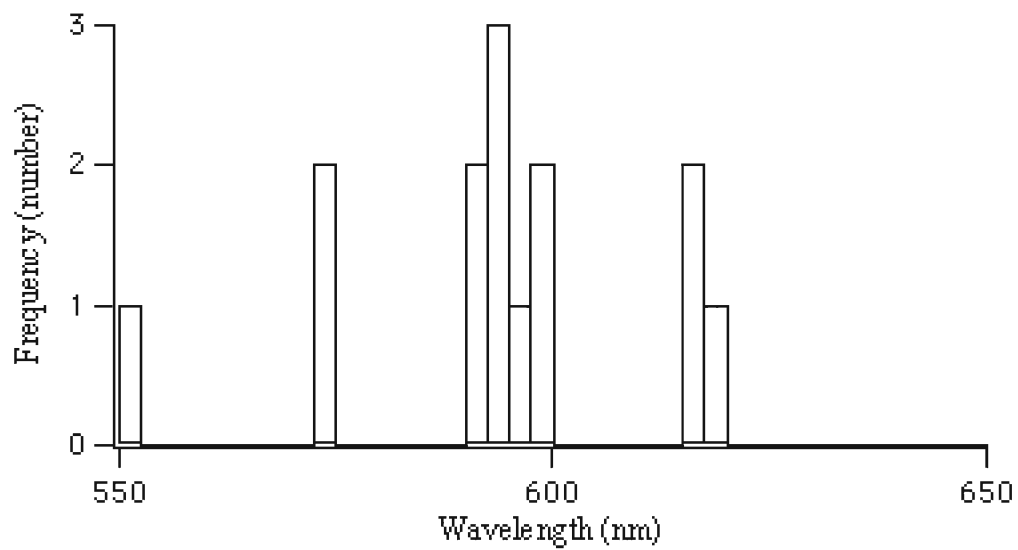


Figure 42: Histogram of Peak Emission Wavelengths for Disperse Red 11

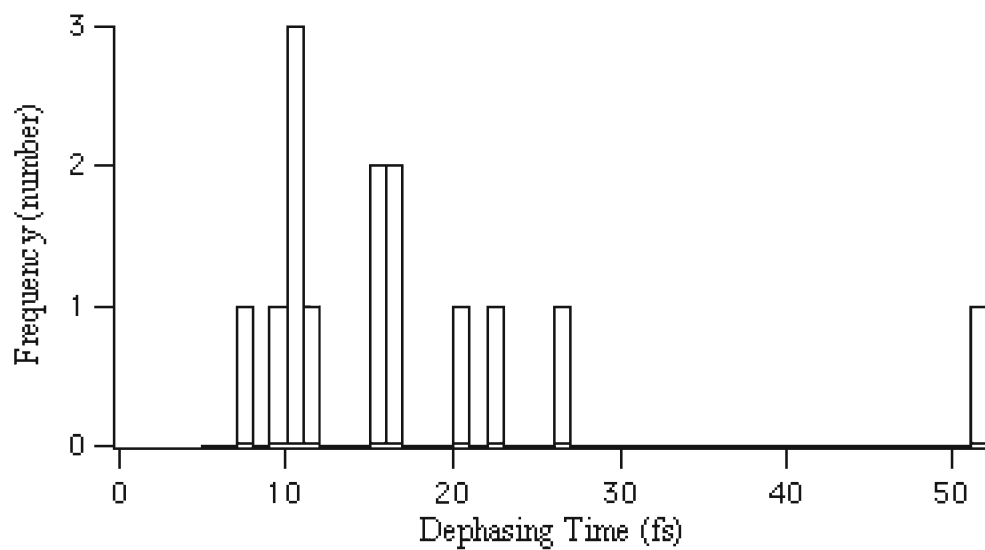


Figure 43: Histogram of Dephasing Times for Disperse Red 11

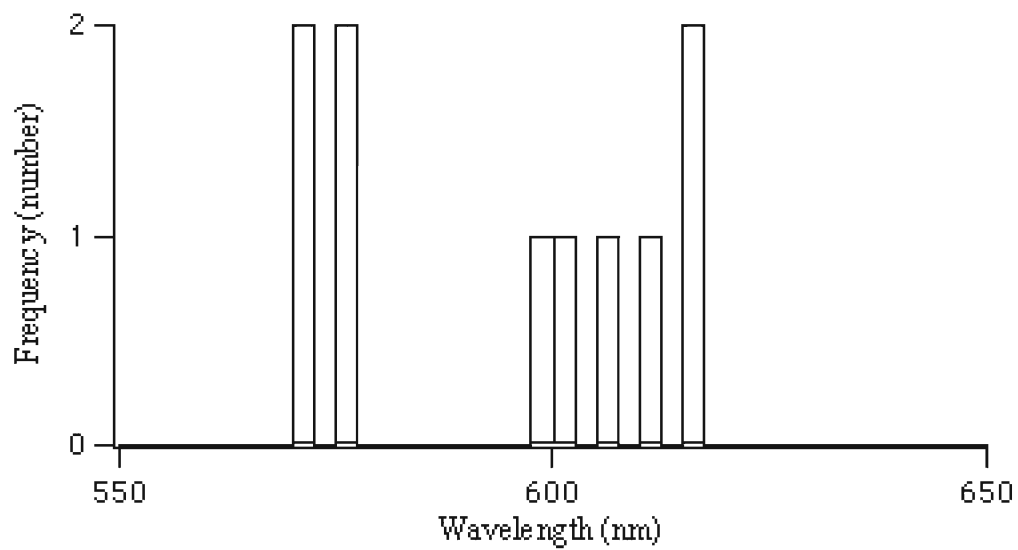


Figure 44: Histogram of Peak Emission Wavelengths for Rhodamine 101

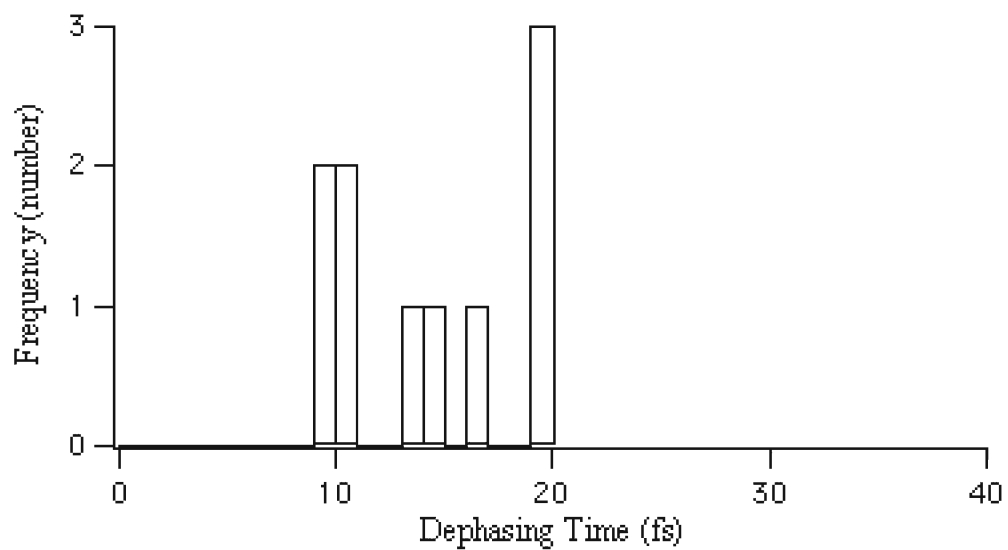


Figure 45: Histogram of Dephasing Times for Rhodamine 101

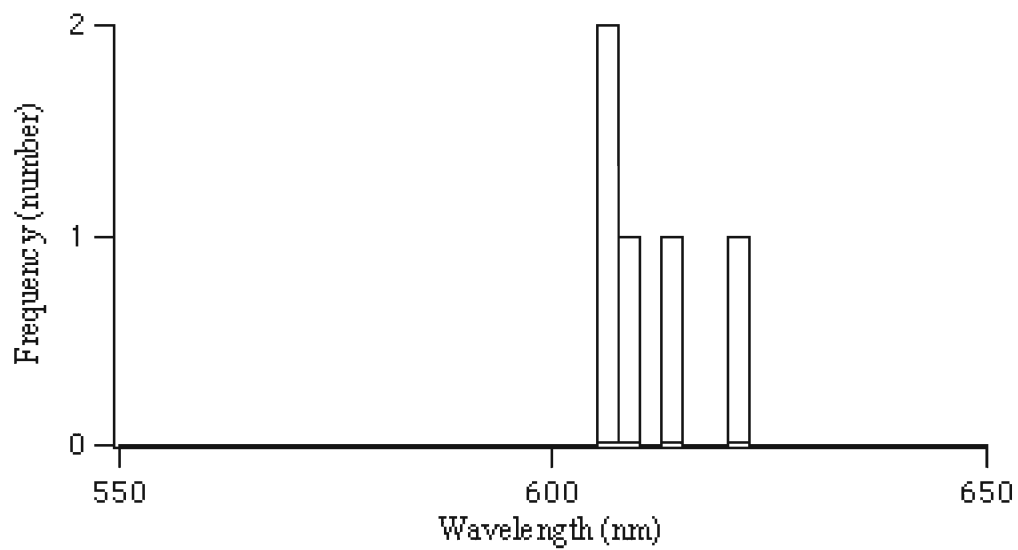


Figure 46: Histogram of Peak Emission Wavelengths for Styryl 7

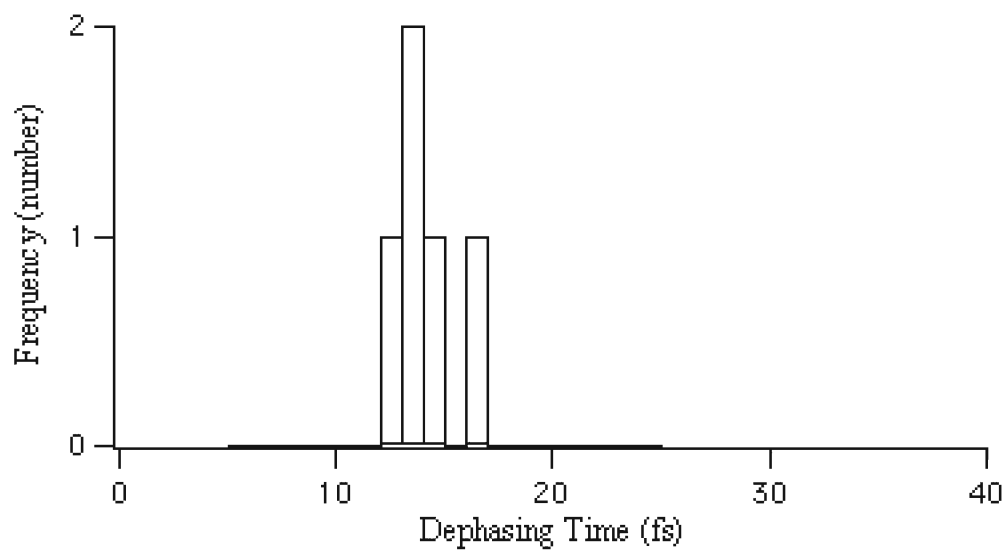


Figure 47: Histogram of Dephasing Times for Styryl 7

List of Figures

1	Three-Level System	11
2	Absorption of Disperse Red 1	33
3	More Absorption for Disperse Red 1	34
4	Spectra for Bodipy	35
5	Spectra for Rhodamine 640	35
6	Spectra for Nile Red	36
7	Disperse Red 1 Fluorescence	37
8	More Disperse Red 1 Fluorescence	37
9	Fluorescence Experimental Setup	41
10	Cyanine Correlation Function	44
11	DR-11 Correlation Function	44
12	R-101 Correlation Function	45
13	Another R-101 Correlation Function	45
14	An Excellent R-101 Correlation Function	46
15	Styryl-7 Multiple-Molecule Correlation Function	47
16	Styryl-7 Correlation Function	47
17	Cyanine Time Intensity Plot	49
18	DR-11 Time Intensity Plot	49
19	R-101 Time Intensity Plot	50
20	Another R-101 Time Intensity Plot	51
21	A Final R-101 Time Intensity Plot	51
22	Styryl-7 Time Intensity Plot	52
23	R-640 Time Intensity Plot	52
24	Another R-640 Time Intensity Plot	53
25	Single Molecule Emission Spectrum for Cyanine	54
26	A Second Single Molecule Emission Spectrum for Cyanine	55
27	Single Molecule Emission Spectrum for Nile Red	56
28	Photon Echo Experimental Setup	61
29	Beam Geometry for DFWM	62
30	Dephasing Signal for NB in PVOH at 12K	64
31	Dephasing Signal for Nile Blue at 310K	65
32	Rhodamine 640 Dephasing Signal at 50K	66
33	Rhodamine 640 Dephasing Signal at 40K	66
34	Histogram of Peak Emission Wavelengths for Nile Blue	68

35	Histogram of Dephasing Times for Nile Blue	68
36	Histogram of Peak Emission Wavelengths for Rhodamine 640	69
37	Histogram of Dephasing Times for Rhodamine 640	70
38	Dephasing Time vs. Temperature for Rhodamine 640	71
39	Dephasing Time vs. Temperature for Nile Blue	72
40	Histogram of Peak Emission Wavelengths for Bodipy	78
41	Histogram of Dephasing Times for Bodipy	79
42	Histogram of Peak Emission Wavelengths for Disperse Red 11	80
43	Histogram of Dephasing Times for Disperse Red 11	80
44	Histogram of Peak Emission Wavelengths for Rhodamine 101	81
45	Histogram of Dephasing Times for Rhodamine 101	81
46	Histogram of Peak Emission Wavelengths for Styryl 7	82
47	Histogram of Dephasing Times for Styryl 7	82

References

- [1] L. Allen and J.H. Eberly. *Optical Resonance and Two-Level Atoms*. Dover Publications, New York, first edition, 1987.
- [2] P.W. Anderson, B.I. Halperin, and C.M. Varma. Anomalous Low-temperature Thermal Properties of Glasses and Spin Glasses. *The Philosophical Magazine*, 25:1, 1971.
- [3] Th. Basché, W.E. Moerner, M. Orrit, and H. Talon. Photon Antibunching in the Fluorescence of a Single Dye Molecule Trapped in a Solid. *Physical Review Letters*, 69:1516, 1992.
- [4] Isadore B. Berlman. *Handbook of Fluorescence Spectra of Aromatic Molecules*. Academic Press, New York, first edition, 1965.
- [5] David A. Vanden Bout, Wai-Tak Yip, Dehong Hu, Dian-Kui Fu, Timothy M. Swager, and Paul F. Barbara. Discrete Intensity Jumps and Intramolecular Electronic Energy Transfer in the Spectroscopy of Single Conjugated Polymer Molecules. *Science*, 277:1074–1077, 1997.
- [6] Rosa Brouri, Alexios Beveratos, Jean-Philippe Poizat, and Philippe Grangier. Photon antibunching in the fluorescence of individual color centers in diamond. *Optics Letters*, 15:1294, 2000.
- [7] X. Cheng and T. Kobayashi. 3-Beam Degenerate 4-Wave Mixing Using Incoherent Light. *Mol. Cryst. Liq. Cryst*, 182A:139, 1990.
- [8] Laurent Cognet, Françoise Coussen, Daniel Choquet, and Brahim Lounis. Fluorescence microscopy of single autofluorescent proteins for cellular biology. *Single Molecule Biophysics*, 3:645, 2002.
- [9] Alan Corney. *Atomic and Laser Spectroscopy*. Oxford Science Publications, New York, first edition, 1988.
- [10] C.H. Brito Cruz, R.L. Fork, W.H. Know, and C.V. Shank. Spectral Hole Burning in Large Molecules Probed with 10-fs Optical Pulses. *Chemical Physics Letters*, 132:341, 1986.
- [11] Wolfgang Demtröder. *Laser Spectroscopy: Basic Concepts and Instrumentation*. Springer, New York, second edition, 1998.
- [12] Robert M. Dickson, Andrew B. Cubitt, Roger Y. Tsien, and W.E. Moerner. On/off blinking and switching behavior of single molecules of green fluorescent protein. *Nature*, 1997.

- [13] T.D. Donnelly and Carl Grossman. Ultrafast phenomena: A laboratory experiment for undergraduates. *American Journal of Physics*, 66:677, 1998.
- [14] Koos Duppen, Foppe de Haan, Erik T.J. Nibbering, and Douwe A. Wiersma. Chirped four-wave mixing. *Physical Review A*, 47:5120, 1993.
- [15] B.L. Fearey, T.P. Carter, and G.J. Small. Efficient Nonphotochemical Hold Burning of Dye Molecules in Polymers. *Journal of Physical Chemistry*, 87:3590–3592, 1983.
- [16] Richard P. Feynman, Frank L. Vernon, and Robert W. Hellwarth. Geometrical Representation of the Schrödinger Equation for Solving Maser Problems. *Journal of Applied Physics*, 28:49, 1957.
- [17] Henk Fidder, Jacob Terpstra, and Douwe A. Wiersma. Dynamics of Frenkel excitons in disordered molecular aggregates. *Journal of Chemical Physics*, 94:6895, 1991.
- [18] Masahiro Fujiwara, Ryo Kuroda, and Hiroki Nakatsuka. Measurement of ultrafast dephasing time of Cresyl Fast Violet in cellulose by photon echoes with incoherent light. *J. Opt. Soc. Am. B*, 2:1634–1639, 1985.
- [19] J.E. Golub and T.W. Mossberg. Ultrahigh-frequency interference beats in transient, incoherent-light four-wave mixing. *Optics Letters*, 11:431, 1986.
- [20] David J. Griffiths. *Introduction to Electrodynamics*. Prentice Hall, Upper Saddle River, NJ, third edition, 1999.
- [21] Carl Grossman. Personal Communication.
- [22] Carl Grossman. Unpublished laboratory notebook 8.
- [23] Carl H. Grossman and Julie J. Schwendiman. Ultrashort dephasing-time measurements in Nile Blue polymer films. *Optics Letters*, 23:624–626, 1998.
- [24] N.V. Gruzdev and Yu.G. Vainer. Nanosecond spectral diffusion and optical dephasing in organic glasses over a wide temperature range: incoherent photon echo study of reosufirin in D- and D₆-ethanol. *Journal of Luminescence*, 56:181, 1993.
- [25] Anne Myers Kelley, Xavier Michalet, and Shimon Weiss. Single-Molecule Spectroscopy Comes of Age. *Science*, 292:1671, 2001.
- [26] H.J. Kimble, M. Dagenais, and L. Mandel. Photon Antibunching in Resonance Fluorescence. *Physical Review Letters*, 39:691, 1977.

- [27] T. Kobayashi, A. Terasaki, T. Hattori, and K. Kurokawa. The Application of Incoherent Light for the Study of Femtosecond-Picosecond Relaxation in Condensed Phase. *Applied Physics B*, 47:107–125, 1988.
- [28] Takayoshi Kobayashi, Toshiaki Hattori, Akira Terasaki, and Kenji Kurokawa. Sub-picosecond vibrational dephasing measured by coherent Raman scattering and libration relaxation by degenerate four-wave mixing, using temporally incoherent light. *Time Resolved Spectroscopy*, page 113, 1989.
- [29] M.A. Kol’chenko, Yu.G. Vainer, and R.I. Personov. Optical dephasing in polymers and the soft potential model: analysis of photon echo in doped PMMA. *Journal of Luminescence*, 2002.
- [30] Valery Kozich, Leonardo de S. Menezes, and Cid B. de Araújo. Interference effects in time-delayed degenerate four-wave mixing with broadband noisy light. *Journal of the Optical Society of America B*, 17:973, 2000.
- [31] A. Kummrow. Optical dephasing of neat liquids and liquid crystals studied by forced light scattering. *Chemical Physics Letters*, 236:362, 1995.
- [32] A. Kummrow and A. Lau. Dynamics in condensed molecular systems studied by incoherent light. *Applied Physics B*, 63:209, 1996.
- [33] L.D. Landau and E.M. Lifshitz. *The Classical Theory of Fields: Course of Theoretical Physics Volume 2*. Pergamon, New York, fourth edition, 1975.
- [34] Rodney Loudon. *The Quantum Theory of Light*. Oxford University Press, Oxford, third edition, 2000.
- [35] B. Lounis and W.E. Moerner. Single photons on demand from a single molecule at room temperature. *Nature*, 2000.
- [36] J.J. Macklin, J.K. Trautman, T.D. Harris, and L.E. Brus. Imaging and Time-Resolved Spectroscopy of Single Molecules at an Interface. *Science*, 272:255, 1996.
- [37] Amit D. Mehta, Mattias Rief, James A. Spiduch, David A. Smith, and Robert M. Simmons. Single-Molecule Biomechanics with Optical Methods. *Science*, 183:1689, 1999.
- [38] Hans C. Meijers and Douwe A. Wiersma. Glass Dynamics Probed by the Long-Lived Stimulated Photon Echo. *Physical Review Letters*, 68:381, 1992.

- [39] Xavier Michalet and Shimon Weiss. Single-molecule spectroscopy and microscopy. *Single Molecule Biophysics*, 3:619–644, 2002.
- [40] Peter W. Milonni and Joseph H. Eberly. *Lasers*. John Wiley, New York, first edition, 1988.
- [41] K. Misawa and T. Kobayashi. Ultrafast Dephasing Measurement by Transient Four-Wave Mixing. *Mol. Cryst. Liq. Cryst*, 182A:125, 1990.
- [42] W.E. Moerner. Examining Nanoenvironments in Solids on the Scale of a Single, Isolated Impurity Molecule. *Science*, 266:46, 1994.
- [43] W.E. Moerner. Polymer Luminescence: Those Blinking Single Molecules. *Science*, 277:5329, 1999.
- [44] W.E. Moerner. A Dozen Years of Single-Molecule Spectroscopy in Physics, Chemistry, and Biophysics. *Journal of Physical Chemistry B*, 106:910–927, 2002.
- [45] W.E. Moerner and L. Kador. Optical Detection and Spectroscopy of Single Molecules in a Solid. *Physical Review Letters*, 62:2535, 1989.
- [46] W.E. Moerner and Michel Orrit. Illuminating Single Molecules in Condensed Matter. *Science*, 8283:1670, 1999.
- [47] Andrzej Molski, Johan Hofkens, Thomas Gensch, Noël Boens, and Frans De Schryver. Theory of time-resolved single-molecule fluorescence spectroscopy. *Chemical Physics Letters*, 318:325–332, 2000.
- [48] Norio Morita and Tatsuo Yajima. Ultrahigh-time-resolution coherent transient spectroscopy with incoherent light. *Physical Review A*, 30:2525–2535, 1984.
- [49] F. Moshary, M. Arend, R. Friedberg, and S.R. Hartmann. Ultrafast relaxation and modulation in the oxazine dye nile blue. *Physical Review A*, 46:R33, 1992.
- [50] Shaul Mukamel. Solvation Effects in Four-wave Mixing and Spontaneous Raman and Fluorescence Lineshapes of Polyatomic Molecules. *Adv. Chem. Phys.*, 70:165, 1988.
- [51] Shaul Mukamel. Femtosecond Optical Spectroscopy: A Direct Look at Elementary Chemical Events. *Annual Reviews of Physical Chemistry*, 41:647–681, 1990.
- [52] K.-P. Müller and D. Haarer. Spectral Diffusion of Optical Transitions in Doped Polymer Glasses below 1 K. *Physical Review Letters*, 66:2344, 1991.

- [53] S. Nakanishi, H. Ohta, N. Makimoto, and H. Itoh. Temperature-dependent femtosecond dephasing of vibronic lines in a Nile-blue-doped polymer system. *Physical Review B*, 45:2825, 1992.
- [54] S. Nakanishi, H. Ohta, N. Makimoto, and H. Itoh. Temperature-dependent femtosecond dephasing of vibronic lines in a Nile-blue-doped polymer system. *Physical Review B*, 45:2825, 1992.
- [55] L.R. Narashimhan, Dee Williams Pack, and M.D. Fayer. Solute-solvent dynamics and interactions in glassy media: photon echo and optical hole burning studies of cresyl violet in ethanol glass. *Chemical Physics Letters*, 152:287, 1988.
- [56] L.R. Narasimhan, K.A. Littau, Dee William Pack, Y.S. Bai, A. Elschner, and M.D. Fayer. Probing Organic Glasses at Low Temperature with Variable Time Scale Optical Dephasing Measurements. *Chemical Review*, 90:439, 1990.
- [57] A.V. Naumov and Yu.G. Vainer. Minimal distance between chromophore and two-level systems in amorphous solids: effect on photon echo and single molecule spectroscopy data. *Journal of Luminescence*, 209, 2002.
- [58] Erik T.J. Nibbering, Koos Duppen, and Douwe A. Wiersma. Solution dynamics by line shape analysis, resonance light scattering, and femtosecond four-wave mixing. *Journal of Photochemistry and Photobiology A: Chemistry*, 62:347, 1992.
- [59] Erik T.J. Nibbering, Douwe A. Wiersma, and Koos Duppen. Ultrafast electronic fluctuation and solvation in liquids. *Chemical Physics*, 183:167, 1994.
- [60] Shuming Nie, Daniel T. Chiu, and Richard N. Zare. Probing Individual Molecules with Confocal Fluorescence Microscopy. *Science*, 266:1018, 1994.
- [61] M. Orrit and J. Bernard. Single Pentacene Molecules Detected by Fluorescence Excitation in a *p*-Terphenyl Crystal. *Physical Review Letters*, 65:2716, 1990.
- [62] M. Orrit, J. Bernard, and R.I. Personov. High-resolution spectroscopy of organic molecules in solids: From fluorescence line narrowing and hole burning to single molecule spectroscopy. *J. Phys. Chem.*, 97:10256–10268, 1993.
- [63] Taras Plakhotnik, Daniel Walser, Marco Pirotta, Alois Renn, and Urs P. Wild. Nonlinear Spectroscopy on a Single Quantum System: Two-Photon Absorption of a Single Molecule. *Science*, 271:1703–, 1996.

- [64] R. Purchase, A. Gorshchev, B.M. Kharlamov, T. Plakhotnik, and U.P. Wild. Optical dephasing in terrylene-doped polymer microspheres. *Journal of Luminescence*, 94:211, 2001.
- [65] B.E.A. Saleh and M.C. Teich. *Fundamentals of Photonics*. John Wiley, New York, first edition, 1991.
- [66] Robin Smith. Unpublished laboratory notebook 2, Swarthmore College, Summers 2001-2.
- [67] Robin Smith. Unpublished laboratory notebook 3, Swarthmore College, 2002-3.
- [68] Robin Smith. Unpublished laboratory notebook 1, Swarthmore College, Summer 2001.
- [69] Charles W. Teplin. Hole Burning and Optical Dephasing of the Dye Nile Blue in a Polymer Matrix. Unpublished research summary, Swarthmore College.
- [70] François Treussart, Romain Alléaume, Véronique Le Floch, and Jean-François Roch. Single photon emission from a single molecule. *Molecular Photonics: Materials, Physics, and Devices*, 3:501–508, 2002.
- [71] François Treussart, Romain Alléaume, Véronique Le Floch, L.T. Xiao, J.-M. Courty, and Jean-François Roch. Direct Measurement of the Photon Statistics of a Triggered Single Photon Source. *Physical Review Letters*, 89, 2002.
- [72] François Treussart, André Clouqueur, Carl Grossman, and Jean-François Roch. Photon antibunching in the fluorescence of a single dye molecule embedded in a thin polymer film. *Optics Letters*, 26:1504–1506, 2001.
- [73] Yu.G. Vainer, T.V. Plakhotnik, and R.I. Personov. Dephasing and diffusional linewidths in spectra of doped amorphous solids: comparison of photon echo and single molecule spectroscopy data for terrylene in polyethylene. *Chemical Physics*, 209:101–110, 1996.
- [74] A.M. Weiner, S. De Silvestri, and E.P. Ippen. Three-pulse scattering for femtosecond dephasing studies: theory and experiment. *Journal of the Optical Society of America B*, 2:654–661, 1985.
- [75] Shimon Weiss. Fluorescence Spectroscopy of Single Biomolecules. *Science*, 283:1676, 1999.
- [76] X. Sunny Xie and Robert C. Dunn. Probing Single Molecule Dynamics. *Science*, 265:361, 1994.
- [77] T. Yajima. Non-linear Optical Spectroscopy of an Inhomogeneously Broadened Resonant Transition by Means of Three-Wave Mixing. *Optics Communications*, 14:378–382, 1975.

- [78] Yiping Zhang, S.R. Hartmann, and Fred Moshary. Fluorescence-line-narrowing spectroscopy of Nile blue in glass and polymer at 5K: Determination of a single-site line shape function. *Journal of Chemical Physics*, 104:4371, 1996.
- [79] Yiping Zhang, S.R. Hartmann, and Fred Moshary. Incoherent four-wave-mixing on Nile blue and cresyl violet in glass and polymer at 5L: Single-site line shape analysis. *Journal of Chemical Physics*, 104:4380, 1996.
- [80] Yiping Zhang, Fred Moshary, and S.R. Hartmann. Incoherent Broad-Band Time-Delayed Four-Wave-Mixing Spectroscopy of Nile Blue in Polyvinyl Alcohol. *Laser Physics*, 5:676–681, 1995.
- [81] Andreas Zumbusch, Ludovic Fleury, Ross Brown, Jacky Berhard, and Michel Orrit. Probing Individual Two-Level Systems in a Polymer by Correlation of Single Molecule Fluorescence. *Physical Review Letters*, 70:3584, 1993.

Acknowledgments

Carl Grossman has served as an excellent mentor and advisor. François Treussart and Jean-François Roch were energetic collaborators who graciously gave their time and resources to help us perform single molecule fluorescence measurements. Romain Alléaume helped with single molecule apparatus calibration answered many of my questions, while L.T. Xiao helped with data acquisition. Peter Collings permitted our use of his spin-coating apparatus and spectrophotometer. Robert Pasternack permitted our use of his fluorimeter. Daniel Sproul performed initial work on fabricating spin-coated films of Nile Blue in PVOH and water, and Elliot Reed acquired much of the dephasing data. Benjamin Bau and Steve Palmer built boxes to keep out dust and keep in light for the dephasing experiment. Funding from the American Chemical Society, Swarthmore College, and Howard Hughes Medical Institute is greatly appreciated.